2011

A CFD Model of Mixing in a Microfludic Device for Space Medicine Technology

Terri Lynn McKay
Cleveland State University

A CFD MODEL OF MIXING IN A MICROFLUIDIC DEVICE FOR SPACE MEDICINE TECHNOLOGY

TERRI LYNN MCKAY

Bachelor of Science in Chemistry

May, 2003

submitted in partial fulfillment of requirements for the degree

MASTER OF SCIENCE IN MECHANICAL ENGINEERING

at the

CLEVELAND STATE UNIVERSITY

May, 2011

APPROVAL PAGE

This thesis has been approved for the Department of MECHANICAL ENGINEERING and the College of Graduate Studies by:

Dr. Mounir Ibrahim/Thesis Committee Chairperson

_____

Department/Date

Dr. Petru Fodor

_____

Department/Date

Dr. Miron Kaufman

_____

Department/Date

Dr. Emily Nelson

_____

Department/Date

ACKNOWLEDGEMENT

There are many people that I would like to thank for their encouragement and support throughout the course of this endeavor. I would first like to thank my advisor, Dr. Mounir Ibrahim, for helping to guide me as I transitioned from an undergraduate education in chemistry to graduate studies in mechanical engineering and for providing his expertise in fluid flow and computational analysis.

I would also like to thank Dr. Emily Nelson for her service as a committee member and for her support throughout this project. Her knowledge of fluid flow and research into the novel area of medical devices tailored for space applications was truly enabling to this effort. The mutual appreciation of snowflakes and flowers was an extreme bonus!

I am also grateful to Dr. Petru Fodor and Dr. Miron Kaufman for their services as committee members and for providing their expertise in microfluidic mixing.

I am extremely thankful for the three supervisors I have worked with during the course of this effort: Dr. John Sankovic, Ms. June Zakrajsek, and Dr. Jerry Myers. I would especially like to thank Dr. Sankovic for all of the excellent advice for being such an outstanding role model and mentor.

Thanks also to NASA's Human Research Program at JSC and GRC for their support of this work. In particular, I am grateful to the project managers at GRC for their appreciation, encouragement and understanding throughout the past two years.

I am truly grateful to everyone on the Reusables/rHEALTH project at NASA and DMI. It is a pleasure to work with such a great team. Thanks to Eugene Chan, M.D. for his first-class work developing the rHEALTH technology. I am especially thankful to Dan Brown for his efforts and for always taking the time to explain the details of how everything works.

I would like to thank all of my family, friends, and coworkers for their encouragement and understanding as I have focused on this work and neglected far too many social opportunities. I truly look forward to having more time to spend with everyone soon!

I wish to especially thank my wonderful husband, Billy, for his patience and understanding over the past couple years. I am also grateful to my parents and my parent-in-laws. I'm fairly certain I could not have done this without spaghetti/family night to nourish my body and soul. I am also thankful to my stister Tressie and her wonderful family.

A CFD MODEL OF MIXING IN A MICROFLUIDIC DEVICE FOR SPACE MEDICINE TECHNOLOGY

TERRI LYNN MCKAY

ABSTRACT

The DNA Medicine Institute (DMI) is currently developing a device to be used for blood analysis to satisfy the unique requirements of space medicine applications. A key component of that device is the micromixer, which will ensure mixing and dilution of reagents utilized for detection assays. As part of the device design process, the micromixer was modeled, and the mixing characteristics were analyzed and compared to experimental data. The experimental data was based on a top-view of the system and, lacking data throughout the fluid domain, could not provide the insight into the mixing process that modeling could readily provide. COMSOL, a Finite Element Method (FEM) package, was used to model the mixer. The mixer design is essentially a spiral channel and relies on centrifugal effects, or Dean flow forces that arise from flows in curved channels, to enhance mixing. A computational model of DMI's spiral mixer was analyzed and compared to experimental data for flow ranging in Reynolds number between 8 and 90. The Dean number range was between 0 and 25. The fluids modeled were miscible and Newtonian. It was observed that at Reynolds number less than 12 (De < 2), the mixing occurred primarily by diffusion and at Reynolds numbers above 30 (De > 11), convective forces dominated. In an intermediate range, Reynolds numbers between 12 and 30 (De 2 – 11), mixing appeared to be enhanced as both diffusion and convection aided the mixing. Due to the rotational nature of the flow, this was not readily apparent from the experimental data. The model is a good tool to optimize design choices since the numerical data can be used to quantify mixing characteristics throughout the entire mixer volume, thereby providing a better insight into mixing performance.

TABLE OF CONTENTS

LIST OF TABLES

LIST OF FIGURES

NOMENCLATURE

Acronyms:

CAD	Computer Aided Design
CDRH	Center for Devices and Radiological Health
CFD	Computational Fluid Dynamics
COTS	Commercial Off-The-Shelf
DMI	DNA Medicine Institute
FDA	Food and Drug Administration
FEM	Finite Element Method
GRC	Glenn Research Center
IVD	*In Vitro* Diagnostic
ISS	International Space Station
LOC	Lab-On-a-Chip
NASA	National Aeronautics and Space Agency
PDMS	Polydimethylsiloxane
POC	Point-of-Care
rHEALTH	reusable Handheld Electrolyte and Lab Technology for Humans
RGB	Red, Green and Blue
RTD	Residence-Time Distribution

Abbreviations and Symbols:

C	Concentration (mol/m^3)
δ	Ratio of D_H to 2R, $\delta = D_H / 2R$
D	Diffusion Coefficient ($m^2 \bullet s^{-1}$)
De	Dean Number, $De = Re\ \delta^{0.5}$
D_H	Hydraulic Diameter (m), $D_H = 2 \times Area / Perimeter$

I	Pixel Intensity
L	Length of Channel (m)
μ	Fluid Viscosity (Pa•s)
P	Pressure (Pa)
ΔP	Pressure Drop, $\Delta P = 32\ \mu\ U\ L / D_H^2\ r$ (Pa)
Pe	Peclet Number, $Pe = U\ D_H / D$
ρ	Fluid Density (m^3/kg)
R	Radius of Curvature (m)
Re	Reynolds Number, $Re = \rho\ U\ D_H / m$
σ_c	Concentration Variance, $\sigma_c = \langle (c - \langle c \rangle)^2 \rangle^{1/2}$
σ_I	Optical Variance, $\sigma_I = \langle (I - \langle I \rangle)^2 \rangle^{1/2}$
Sc	Schmidt Number, $Sc = \mu / \rho\ D$
U	Average Fluid Velocity (m/s)
U_2	Average Secondary Flow Velocity (m/s), $U_2 = (v^2 + w^2)^{0.5}$

CHAPTER I

INTRODUCTION

1.1 Motivation

The retirement of the National Aeronautics and Space Agency (NASA) Space Shuttle Program in 2011 will hinder the Agency's ability to return biological samples from the International Space Station (ISS) to the ground for analysis. Consequently, Point-of-Care (POC) Lab-On-a-Chip (LOC) technologies have been considered for in-flight blood analysis. However, current Commercial Off-The-Shelf (COTS) systems are not capable of satisfying the unique requirements of an on-orbit blood analysis system. Current POC devices do not provide the breadth of assays that the NASA biomedical research communities require. The devices are also not produced with the mass and volume limitations of space travel as key design drivers. COTS devices also rely on reagents with inadequate shelf life relative to the length of a mission. Aside from providing diagnostic value on current crew onboard the ISS, such a device will be critical for any future long duration space exploration missions to protect the health and safety of the crew. Due to the need for in-flight blood sample analysis, NASA has invested in the development of next-generation medical diagnostic capabilities for which the ISS will be used as a test bed.

This type of technology is also applicable for monitoring and improving healthcare in remote regions and developing countries. NASA's unique requirements have significant

overlap with the needs of the armed forces as well as resource-poor settings. Finally, a device with the breadth and adaptability as discussed here has enormous implications for emergency care, clinical medicine and the care provided by first responders. Reviews of emerging technology for global health applications have concluded that there is an urgent need for new health diagnostic technologies in developing countries. Portable devices are now being used in these settings, but more advances are required to satisfy the needs of more extreme resource-poor settings (Chin, Linder et al. 2007). There is tremendous potential for fulfilling the needs of health-care workers and patients in these remote settings with the research and development efforts in the area of microfluidic LOC diagnostics. As space medicine diagnostic priorities parallel such diagnostics, this development effort would provide a tool to satisfy global health needs as well (Chin, Linder et al. 2007).

Although the precise requirements for such a technology for space medicine are still being defined, there are many needs that have already been identified. The device would ideally be handheld and must have a long operational and shelf life (>1 year), while relying on limited consumables. Current POC devices utilize disposable LOC cartridges with reusable readers. One approach to greatly reduce consumables is to incorporate the microfluidic pathways into the detection infrastructure and reuse them as well (Nelson 2011).

Through the support of NASA, the DNA Medicine Institute (DMI) is utilizing this design paradigm in an effort to develop a universal diagnostic device, which has been designated the reusable Handheld Electrolyte and Lab Technology for Humans (rHEALTH). The rHEALTH device will rely on a microfluidic chip to mix the blood sample with appropriate reagents upstream of the detection region. A flushing cycle will be employed between samples to avoid cross-contamination. The mixing component of the chip is critical to ensure adequate mixing and dilution of the sample, but in order to be reusable certain design constraints must be considered. A more detailed summary of these

constraints can be found in the Biomedical Engineering, Vol. 4, chapter "Design principles for microfluidic biomedical diagnostics for space" (Nelson 2011).

DMI investigated multiple passive micromixer designs that have been documented in literature (Auroux, Iossifidis et al. 2002; Reyes, Iossifidis et al. 2002; Bringer, Gerdts et al. 2004) such as those which rely on splitting and recombining flow and surface patterning to increase mixing. Ultimately, a preliminary design was chosen with a flow path that did not include stagnation zones or obstacles to reduce the risk of fouling or clogging the system. The chosen design utilizes spiral channel to induce transverse flow, which, enhances mixing within a small footprint (Chan 2009).

The NASA Glenn Research Center (GRC) has a collaborative relationship with DMI. GRC has extensive expertise in microgravity fluid physics and provides fluidic expertise to DMI. GRC has developed a microfluidics lab capability that enables rapid prototyping of microfluidic designs. The lab also has microfluidic sensors that provide data, such as flow rate and pressure, for model validation.

1.2 Design Process

An engineering design process generally entails a recursive and iterative cycle as detailed in NASA's Systems Engineering Processes and Requirements (NASA 2009). To ensure a quality product, design controls must be in place as described in the Design Control Guidance for Medical Device Manufacturers provided by the Center for Devices and Radiological Health (CDRH) office of the Food and Drug Administration (FDA 1997). Often, in order to satisfy schedules, concurrent engineering is required which involves carrying out tasks in parallel. Although there is some risk associated with this approach, it is typical in the design process and often yields a higher quality product at a reduced cost.

This approach is being applied to the development of the rHEALTH device, employing a spiral chip and onboard two-channel laser detection of fluorescence. The current efforts

involve: assay development, microchip optimization and sensor design. As each task evolves, new design inputs will be established for the other tasks. For example, as the assay development task progresses, new parameters, such as dilution ratio or overall residence time, may be established for the micromixer as it serves to dilute and mix reagents with the sample. Similarly, the detection component of the chip will likely employ flow focusing. As the detection sensor is developed, parameters for that region of the chip will be further refined. In another example, as the assay development progresses, a mixing threshold will be defined which would specify the mixing quality required for specific analytes. Also required dilution ratios will be defined for the analysis. In order to speed the design process and reduce cost, most of these tasks are being carried out concurrently.

Prototype testing of design components is one part of the design process. In particular, high fidelity custom microchips containing the micromixer will need to be tested. Preliminary design refinement studies will be performed with polydimethylsiloxane (PDMS) chips, but for final system a glass microchip will likely be utilized. Glass chips are chemically nonreactive and have good geometric stability. These high fidelity glass chips can be quite expensive and can take on the order of months to procure. It is therefore prudent to have some prototype testing done prior to making this investment. Having an in-house rapid microchip prototyping capability is therefore an avenue to aid in the speed and cost of the design process. There are inexpensive techniques which have fairly recently been published in which a microchip can be fabricated and ready for testing within a day (Chen, Breslauer et al. 2008; Grimes, Breslauer et al. 2008).

Computational Fluid Dynamic (CFD) modeling is a powerful tool that can also be used to speed product development as opposed to relying on experimental data alone. This is particularly true for microdevices because sensors that may typically be used for obtaining data in larger scale systems are on the same scale as a micro device (Weigl, Bardell et al. 2004). This can lead to interference with operations to a degree that data

obtained can be skewed or useless. For example, if you have flow and pressure sensors integrated into the fluid flow, the added restriction of the flow sensor could lead to higher reading for pressure drop across a channel than if the reading were strictly for the channel. The same issue would arise if one were to rely on the drive pressure of a system for the value of the pressure drop across a microchip. If other sensors were integrated in the flow path or other restrictions were present in the flow path then the drive pressure would not be equivalent to the pressure drop. Measurements are certainly necessary to validate the CFD model, but they are often difficult and expensive to obtain and may provide spatially incomplete data. In addition, experimental data also carries some measure of uncertainty. Modeling allows for the prediction of the fluid behavior within the device. It has been learned from previous *In Vitro* Diagnostic (IVD) endeavors that a combination of prototype modeling and testing is critical for speeding the development process as opposed to relying solely on an experimental approach (Weigl, Bardell et al. 2004).

1.3 Objectives

DMI has performed numerous laboratory-mixing studies in order to develop the basic micromixer design for the rHEALTH device, using blue and yellow dyes to distinguish the incoming fluid streams. The mixing data obtained from the DMI lab studies is strictly limited to a visual record of the color at the upper surface of the flow field. Mixing data was obtained from DMI and will also be used for comparing model results. At GRC, rapid prototyping methods will also be investigated. A high fidelity prototype glass chip will be setup in the lab at GRC and tested. Data obtained from the diagnostic set-up at GRC, which can provide flow rate and pressure drop readings, will be used for model validation. The aim of this study is to develop a computational model, using the finite element method (FEM) software package COMSOL, based on current parameters. The fluids that will be mixed for these initial studies will be two miscible Newtonian fluids. Experimental data will be

compared to the computational model results. The data from the model will be analyzed to provide insight into the mixing characteristics and provide design recommendations. The key design considerations for this effort are minimization of power, size, and fouling potential, while providing adequate mixing of reagents for analysis. Future studies will be identified to employ use of the model as a tool to further the rHEALTH design effort.

CHAPTER II

BACKGROUND

2.1 Microscale Mixing

Fluidic channels in Lab-on-a-Chip (LOC) devices typically have width and height dimensions in the range of 1 to 1000 μm. At these dimensions, with fluid similar in properties to water and at low velocities (< 1 m/s), flow tends to be laminar or flow in which fluid streams are parallel. This flow regime is characterized by low Reynolds numbers, (Re), generally less than 200. The study presented in this effort will focus on flow in the Re range of 8 – 90. Re is a non-dimensional parameter representing the ratio of inertial to viscous forces and is given by:

$$Re = \rho U D_H / m \quad (1)$$

where ρ is the fluid density (m^3/kg), U is the average fluid velocity (m/s), D_H is the hydraulic diameter (m), and μ is the fluid viscosity (Pa•s). The hydraulic diameter is:

$$D_H = 2 \times \text{Area} / \text{Perimeter} \quad (2)$$

The transition from laminar flow to turbulent flow typically occurs above Re = 2300 for internal flow. Turbulent flow exhibits unsteady random motion in space. The significant convective mass transport seen in turbulent flow is associated with rapid mixing, but is generally not applicable for microflows where mixing generally occurs via diffusion and convection at low Re. The Peclet number (Pe) is a ratio of convective to diffusive transport

and is given by:

$$Pe = U D_H / D \quad (3)$$

where D is the diffusion coefficient ($m^2 \bullet s^{-1}$). The ratio between Pe and Re is known as the Schmidt number (Sc) and is given by:

$$Sc = \mu / \rho D \quad (4)$$

At the microscale, the values of Pe are high (>100) which implies that in straight channels, rather long mixing lengths (up to centimeters) are required to achieve complete mixing by diffusion (Nguyen 2008). The length and time required for diffusive mixing are generally impractical for most LOC systems.

In general, there are two approaches for increasing the mixing rate in microfluidic systems: active and passive mixers. Active systems rely on external forces such as piezoelectric elements or micromachined magnetic stirrers. Although active systems enable more efficient mixing, they are more expensive and more likely to fail than passive systems. Passive mixing systems rely on the geometry of the microfluidic pathways to manipulate flow and enhance mixing. Some passive mixers will be reviewed in more detail in the following sections. These systems are generally more rugged and easier to produce than active mixers (Howell, Mott et al. 2004; Hessel, Lowe et al. 2005; Kumar, Paraschivoiu et al. 2011). Active mixers require more power and flow control as well.

Clinical diagnostic reviews have noted that laboratory instrumentation in general is becoming smaller and simpler with time. This of course also implies that fluid handling and analysis is becoming more miniaturized as well. There has been an emphasis to better understand fluid behavior at this scale for further design and development of systems. The miniaturization trend is only expected to continue. Therefore it is important to develop a better understand microscale flows and also ensure appropriate tools are available for design assessment (Schulte, Bardell et al. 2002).

2.2 T-Shaped Micromixers

The simplest passive micromixer is the T-shaped micromixer. It simply consists of two inlets that flow into a long straight mixing channel. A schematic of a T-mixer is shown in Figure 1, where two separate fluids, represented by blue and yellow flow into a junction and a green region represents the area of diffusion between the fluids.

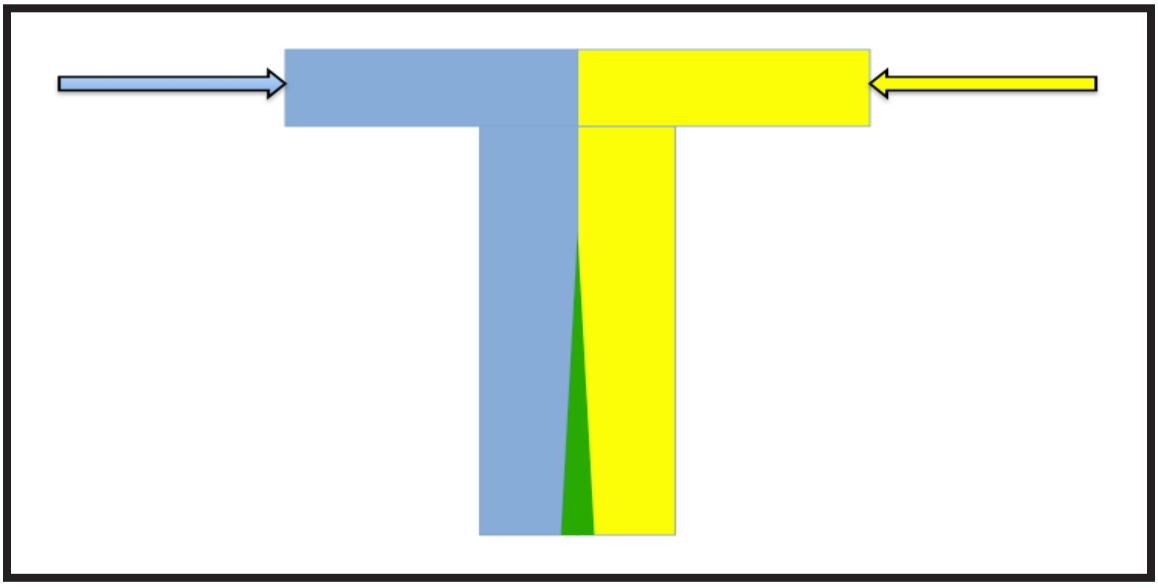

Figure 1: T-mixer showing simple diffusive mixing of two different flows represented by blue and yellow. The green area represents the region of diffusive mixing.

A combined computational and experimental study of laminar flow in a T-mixer has been documented previously (Adeosun and Lawal 2009). The authors observed that there is no established consensus for mixing performance evaluation as microsystem technology is still considered to be in its infancy. They attempt to apply the concept or residence-time distribution (RTD) to indirectly characterize flow and mixing. RTD is often used at the macroscale, but the authors noted that, to their knowledge, implementation at the microscale is novel for characterization. RTD data can be obtained by introducing tracers into the flow field. Tracers not only provide quantitative data, but also reveal qualitative data such as revealing dead zones or regions of channeling. RTD provides information on

the residence times of analytes within each fluid element in a mixer as opposed to a lumped assumption that all fluid element times are equal. A mixer similar to the one shown in Figure 1 was investigated by the authors. Their mixing channel length was 56 mm and the cross section was 400 μm wide by 250 μm deep. The Re range examined was between 10.2 and 20.4, while Pe ranged from 6.84×10^3 to 1.37×10^4. To determine RTD experimentally, the authors used a pulse input method, which involves injecting a pulse of tracers at the inlet. Data for absorbance and concentration were obtained at the inlet and outlet with respect to time. The CFD code FLUENT was used to perform a finite volume-based numerical simulation. A steady state solution was obtained first followed by an unsteady simulation for the tracer species equation. In order to minimize numerical diffusion, which usually arises from the discretization of the governing equations, predominantly aligned volume elements were chosen. The model and experimental data showed good agreement, and the authors propose use of their standardized procedures for future evaluation and comparison of mixing channels (Adeosun and Lawal 2009).

A parametric numerical analysis of a T-shaped micromixer was presented at the 2007 COMSOL Users Conference (Virk 2007). This mixer also looks qualitatively like the one represented in Figure 1. Different aspect ratios were studied with widths ranging from 100 μm to 400 μm and heights ranging from 75 μm to 125 μm. Diffusion coefficients ranged from 1×10^{-10} to 1×10^{-5} m^2/s. This corresponded to a rang of 1 to 1×10^6 for Pe and $Re < 25$. COMSOL was used for the numerical simulation with Dirichlet boundary conditions at the inlet and outlet. Artificial diffusion was applied to stabilize the solution at low diffusion coefficients. The fluid volumes were equivalent for the two fluid types. For channel width, it was observed that smaller channel width exhibited higher diffusive flux due to the increased surface contact between the fluids. This allows for a larger diffusion zone between the fluid streams than channels with larger widths. Generally wider channels required longer mixing lengths than slimmer channels. A similar study was carried out for

varying channel heights, but yielded negligible change in mixing due to channel height. A comparison based on Re was also presented. At low Re, mixing is diffusion-dominated, while at higher Re convective mixing dominates. At higher Re longer mixing lengths are required. At these length scales, the flow can be represented by a parabolic Poisseuille profile, in which the flow is fastest in the center of the channel. It is at the center of the channel that the interface between the two fluids occurs, which leads to reduced residence time of the fluid and therefore reduced opportunity for diffusive transport (Virk 2007).

2.3 Chaotic Mixers

As previously noted, turbulent flow leads to rapid mixing, but is not practical at the microscale. It is difficult to mix solutions in microchannels as the flow is laminar, but a now well-known design, the staggered herringbone mixer (Figure 2), allows for mixing in reduced channel lengths compared to flow in a simple straight smooth channel (Stroock, Dertinger et al. 2002). In Figure 2, it can be seen that the staggered herringbone design utilizes groves in the floor of the channel to induce transverse flows and furthermore induce chaotic stirring. The DNA Medicine Institute tried a similar design, but found it was prone to fouling and although it provides efficient mixing, is not an ideal design for reusability (Chan 2009).

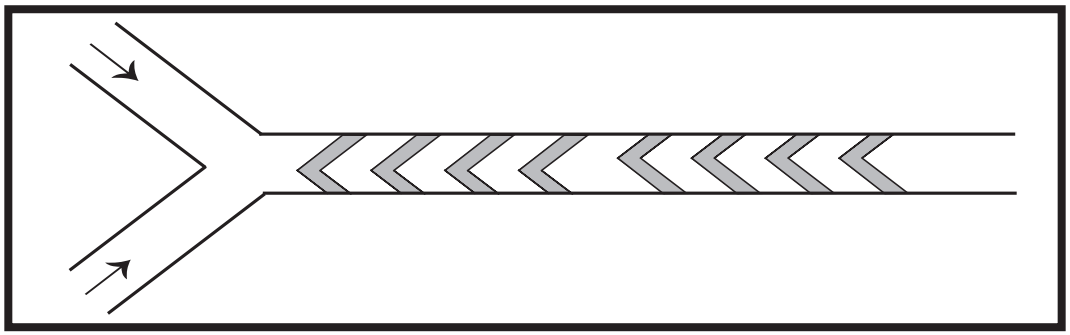

Figure 2: Staggered herringbone chaotic mixer.

2.4 Dean Flow

One passive method to enhance microfluidic mixing, which is the focus of this effort, utilizes the transverse flow field resulting from flow in curved microchannels. Fluid traveling in a curved pipe is pulled radially from the inner wall towards the outer wall. This motion forces fluid near the outer wall to move along the boundaries towards the inner wall. This flow behavior arises from centrifugal effects, inducing counter-rotating vortices known as Dean flow. The illustration in Figure 3 shows a curved rectangular channel with arrows representing the axial flow field and developed Dean flow vortices.

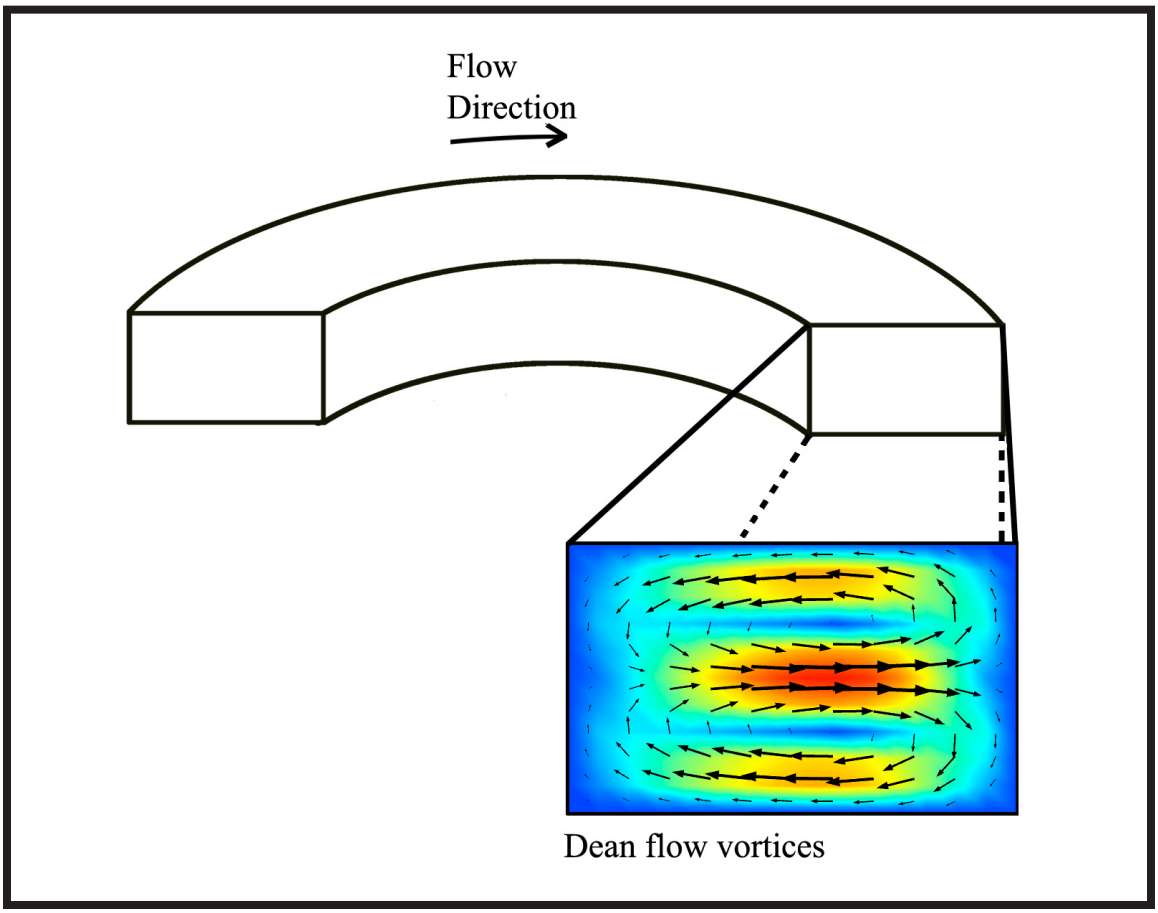

Figure 3: Fluid flow in a curved channel with Dean flow vortices. The cross section surface is colored based on axial velocity magnitude. The arrows also represent axial velocity magnitude and show the pair of Dean vortices.

The dimensionless Dean number, De, characterizes the magnitude of transverse flow:

$$De = Re\ \delta^{0.5} \quad (5)$$

Where δ is the ratio of the hydraulic diameter to twice the flow path radius of curvature. The shape of the secondary flow field changes as De increases. For microchannel flow, De << 100. From of a study of aqueous fluids labeled with dye, in the range of 3.6 < Re < 50.9 (1 < De < 14.2), at low flow rates resulting in De of approximately 1 there was no significant perturbation to the axial flow profile, however at De of approximately 10, counter-rotating Dean vortices appeared in the secondary flow which caused the fluid streams to switch positions (Sudarsan and Ugaz 2006).

Dean flow mixing in curved microchannels appears promising for reusability of channels, which is a major design consideration for space biomedical diagnostics. This design allows for mixing with a continuous uniform flow and without sharp bends, steps, or pockets that could trap bubbles or promote separation zones. The design should be fabricated with smooth walls, as opposed to surface patterning techniques, which increase clogging and fouling risks. A mixing solely based on flow in a curved channel would also not rely on obstruction for mixing which again could increase the likelihood of fouling as well as required pressure drops. In particular with biological samples it is important to minimize residence time of samples near the wall to avoid adhesion of proteins. For these reasons a mixer solely utilizing continuous curved channels would be ideal for the rHEALTH technology.

2.5 Curved Channel Flow Review

One type of passive mixer, with curved channels, utilizing a serpentine flow path and has been well documented in literature. The serpentine design as shown in Figure 4, consists of repetitive curves which leads to enhanced mixing compared to the previously discussed T-mixer in a reduced area. There have been studies of many similar designs with different

variations of this serpentine pattern, which will be discussed in this section (Yamaguchi, Takagi et al. 2004; Sudarsan and Ugaz 2006; Lin and Yang 2007; Ansari and Kim 2009).

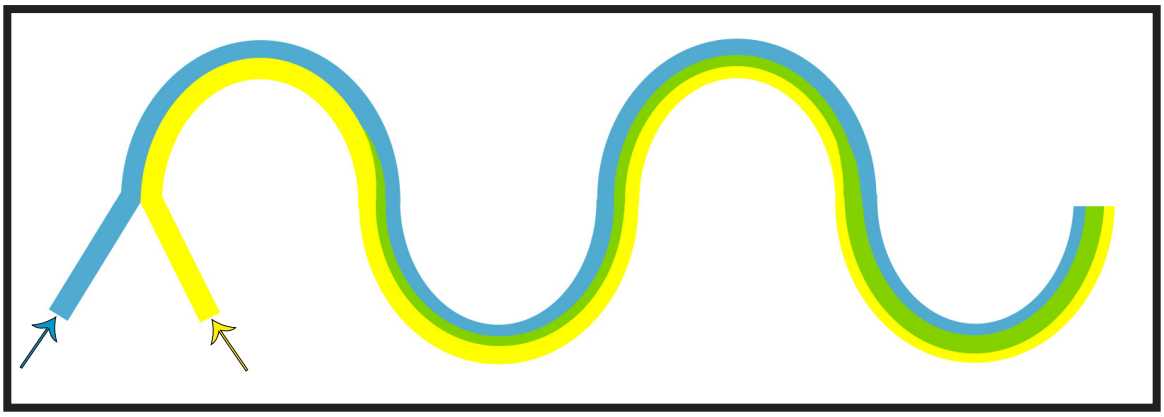

Figure 4: Serpentine channel, with two inlet fluids represented by yellow and blue. Green indicates mixing of the yellow and blue fluids.

A study of the interface between laminar fluid streams in a curved microchannel with confocal microscopy as well as a Computation Fluid Dynamic (CFD) simulation was performed in order to assess the configuration change at the interface between the two fluids (Yamaguchi, Takagi et al. 2004). The 'S' shaped channel design consisted of a long straight channel (200 μm), followed by a 180° turn (with a 500 μm radius of curvature), followed by a long straight channel (200 μm) and another 180° curve (with a 500 μm radius of curvature) in the opposite direction of the initial turn. The channel cross section was 200 μm x 200 μm. The initial interface between flows is straight, but after the first turn it was observed that flow near the central axis, where the velocity is greatest, was forced toward the wall and the peripheral flow was forced inward to compensate. The boundary after the second opposite turn was observed for recovery of the initial straight boundary. The recovery was observed to be incomplete, particularly at higher velocities. It was concluded that comprehension of the three-dimensional behavior of flow, in particular distortions at the fluid interface due to secondary flow, should be considered for optimization of

microchannel designs (Yamaguchi, Takagi et al. 2004).

Another curved channel mixing study included fluid mixing in planar spiral microchannels that were 150 mm wide by 29 mm tall with varied channel lengths (Sudarsan and Ugaz 2006). The investigation involved flow conditions with Re numbers between 0.02 and 18.6. The spiral design included inlet and outlet spirals connected by a central region. Circular arcs were joined with decreasing radius of curvature creating a spiral design. The spiral path allows the secondary flow strength to increase as the fluid travels towards the center of the spiral. This also allows the secondary flow rotation to be sustained, unlike previous serpentine designs in which the secondary flow direction oscillated. Although the serpentine design allows for enhanced mixing over a T-mixer, the spiral mixer yields more appreciable mixing as the fluid interface continues to stretch along the length of the channel. The mixing experiments were carried out by imaging fluid streams with blue and yellow food coloring diluted in water. To quantify the mixing, Adobe Photoshop was used to filter out green so that the mixing interface (green region) could be measured and compared to the channel width. The mixing intensity was then quantified by dividing the width of the mixed interface by the width of the channel. At low flow rates (Re < 1) mixing occurred primarily by diffusion, however the spiral design allowed for mixing to be accomplished in a relatively small footprint. At higher Re (0.02 – 18.6) it was observed that the length required for mixing decreased with increasing Re. The Dean number is proportional to Re and therefore the strength of the secondary flow increases with increasing Re (Sudarsan and Ugaz 2006).

A similar physical and numerical study of mixing in a planar serpentine channel was carried out, but the channels in this study had sharp turns as opposed to the S-shaped curves in the previous paper (Lin and Yang 2007). At different lengths along the flow path the channels converged and diverged which increased the degree of trajectory irregularity. The cross sections ranged from 2 x 2 mm to 4 x 4 mm. This is an order of magnitude larger than

the other channels reviewed. The study was performed for Re of 160. They concluded that rapid mixing was achieved and enhanced due to the flow trajectory irregularities (Lin and Yang 2007).

A three-dimensional serpentine microchannel, with repeating L-shaped units, was investigated using experimental and numerical analysis (Ansari and Kim 2009). The Re range investigated was 1-70. The channel width was held constant at 300 μm, while the other dimensions were varied. The authors noted that although techniques were used to minimize numerical diffusion, it is impossible to yield a simulation free of numerical diffusion, which arises from the discretization of the convection terms in the Navier-Stokes equation. The boundary conditions were set as a normal velocity at the inlet and zero static pressure at the outlet and no slip conditions. A grid independency test was performed based on the concentration variance profile along the fluid path. The study showed that the level of circulation and mixing increased as Re increased from 1-70 (Ansari and Kim 2009).

Many studies have been performed with passive micromixer designs and in particular, those based on enhanced mixing from Dean flows in curved channels. It is of interest to note that in the literature the method for measuring and quantifying mixing is inconsistent and remains challenging. Mixing studies range from use of food coloring to observation of chemical reactions at the mixing interface. Also some of the imaging techniques utilized may have varying results depending on the orientation of the imaging of the fluids studied (Nguyen and Wu 2005). Ultimately, the spiral mixer design appears to be a promising method to mix fluids in a small footprint with minimal fouling risks.

2.6 Prototype Chip Fabrication

Prototype microfluidic chips are often used for design refinement during the development process in order to assess different designs and provide a better understanding of any design related issues. The chips are fabricated with a variety of techniques and

materials. The techniques are generally divided into ‘hard’ and ‘soft’ depending on the materials and procedures. Depending on the process and fidelity requirements, the time range for fabricating a prototype can be from within a day to months. The first step in this process is to develop a design or model usually assisted by a computer-aided design (CAD) package. It is also important to consider design constraints imposed by the fabrication method. For example, some of the quicker and cheaper prototype methods have limitations on minimum and maximum channel dimensions. The designer would therefore need to take this into account when specifying the dimensions or consider a different prototype method (Saliterman 2006).

One of the least expensive and quickest procedures utilizes shrink film and a laser printer (Grimes, Breslauer et al. 2008). The shrink material is purchased as polystyrene sheets that are preformed and under tension. When they are heated above their transition temperature, they shrink and return to their original size. In this procedure, channel designs are first generated using CAD software and then printed onto the polystyrene thermoplastic sheets using a laser jet printer. The printer resolution can be adjusted to smooth the edge features of the design. In order to achieve a taller channel dimensions, the sheets can have the pattern printed on them repeatedly, which raises the ink level. Once printed, the sheets are cut into smaller pieces (for less distortion during the shrinking process) and placed in a pre-heated oven for about 5 minutes at 163 °C. During the shrinking process the height of the ink is raised from the surfaces, while the overall dimensions of the design are reduced approximately 60%. The shrunk pattern can then be used as a mold for an actual chip. Polydimethylsiloxane (PDMS), a typical soft lithography material, can then be poured onto the mold and cured. Once cured, the PDMS can be peeled off of the mold and bonded to a glass substrate to close the channels and rapidly yield a prototype microfluidic chip (Grimes, Breslauer et al. 2008).

Another inexpensive and rapid prototyping technique, developed in the same lab as

the previous method, allows for 3D chip fabrication (Chen, Breslauer et al. 2008). This technique also relied on exploiting the shrinking properties of pre-stressed thermoplastic sheets, but instead of using the shrunken sheets as a mold, they are instead used as the actual channel. This technique was found to be even faster than the previous method as PDMS is not used and the curing step is therefore eliminated. As opposed to printing a design on the sheets, in this method the design was scribed into the surface with the material being removed in the channel locations. The sheets are then shrunk resulting in thinner and deeper channels. To create 3D chips layers of shrink sheets are stacked on top of each other before shrinking. When shrunk in this manner, an irreversible cross-linking occurs. Scribing was performed manually, but could be adapted to a milling machine or computer controlled plotter for greater design control (Chen, Breslauer et al. 2008).

The two previous methods discussed work well for creating chips with channel dimensions in the range of tens to hundreds of microns. If smaller channel dimensions with smoother features are needed, then a different manufacturing process will be required. In soft lithography techniques, the mold dictates the resolution of the channel dimensions. One method to generate higher fidelity masters than the shrinky dink method is to use photolithography. In this process a substrate, such as silicon, is cleaned and spin coated with photoresist. The depth of the channel mold is determined from the thickness of the coating. A photomask is then used during the UV exposure step. The mask prevents light from reaching the photoresist in the design pattern region of the desired channels. The photoresist is then silanized resulting in a mold which can be used as a mold for a PDMS chip similar to the previous methods described (Saliterman 2006).

Although PDMS chips work well, particularly in early stages of the design process, there are advantages to using chips made of different materials as well. In the development effort discussed in this effort, a silica chip will also be used. Silica chips are preferable when fluorescence techniques are involved as PDMS exhibits autofluorescence. Silica chips are

chemically inert, impermeable to gases, and exhibit better geometric stability over time than a PDMS chip. There are multiple vendors that will fabricate custom glass microfluidic chips. These types of chips are significantly more expensive than PDMS chips and for this effort were not purchased until after numerous PDMS chips had been tested (Chan 2009).

CHAPTER III

MICROCHIP PROTOTYPING AT GRC

3.1 Shrinky Dink Method

As discussed previously, an inexpensive, simple, and quick microchip fabrication procedure has been developed that utilizes shrink film and a laser printer (Grimes, Breslauer et al. 2008). This method is often referred to as the 'Shrinky Dink" method as the shrink film used is also sold as a children's toy by that name. Figure 5 shows a picture of a PDMS chip that was created by this method. Water with yellow and blue food coloring can be seen flowing in the inlets. The innermost spiral has a wave appearance in Figure 5, but this is just an optical illusion do to shadows. For this procedure, channel designs are first generated using CAD software and then printed onto the shrink sheets using a laser jet printer. The sheets are then shrunk down to create a mold into which PDMS is poured, creating a chip. The procedure is outlined in more detail below.

Microchannel designs were first created using AutoCAD. As the unshrunk film is 2.5 times larger than the shrunk film, the AutoCAD designs are therefore first created at the desired design size and then scaled up 2.5 times before printing. The sheets were then placed on an aluminum tray in an oven preheated to 160°C. As the sheet heats up, the plastic polymer molecules begin to realign. Initially the sheet curls up and then flattens out into a shrunken version. If the shrinking resulted in a slightly less than flat form, then a flat

piece of aluminum was gently pressed onto the sheet to flatten it. Figure 6a and b show the thermoplastic sheets before and after shrinking.

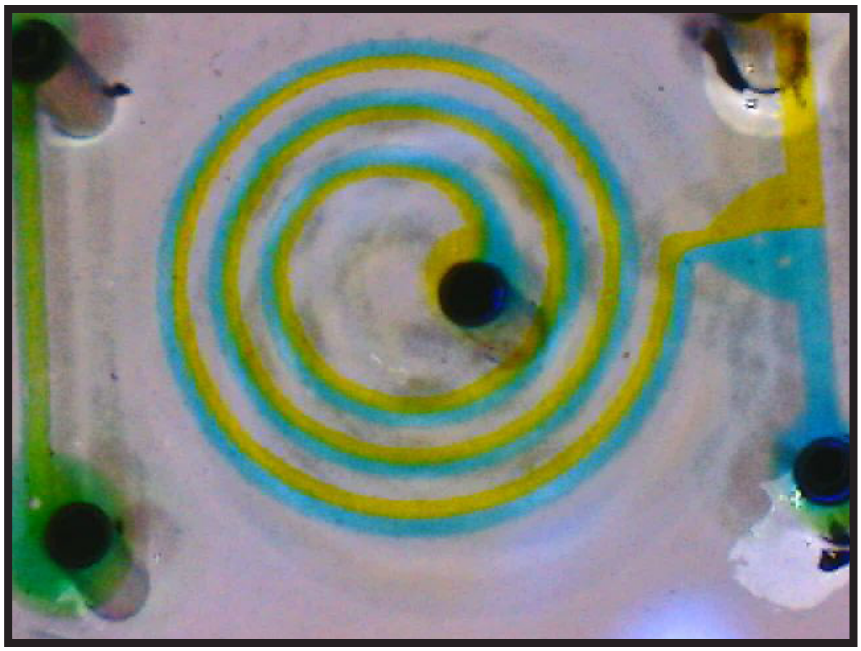

Figure 5: PDMS chip created using the shrinky dink method. Water with yellow and blue food cloring can be seen flowing through the inlets and inth the mixing spiral.

A custom holder was built to hold the shrunken patterns. This allowed for reproducible chip production. Previously the shrunken sheet was placed in a hand formed aluminum foil shaped tray and cut down by hand using a razor blade. This method provided inconsistent chip size and height and therefore a holder was built as can be seen in Figure 6c. In Figure 6d, the pattern has been secured in place and a curable silicone, PDMS, has been poured over the patterns. The PDMS comes as two components, GE RTV 615A and 615B, which are combined and thoroughly mixed just prior to pouring into the molds. The 615B component is the curing agent and is at a ratio of 1:10 with the RTV 615A. The mixing process results in many tiny air bubbles in the PDMS. In order to remove the bubble before

pouring into the mold, the mixed PDMS is placed in a vacuum chamber for 30-45 minutes. Once the PDMS is clear of bubbles it is poured onto the shrink pattern.

The holder, with shrink pattern, and PDMS are then placed in an oven at 175ºC for 1½ - 2 hours for curing. After curing and cooling down the PDMS chip can be removed from the form. The resulting PDMS chip now has an imprint or stamp of the desired design. In order to complete and close the fluid pathway, the chip is sealed with a glass cover slip. The bonding of the PDMS chip to the glass cover slip is accomplished through the use of a plasma cleaner (Figure 6e), which activates the surface of the glass cover slip and the PDMS for bonding. They are both placed in the plasma cleaner for 1 minute after which the chip is quickly pressed against the cover slip. The plasma treatment causes the surfaces to become hydrophilic which helps with the initial chip priming. A completed chip can be seen in Figure 6f.

Although this technique was used to successfully generate chips, the channel height dimension was limited to 30 to 50 μm. An attempt to print layers of ink on the shrink film was unsuccessful due to alignment issues. The micromixer in this study has channels close to 100 μm in height, which allows for full Dean flow vortex formation. Although this capability will be useful for prototyping other geometries, the mixing chips produced in this manner were not used for model validation.

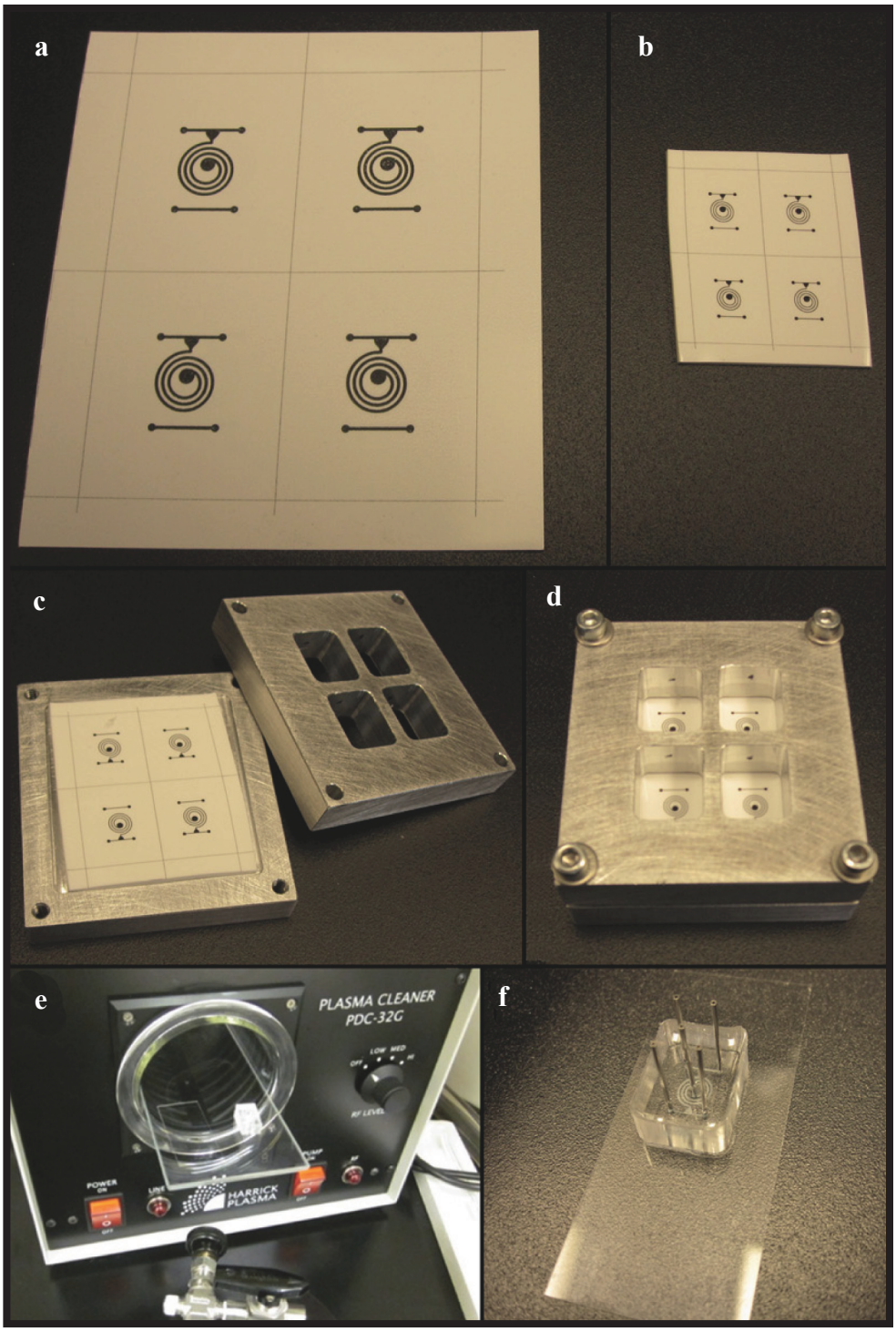

Figure 6: Overview of shrinky dink chip fabrication. a) Pre-shrunk pattern. b) Shrunk pattern. c) Pattern in holder. d) PDMS curing. e) Chip and coverslip being placed in plasma cleaner. f) Chip bonded to glass coverslip.

3.2 3D Shrink Film Milling Method

A similar technique, also discussed previously, also involves the use of pre-stressed thermoplastic sheets. As opposed to printing a pattern on the shrink film, a pattern is etched into the surface (Grimes, Breslauer et al. 2008). After shrinking, the etched region becomes the microchannel. This technique is even faster than the previous method as PDMS is not used and the curing step is therefore eliminated. Although the patterns were etched manually in the article, it was noted that this method could easily be adapted to use with a milling machine.

As can be seen in Figure 7, a computer numerically controlled (CNC) milling machine was used to etch the spiral design pattern in the thermoplastic sheets. The sheet was held in place via a vacuum. Once the patterns were etched, the sheets were cut down into individual chip patterns. To complete the channel for this method a second thermoplastic sheet was adhered to the patterned sheet with superglue before being placed in the oven. Figure 8 shows the adhered thermoplastic sheets shrinking in the oven. Shrinking the films in this manner leads to an irreversible cross-linking. The channel is thus completed via this strong binding.

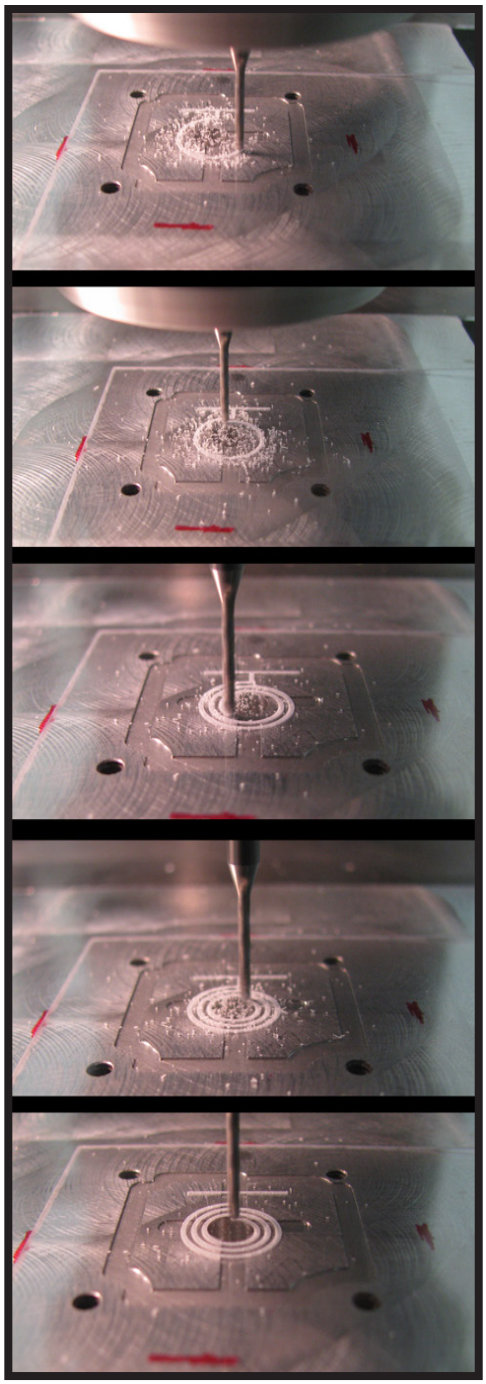

Figure 7: Automated spiral pattern generation by pre-programmed milling machine.

Channel dimensional control was also found to be challenging for this method. The depth was again the issue, however for this technique, the channel depth was generally too deep. The depth of the etching from the CNC milling machine determines the channel depth. The mill used had computerized control in the x-y direction, however the z control was manual. It was found to be very difficult to set the mill so that it would just barely etch the surface. The depth grows 6 ¼ times after shrinking from the original etched depth. For example, if a 100 μm channel is desired, then the etching depth would need to be 15 μm. The manual controls were not adequate to create such a shallow channel so precisely. Another issue with depth was the stability of the sheet during the drilling process. Even with vacuum stabilization, the sheet was not stable in the z-direction. There was therefore more variation in the continuity of the channel depth than in the previous technique, however both presented issues in resolving this dimension in the range of interest for this study. Nevertheless, this technique resulted in successful microfluidic

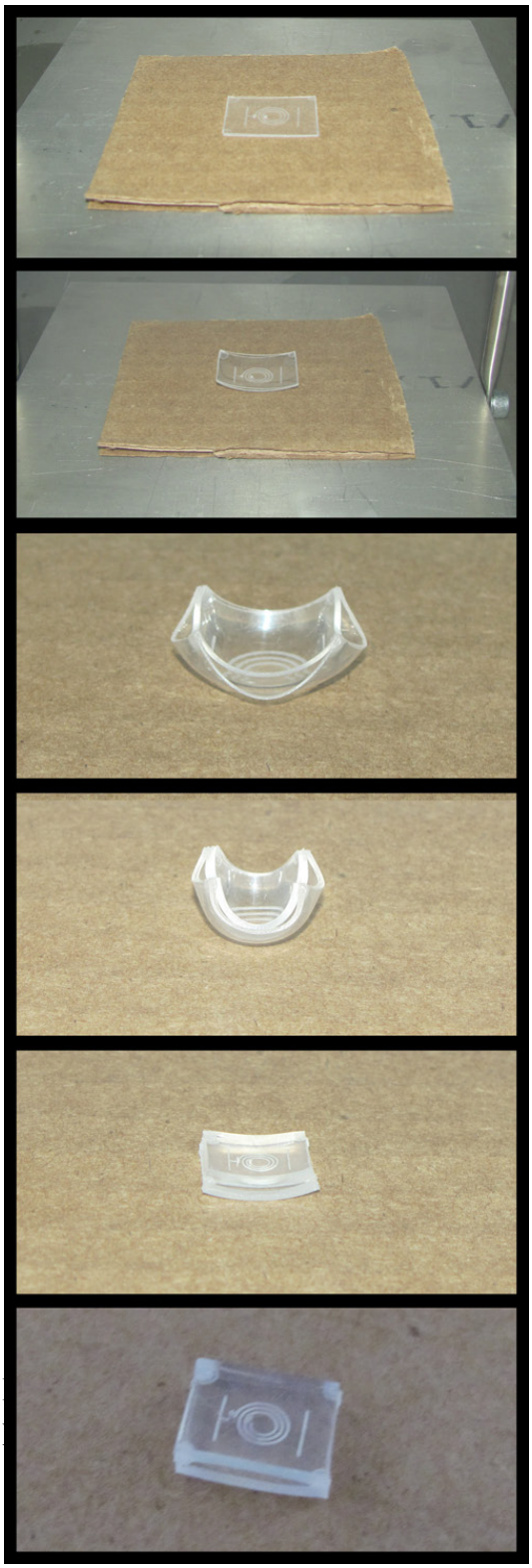

Figure 8: Milled and adhered thermoplastic sheets shrinking in oven.

chips and will be used for studies and prototyping when the desired channel dimensions fall within the tolerances of this method. The final design, however, should be made with a process that has much better tolerance control.

CHAPTER IV

GRC EXPERIMENTAL DATA

4.1 Glass Chip Experimental Set-up

After testing many PDMS chip designs, the DNA Medicine Institute had a set of glass chips made for further testing. One of those chips was delivered to the Glenn Research Center and an experimental setup was used to obtain hydrodynamic flow data for the model validation (Brown 2011). The main components of the experimental test setup (Figure 9) were: a pump, pressure transducers, and a flow meter. The pump (Figure 9a) is a Mitos P-Pump from Dolomite and is designed specifically for microfluidic applications. It has a glass chamber where vials of liquid, with tubing, can be placed. The pump has a feedback control system that maintains a set pressure specified by the user. After the pressure is set, the glass chamber is pressurized which forces fluid from the vials through the tubing. Pressure transducers were incorporated into the flow loop before each inlet and out the outlet (Figure 9b and c). As mentioned previously, measurements at this scale can be difficult and costly. As an example, there were no pressure sensors commercially available that were suitable for this setup, so custom sensors had to be purchased. The custom pressure sensors used in this setup were procured from Dolomite as well. These sensors were placed as close to the chip as was reasonable in order to obtain measurements for the pressure drop across the chip. To avoid affecting the data for pressure drop across the glass chip (Figure 9d),

the flow sensor (Figure 9e) was placed after the final pressure transducer. The flow meter is a Microfluidic Flow Rate Sensor from Dolomite. The glass chip can be seen in Figure 10.

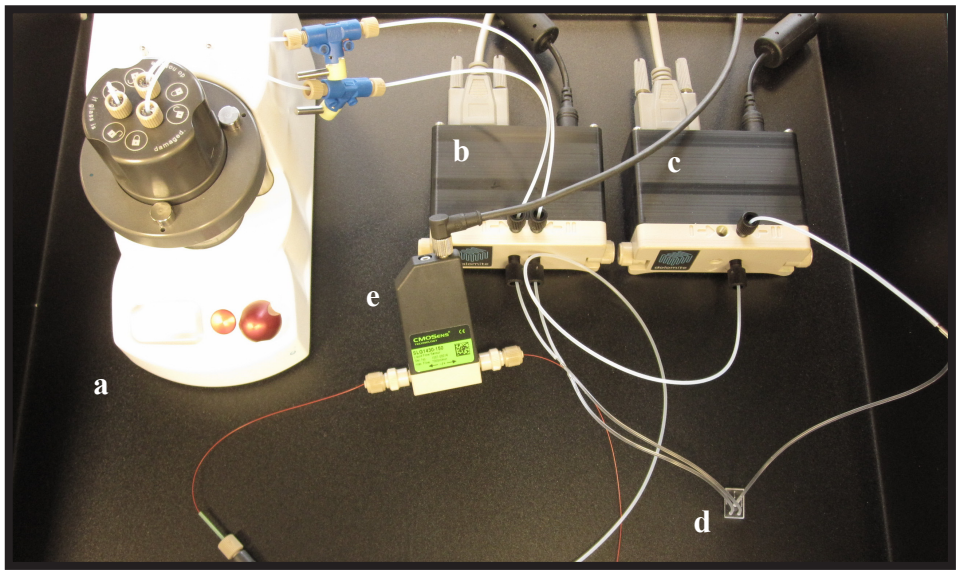

Figure 9: GRC experimental set-up with glass chip. a) P-pump. b) and c) Pressure transducers. d) glass chip.

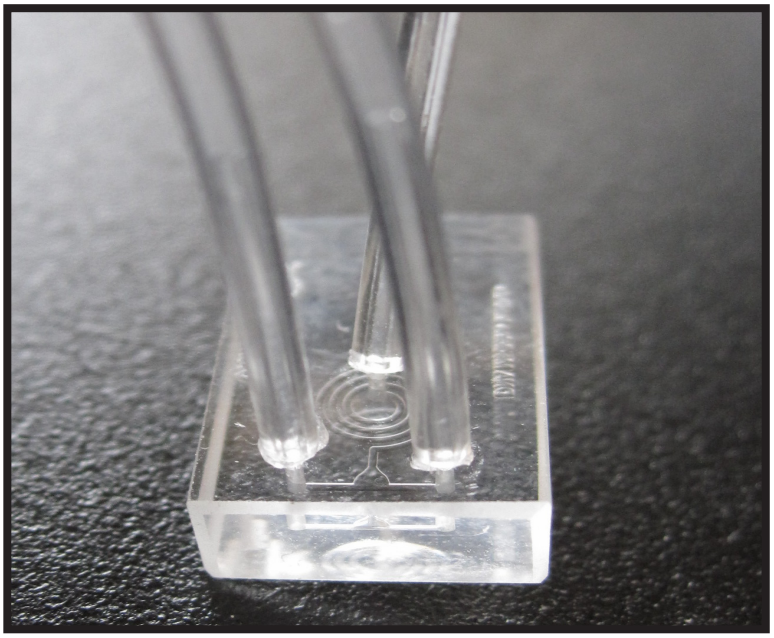

Figure 10: DMI glass chip tested at GRC.

4.2 Glass Chip Experimental Results

Pressure and flow data were recorded for a range of driving pressures. From this data, a plot was generated of Re versus pressure. The data was then plotted against theoretical calculations for pressure drop in a pipe (assuming no-slip, incompressible, viscous flow) from the Hagen Poiseulle equation for fully developed flow in a circular pipe:

$$\Delta P = 32\ \mu\ U\ L\ /\ D_H^2\ \rho \qquad (6)$$

Where P is pressure (Pa) and L is the channel length (m). The plot, presented in Figure 11, shows that there is good correlation between the two data sets.

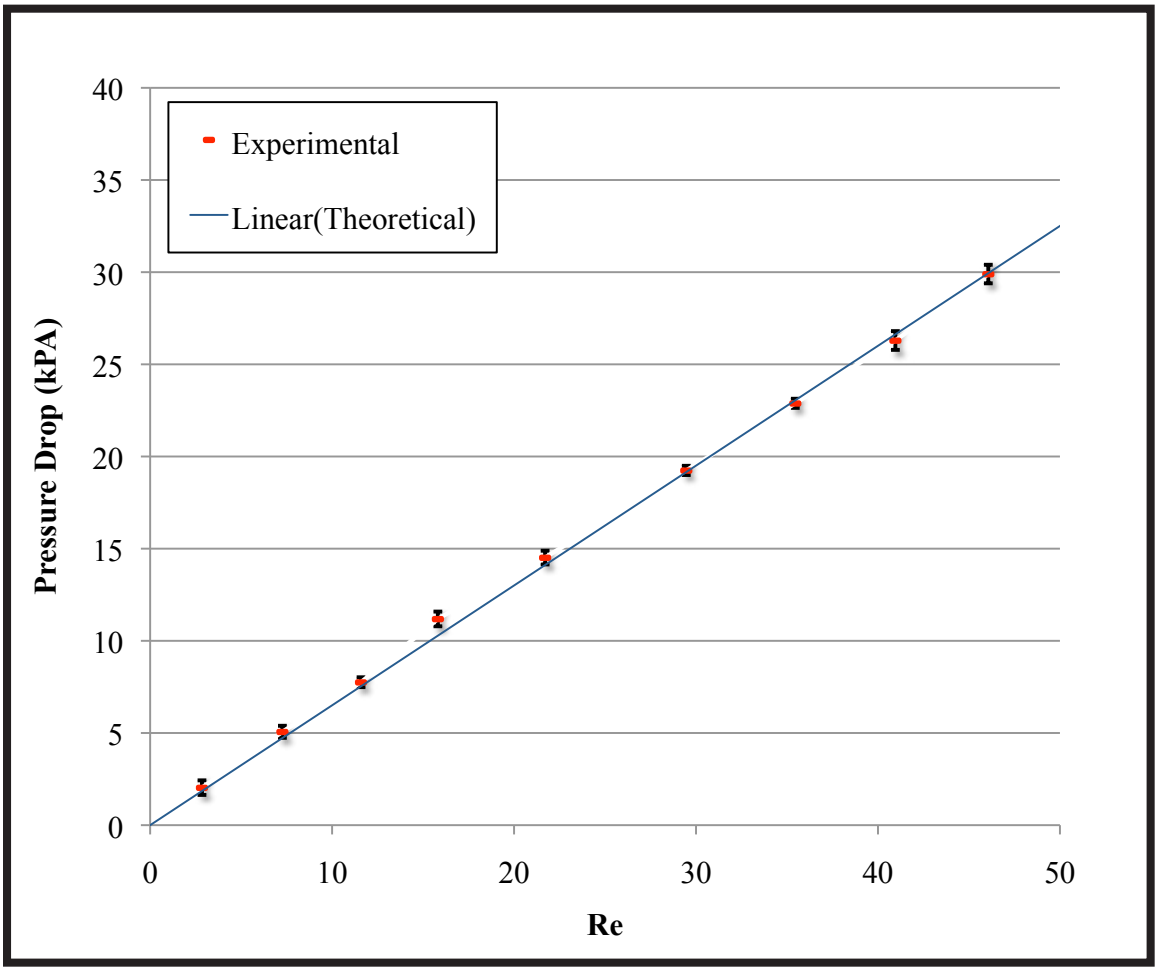

Figure 11: Experimental and theoretical plot of Re versus pressure drop (+/- 2SD) for glass chip.

CHAPTER V

DMI Experimental Data

5.1 Dye Mixing Experiment

The DNA Medicine Institute obtained data from a dye mixing experiment in order to assess their preliminary spiral micromixer design. The cross section of the channel had a width of 200 μm and height of 120 μm. Soft lithography methods were used to make the PDMS chips, which were bonded to a glass slide and mounted on a stereomicroscope for analysis (Figure 12). The flow path on the chip has two inlets that meet and enter into the spiral mixer. The spiral channels are made connecting by half circles (see Figure 13). The outer radii of the six half circles for the spiral chip were: 2.0 mm, 1.8 mm, 1.6 mm, 1.4 mm, 1.2 mm, and 0.95 mm. Blue and yellow food coloring (1:1 in Phosphate Buffered Saline) were used for the dye mixing experiments. Flow was actuated by a miniature air pump. The study investigated Re from 10-70.

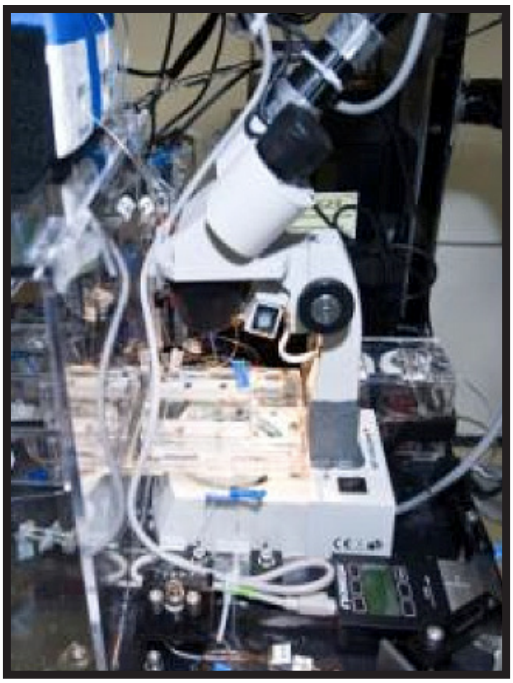

Figure 12: Stereomicroscope mixing experiment set-up.

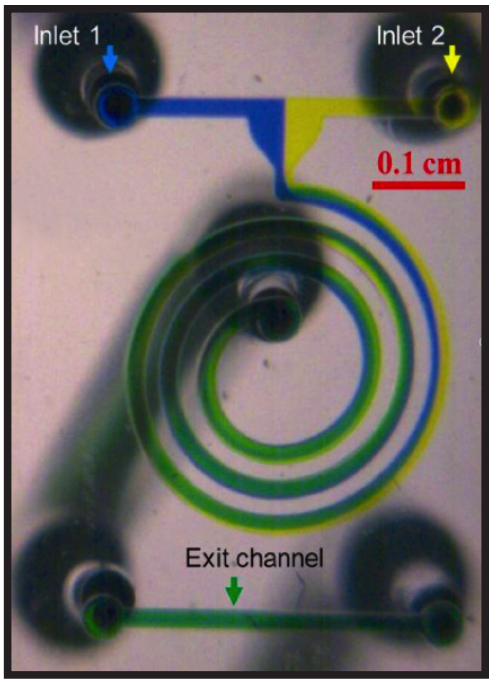

Figure 13: Blue and yellow dye mixing chip.

5.2 Dye Mixing Analysis

Image processing techniques were used to analyze the samples for quantitative evaluation of mixing. Raw RGB (Red, Green, and Blue) images were acquired and then converted to grayscale. Mixing was quantified at the five locations: the inlet, spiral 1, spiral 2, spiral 3, and the outlet. Figure 14 shows an example of a raw RGB image, a grayscale image, and the locations where mixing was assessed. The optical variance, σ_I, was calculated based on pixel intensity:

$$\sigma_I = \langle (I - \langle I \rangle)^2 \rangle^{1/2} \qquad (7)$$

where I is grayscale intensity between 0 and 1 and $\langle I \rangle$ is the spatial average intensity across the sample. Theoretically an unmixed sample would have a value of 0.5 and a completely mixed sample would have a value of 0.0. A value for sufficient mixing will need to be determined experimentally and will depend on the assay and analyte of interest.

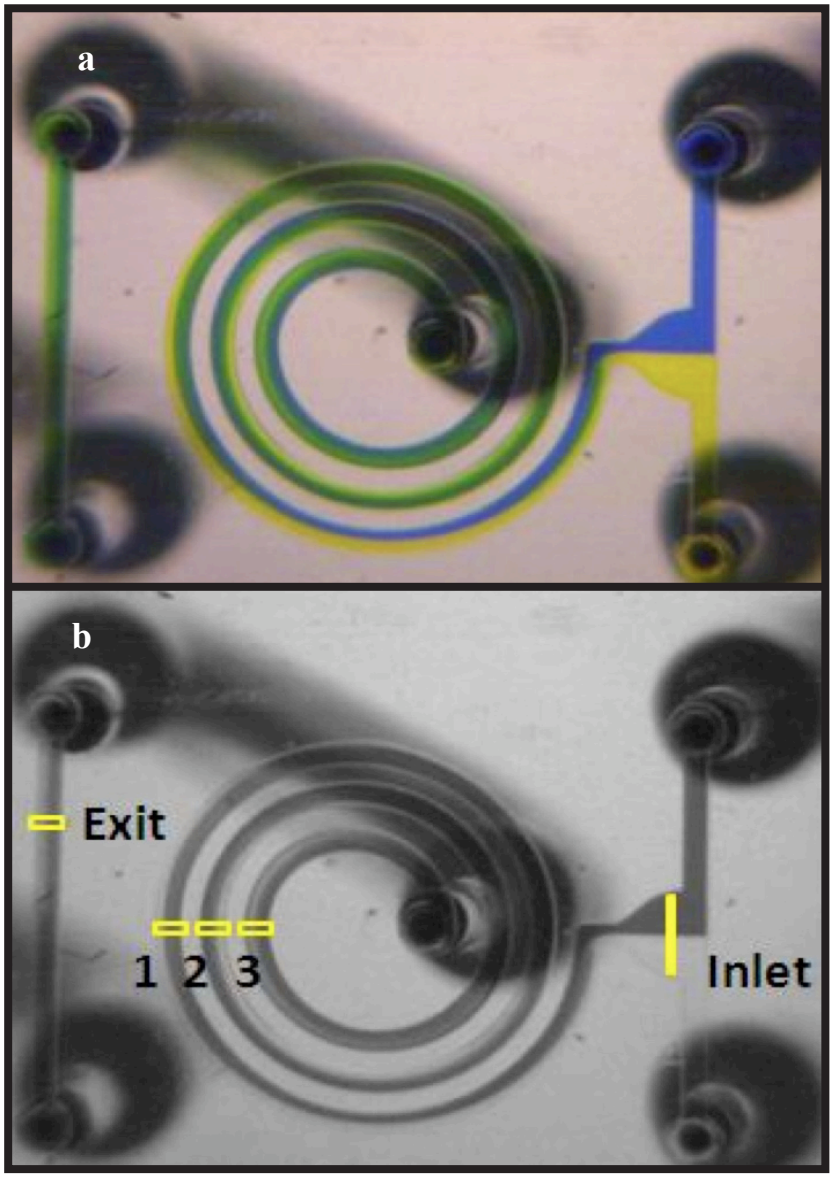

Figure 14: a) Raw RGB image. b) Image converted to grayscale. Locations were mixing was assessed are labeled in the grayscale image.

5.3 Dye Mixing Experiment Results

The value for σ_I at the inlet for all test cases was between 0.4 and 0.5. Theoretically the inlet value would be 0.5 for no mixing and 0.0 for complete mixing. It should be noted, as is evident in Figure 15, there is a plenum at the inlet that was not included in the numerical model. Mixing upstream of the spiral inlet and experimental error would contribute to deviations form the theoretical value. The value decreases at each consecutive spiral, but the trend is not monotonic. This is due the transverse rotations of the flow resulting from the Dean effect. Dean flow effects are evident from reversal of the location of each fluid. In the RGB (Red, Green and Blue) image for Figure 14, if one looks closely, it is apparent at the outer spiral that the yellow fluid is flowing along the out diameter of the flow path, however by the next spiral the yellow fluid is flowing along the inner diameter. In these images it appears that the colors have flipped. This is a result of the secondary flows generated by the centrifugal forces that characterize Dean flow. The 2D image from the top of the chip only provides partial assessment of the process and therefore leads to an inconsistent in the σ_I value. For this method of assessing mixing, mixing can be considered complete when σ_I approaches zero and remains below the desired precision. See Figure 15 for RGB mixing images and Figure 16 for a plot of Re versus σ_I (Chan 2010).

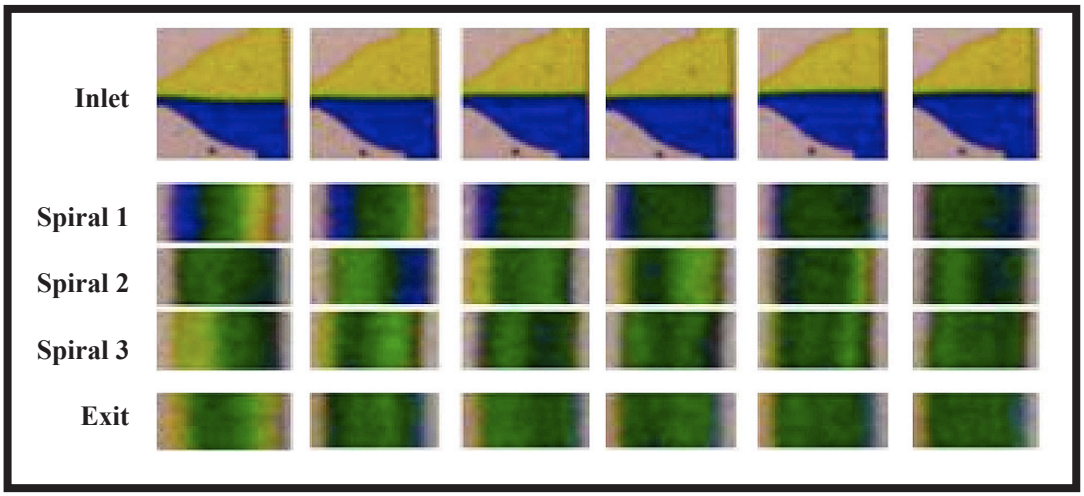

Figure 15: DMI PDMS chip mixing images.

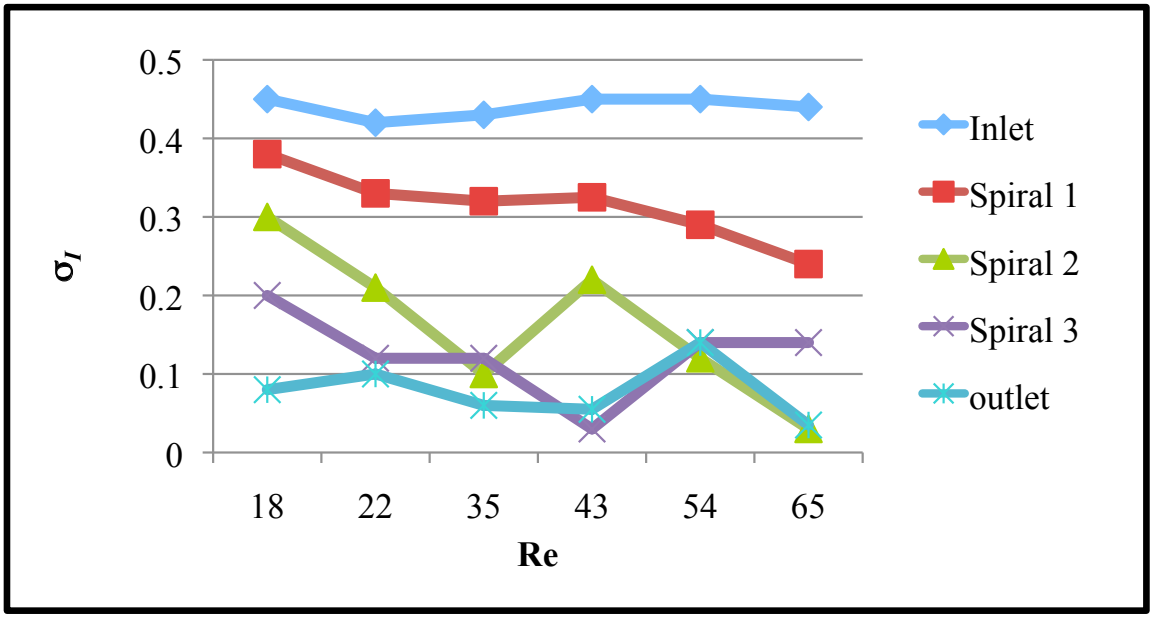

Figure 16: Plot of Re verses σ_I for DMI PDMS spiral mixing chip.

CHAPTER VI

NUMERICAL ANALYSIS

6.1 Computational Modeling Overview

The first step in computational modeling of a physical process is the problem formulation. This involves determining the appropriate mathematical model to describe the physical problem. The model will include: the geometry (domain), governing equations, boundary conditions, initial conditions, and other specified properties and parameters. The computational domain or geometry should be chosen with caution. The problem should be simplified in order to fit within computing resources, but should not be oversimplified, which could lead to loss of fidelity through neglecting relevant physics.

Governing equations are selected based upon the physics present in the problem. For example a given problem might involve: fluid flow, heat transfer, mass transfer, or a combination of processes. Once the governing equations are identified consideration should be given to simplification. The governing equations and computational domain will dictate the number and type of boundary conditions required. Boundary conditions describe the relationship between the model boundary and its exterior surroundings and are required to find a solution as they provide enough data to evaluation of the unknowns. Finally, material properties and parameters are required. Once the model is formulated, a CFD software package can be used to solve the equations (Datta and Rakesh 2010).

6.2 Finite Element Method Overview

The Finite Element Method (FEM) is one mathematical method commonly used for solving engineering and physics problems. The FEM approach solves the governing equations for the system in spatially discrete elements. Each element has a fixed number of nodes that define the element boundaries and connect the elements. Functions are defined within each element with unknown variables at each nodal point. A representation of examples of 3D elements with connecting nodes is shown in Figure 17. A system of algebraic equations for the unknown nodal values can then be solved simultaneously to yield a piecewise approximation of the continuum solution. An example of this is shown in Figure 18. A blue line represents the continuum solution, and the green and red plots represent multiple piecewise approximations. It is evident that as the number of elements increases, the approximation approaches the actual solution. It is also apparent that the shape of the elements and locations of nodal points can effect how well the numerical results approximate the solution. Ideally the error in the approximation approaches zero as the number of elements approaches infinity (Logan 2011). In this study, the COMSOL Computational Fluid Dynamic (CFD) code was chosen as the numerical backbone for solving the steady incompressible Navier-Stokes equation and species transport.

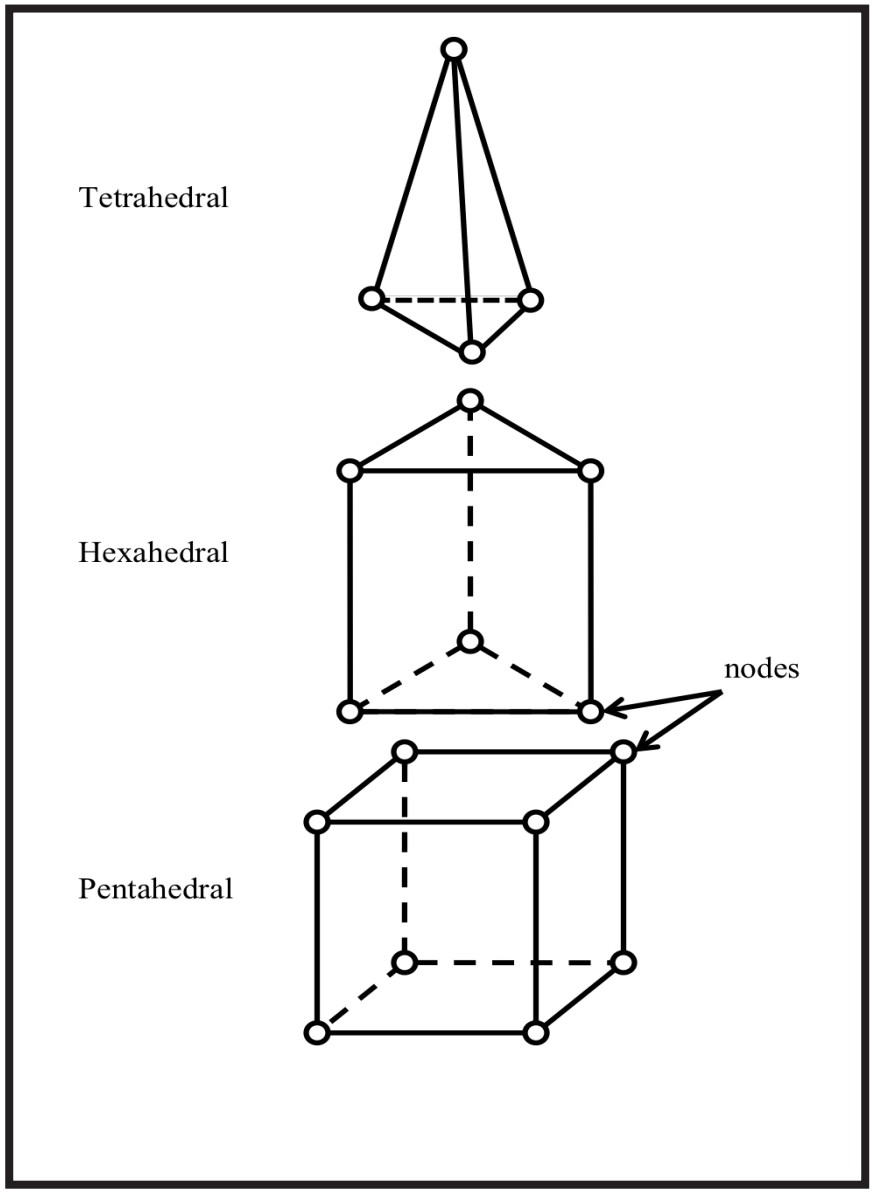

Figure 17: 3D FEM element examples.

Nodes, which connect elements, are pointed out.

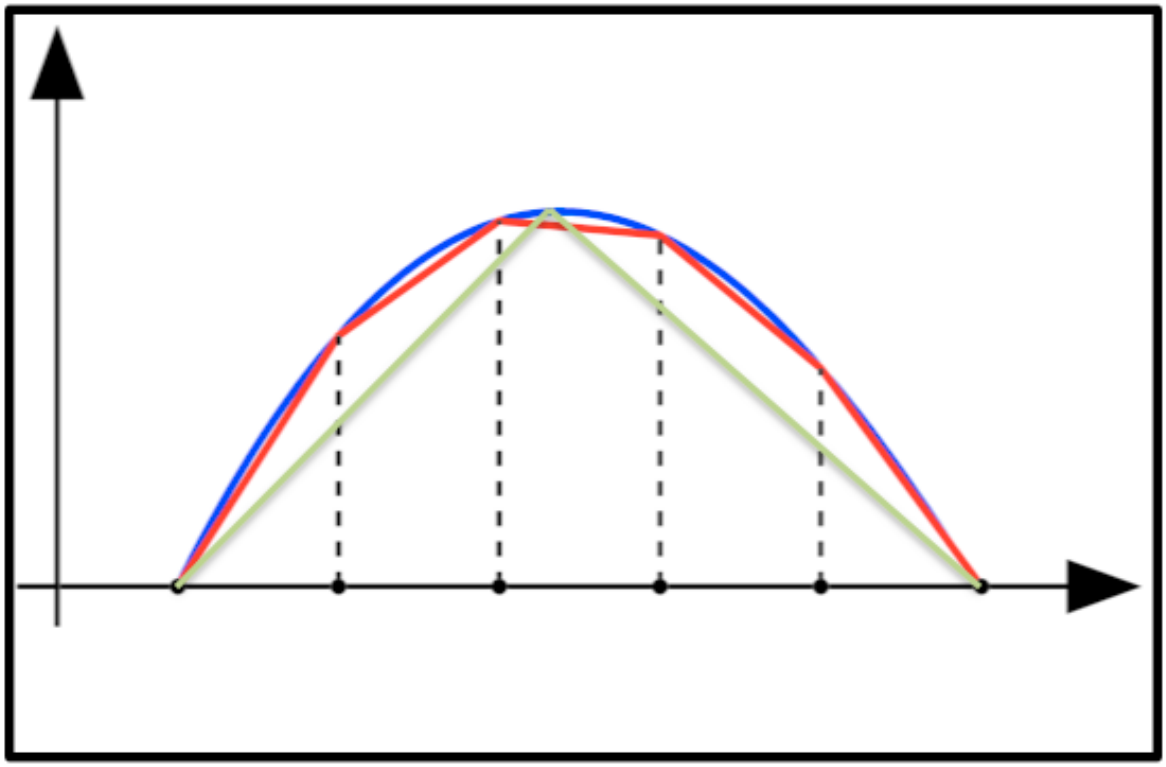

Figure 18: The FEM uses a piece-wise approximation of a function. The blue line represents the actual function, while the red and green lines show piece-wise approximations. It is evident that more pieces or elements will lead to a closer approximation of the function.

6.3 Model Parameters

Three different geometries were modeled for this mixing study: a T-mixer, and two spiral mixers. The T-mixer (case 1) had identical cross sectional dimensions and channel lengths to DMI's PDMS chip. One of the spiral mixers (case 2), was modeled after the glass chip discussed in chapter IV. The other spiral mixer (case 3), was modeled after DMI's PDMS chip, which was presented in Chapter V.

For all models, the fluid properties of water were used (ρ = 1000 kg/m^3, ν = 1x10^{-3} Pa•s). The diffusion coefficient was set to 5x10^{-9} m^2/s, which is on the order of the diffusion coefficients of electrolytes in water (Nguyen 2008). A step function at y = 0 was used in COMSOL to define the concentration at the inlet. For y < 0, the concentration was set to 0 and for y > 0, the concentration was set to 1. For all three geometries, five inlet flow velocities were analyzed: 0.05 m/s, 0.08 m/s, 0.2 m/s, 0.4 m/s, and 0.6 m/s. These velocities corresponded to a Re range of 8-90, which covers the range of experimental data from DMI. The outlet pressure was specified to be 0 Pa and a no slip boundary condition were set for the walls. These parameters are summarized in Table 1.

The T-mixer channel (case 1) had a cross section with a width of 200 μm and height of 120 μm. The channel length was 26.2 mm. A schematic for this geometry is shown in Figure 19. The geometry for case 2, the glass chip (Figure 21), was defined in COMSOL based on glass chip design that was tested at GRC. The cross section of the channel had a width of 250 μm and height of 100 μm. The spiral is made from connecting half circles. The outer radii of the six half circles for the spiral chip were: 2.0 mm, 1.8 mm, 1.6 mm, 1.4 mm, 1.2 mm, 1.0 mm and 0.8 mm. The geometry for case 3, the DMI PDMS spiral mixer (Figure 20), was defined in COMSOL based on the chip design that DMI had used to perform mixing studies. The cross section of that channel also had a width of 200 μm and height of 120 μm. The spiral is made from connecting half circles. The outer radii of the six half circles for the spiral chip were: 2.0 mm, 1.8 mm, 1.6 mm, 1.4 mm, 1.2 mm, and 0.95 mm.

Table 1: Mixer Model Parameter Study

Fluid Properties	$\rho = 1000\ kg/m^3$ $\nu = 1x10^{-3}\ Pa \bullet s$ $D = 5x10^{-9}\ m^2/s$
Inlet Concentrations	For $y < 0$, $c = 0$ For $y > 0$, $c = 1$
Inlet Velocities Analyzed	0.05 m/s, 0.08 m/s, 0.2 m/s, 0.4 m/s, and 0.6 m/s
Outlet Boundary Condition	P = 0 Pa No slip at walls
Reynolds Range Dean Range	8 – 90 0 - 23

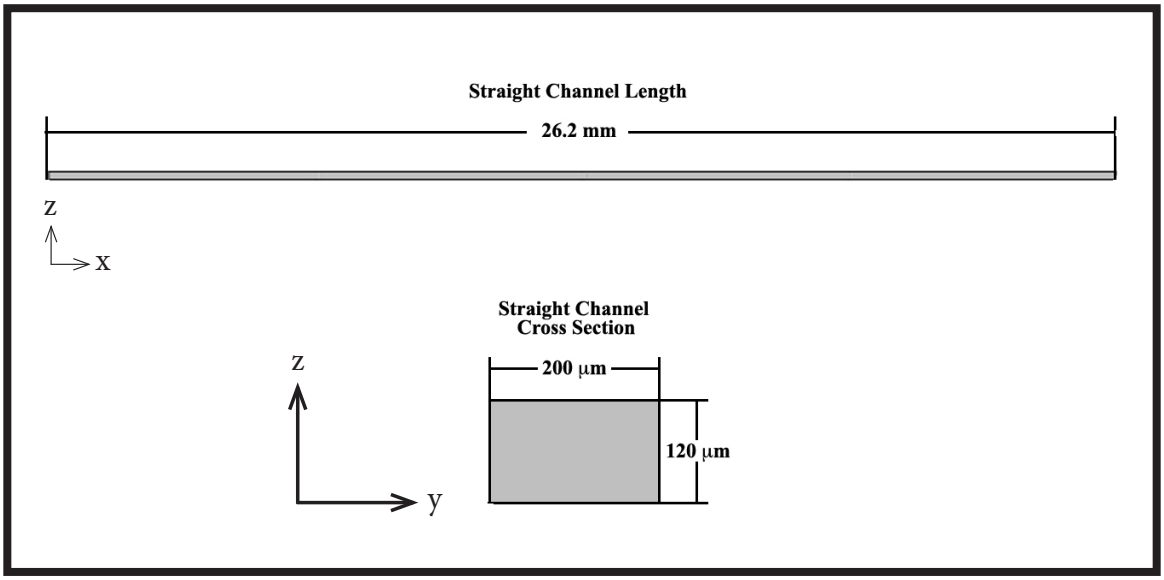

Figure 19: Case 1 - T-mixer geometry.

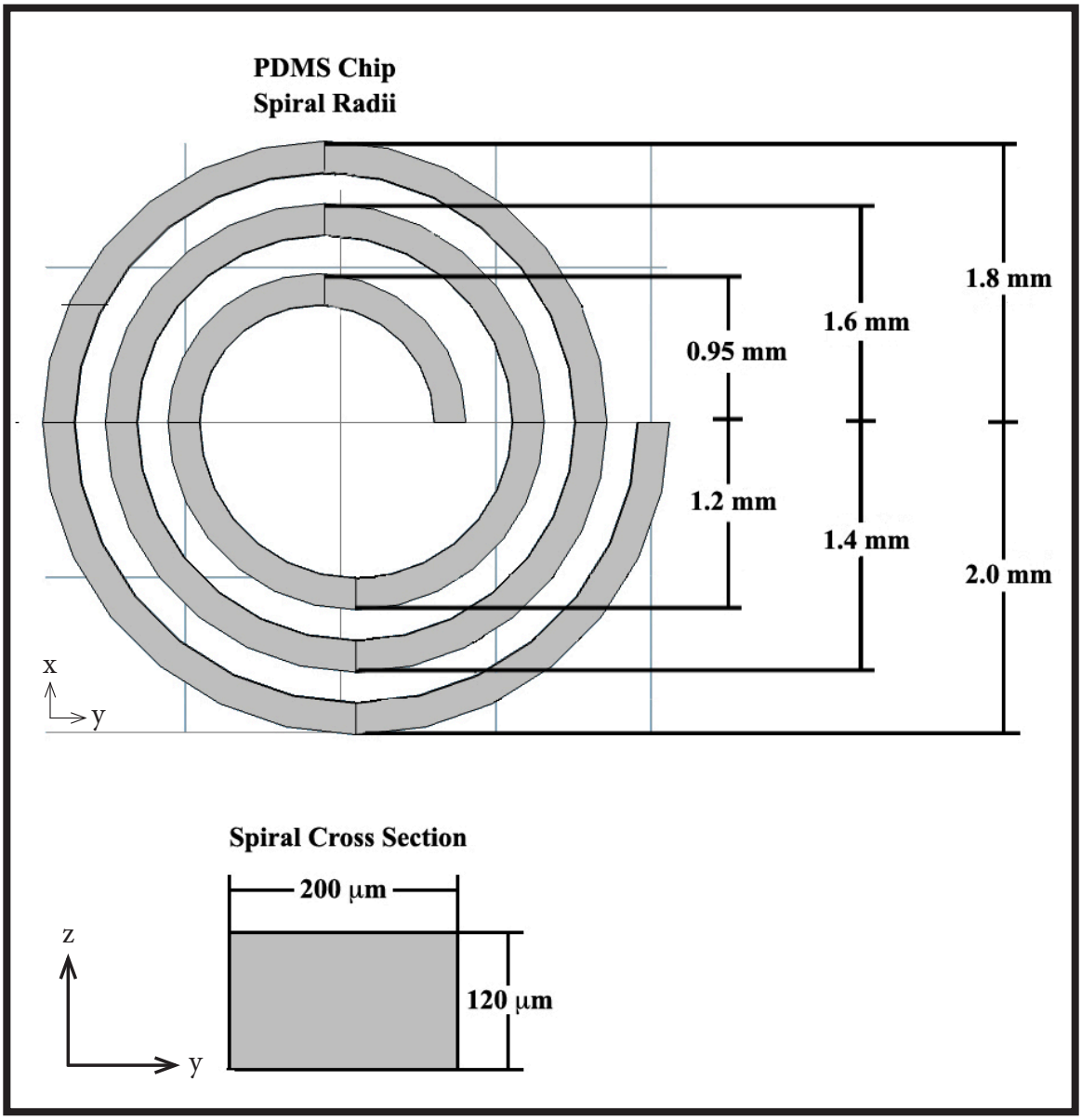

Figure 20: Case 3 - DMI PDMS spiral mixer geometry.

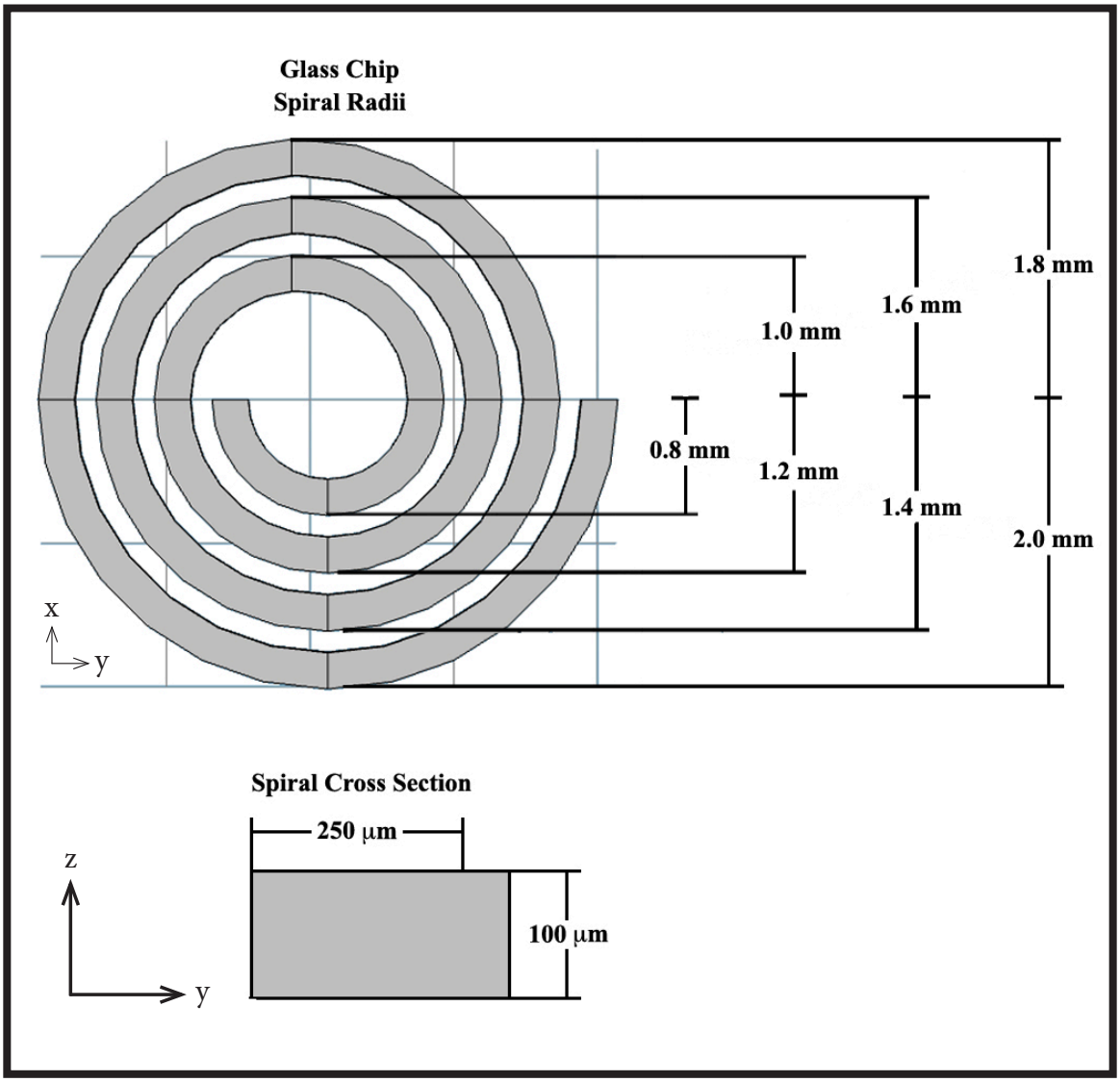

Figure 21: Case 2 - Glass chip spiral geometry.

6.4 COMSOL Implementation

A solution using the COMSOL software is achieved in two steps. First, the velocity field is found from solving the Navier-Stokes equation. The velocity field is then mapped to the convective mass-transport term of the mass transport equation. The Navier-Stokes equation for steady incompressible flow is given by:

$$\rho (\mathbf{u} \cdot \nabla) \mathbf{u} - \mu \nabla^2 \mathbf{u} - \nabla p = 0 \quad (8)$$

$$\nabla \bullet \mathbf{u} = 0 \quad (9)$$

where μ is the viscosity (Pa•s), $\mathbf{u}$ is the velocity (m/s), ρ is fluid density (kg/m^3), p is pressure (Pa). The convection-diffusion equation is:

$$D \nabla^2 c - \mathbf{u} \cdot \nabla c = 0 \quad (10)$$

where D is the diffusion coefficient (m^2/s), and c is the concentration (mol/m^3). Due to instabilities in the solution from the convective term, a finer mesh is needed to obtain a solution for the concentration field than for the velocity field (COMSOL 2011).

As noted in section 2.3, mixing assessment techniques are inconsistent in the literature. In order to compare the model data with the experimental data, a similar calculation was employed. The experimental mixing data was examined by using the same calculation as the experimental method, but calculations relied on the concentration value instead of the pixel intensity value. This is the method was also employed in a study comparing various micromixers (Finlayson, Aditya et al. 2008). The concentration variance, $\sigma_{c,}$ was calculated based on concentration using:

$$\sigma_c = \langle (c - \langle c \rangle)^2 \rangle^{1/2} \quad (11)$$

where *c* is concentration between 0 and 1 and $\langle c \rangle$ is the average concentration across the sampled region.

Dean flow effects were also considered. In order to further investigate the secondary flow effects, the average magnitude of the transverse or secondary flow (U_2) was calculated as well. This was accomplished using the surface integration tool in COMSOL and the

following equation:

$$U_2 = (v^2 + w^2)^{\wedge.5} \tag{12}$$

where v is the velocity magnitude in the y direction and w is the velocity magnitude in the z direction of the x-y-z 3D coordinate system.

6.5 Preliminary Mesh Study (DMI PDMS Spiral Mixer)

Engineering judgment is generally used to decide on the type of element shape used for discretization (Logan 2011). In order to get a feel for which element shapes would be best for this spiral mixer model, a preliminary mesh study was performed. Three different mesh types were analyzed for the PDMS spiral mixer. For each study a coarse grid was used to solve for the velocity field and a refined grid was used to solve for the mass transport. The first mesh was generated using default COMSOL options for generating a physics controlled mesh. This mesh was generated with tetrahedral elements and refined at the wall. The physics controlled coarse mesh had 149,663 elements and the refined mesh had 408,781 elements. The other two meshes investigated were generated with user-controlled meshing options. For both meshes, the initial mesh element was generated on the top surface of the spiral, and then the COMSOL sweep option was used to sweep the mesh through the geometry with a given distribution. The second mesh studied resulted from an initial triangular mesh on the surface that was swept through the geometry. This coarse triangular swept mesh had 175,680 elements and the refined mesh had 497,040 elements. The last mesh considered was generated with an initial quadrilateral mesh on the surface that was then swept through the geometry with a given distribution. The coarse quad swept mesh had 104,958 elements and the refined mesh had 626,483 elements.

The three meshes and a resulting surface concentration plot near the entry region of the spiral for each case are summarized in Figure 22. After a superficial inspection of the results, the quad swept mesh was chosen for a further grid study. The inlet was defined

to have distinct two fluids flowing in parallel to each other. One fluid has a concentration of 0 and the other 1. Only the quad grid appeared to resolve this gradient well in the inlet region. It was decided that a quad grid would be the best option for resolving the velocity and concentration gradients for this problem.

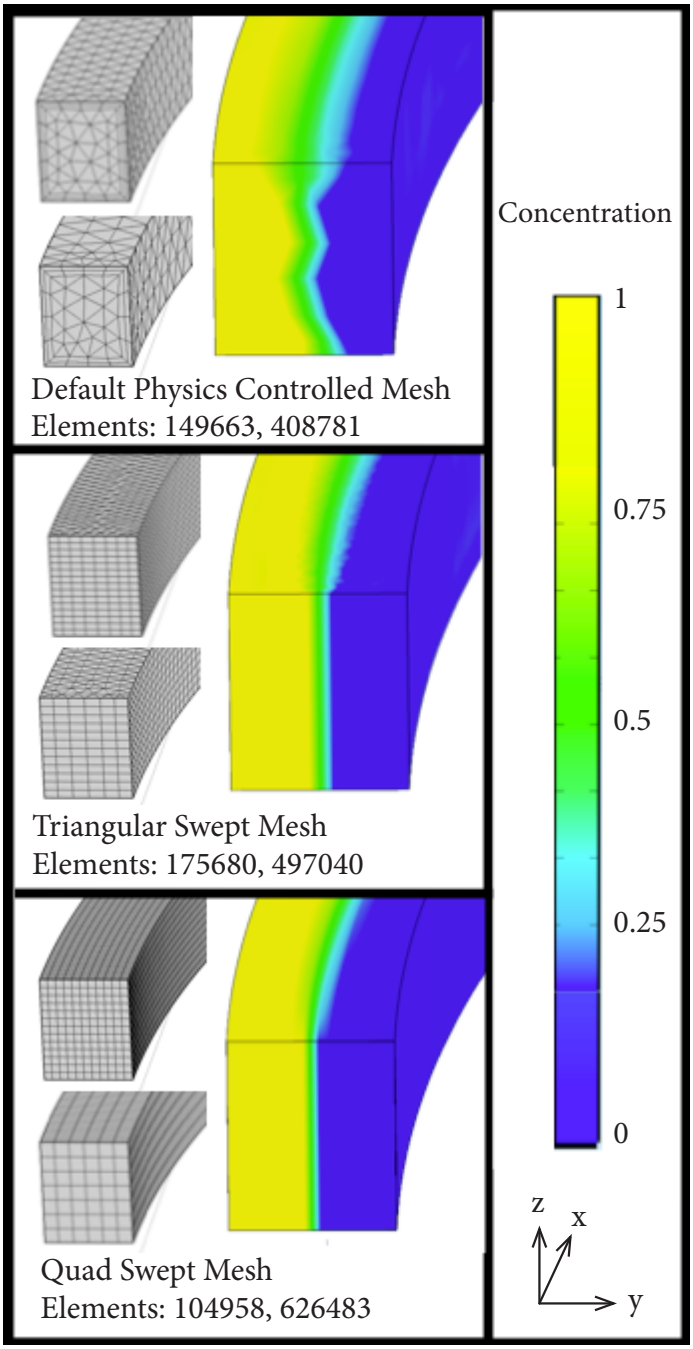

Figure 22: Preliminary grid study summary for DMI PDMS spiral mixer.

6.6 Mesh Independence Study (DMI PDMS Spiral Mixer)

The quad swept mesh was studied further to ensure an appropriate mesh size was used to provide results that were independent of mesh size, but not overly refined to reduce computational time. An analysis was performed initially for the mesh used to resolve the velocity. As noted earlier in this chapter, a finer grid is required to solve for the concentration field than for the velocity field. Therefore, after the mesh was chosen for the velocity field, a similar study was performed to select a mesh to resolve the concentration field.

For the velocity field study, five different mesh refinements were examined. The meshes were ranged from the coarsest, with 6,720 elements, to the finest, with 134,656 elements. An overview of the five meshes is presented in Figure 23.

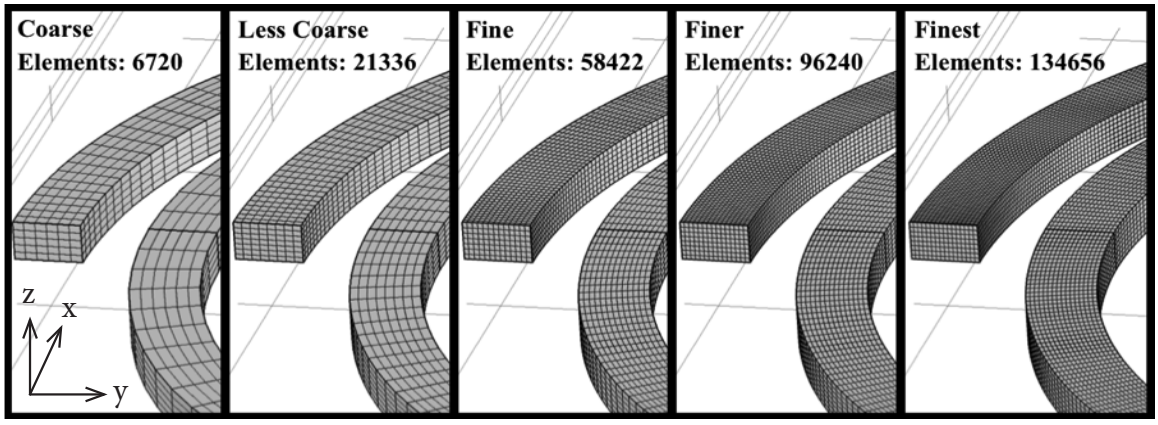

Figure 23: Summary of meshes examined for the velocity field independence study.

In order to evaluate the meshes for solution independence, the velocity profiles at a line, in the xy-plane, cut at half the height of the channel, were examined. This line where the data was taken can be seen in Figure 24. The velocity plot across the entire spiral is presented in Figure 26. An extreme zoom of one of the peaks from that plot is shown in Figure 25. The minimal difference between the finer and finest plots indicates that the data resulting from the finer plot is independent of mesh size.

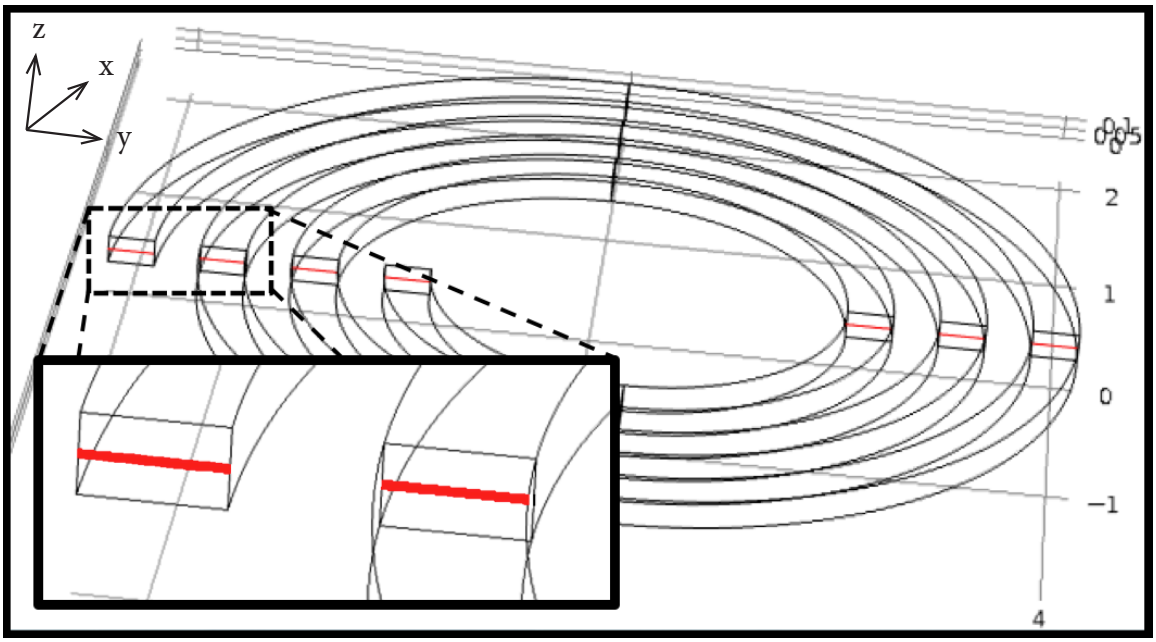

Figure 24: Red line showing location of velocity data used for mesh independence study. Inset image shows close up of red line at the inlet and first spiral.

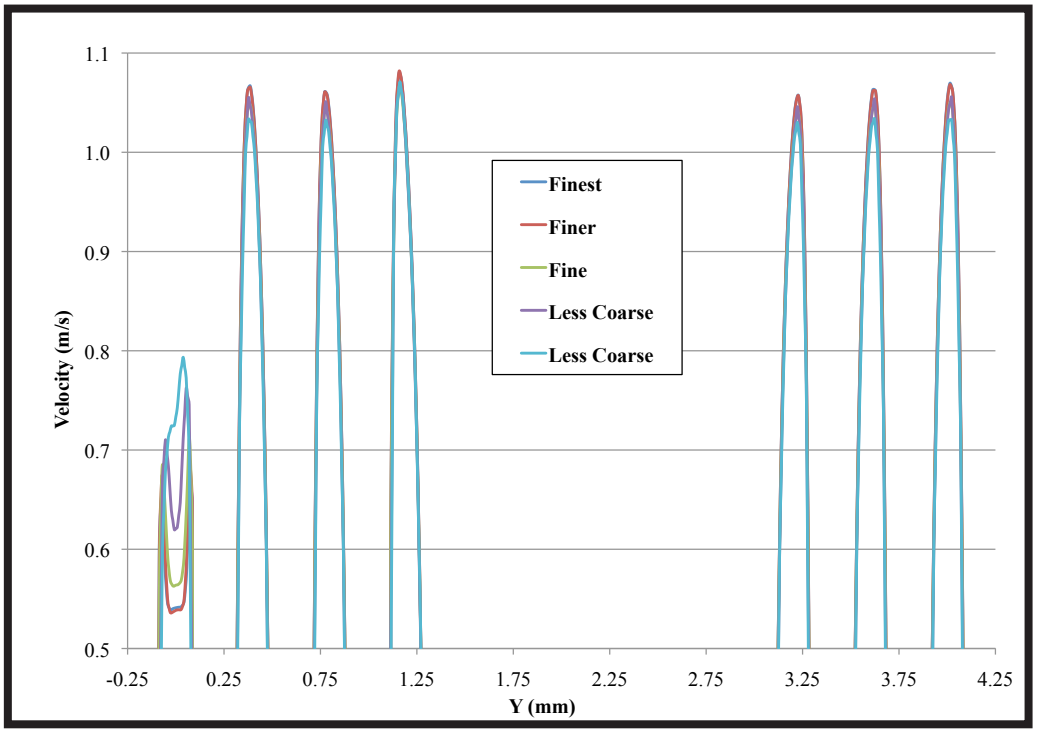

Figure 25: Velocity profiles for grid independence study.

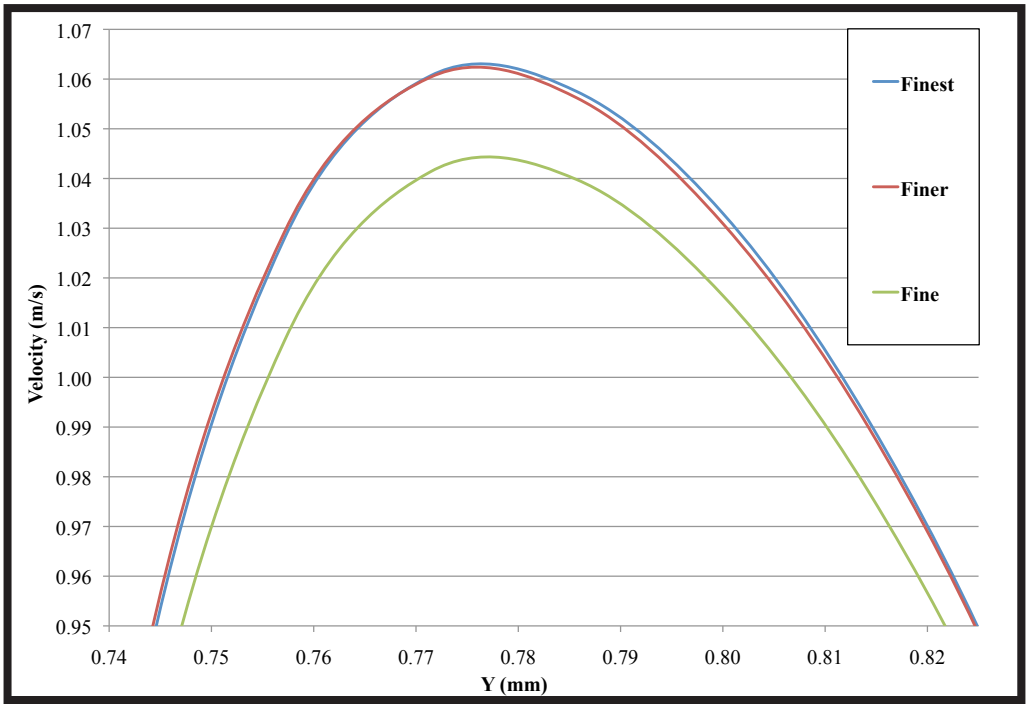

Figure 26: Zoom of the second peak from the grid independence study for the velocity. There is minimal difference between the finer and finest grid.

To ensure that the concentration results were also independent of grid size, a similar study was performed. This study also addresses the issue of numerical diffusion. Although it is impossible to perform a computational study without introducing some degree of numerical diffusion, the numerical diffusion needs to be much lower than the physical diffusion. One method to reduce the numerical diffusion is to refine the grid. As such, this study is done for gird independence as well as to minimize numerical diffusion. For this study, the finer velocity field mesh (96,240) from the velocity field study was used and then three further refined grids were tested for the second analysis step. The σ_c value at the outlets was used for comparison as well as inspection of the concentration profiles along the same cut-line of data used for the velocity field grid independence study. The concentration field profiles along the cutline are shown in (location for data can be seen in Figure 24) The σ_c outlet study is summarized in Figure 29. The percent difference between concentration variance for the fine and finer grid was 46%. The percent difference between the finer and finest grid was 3%. The finer grid, which had 282,520 elements was selected for the concentration field.

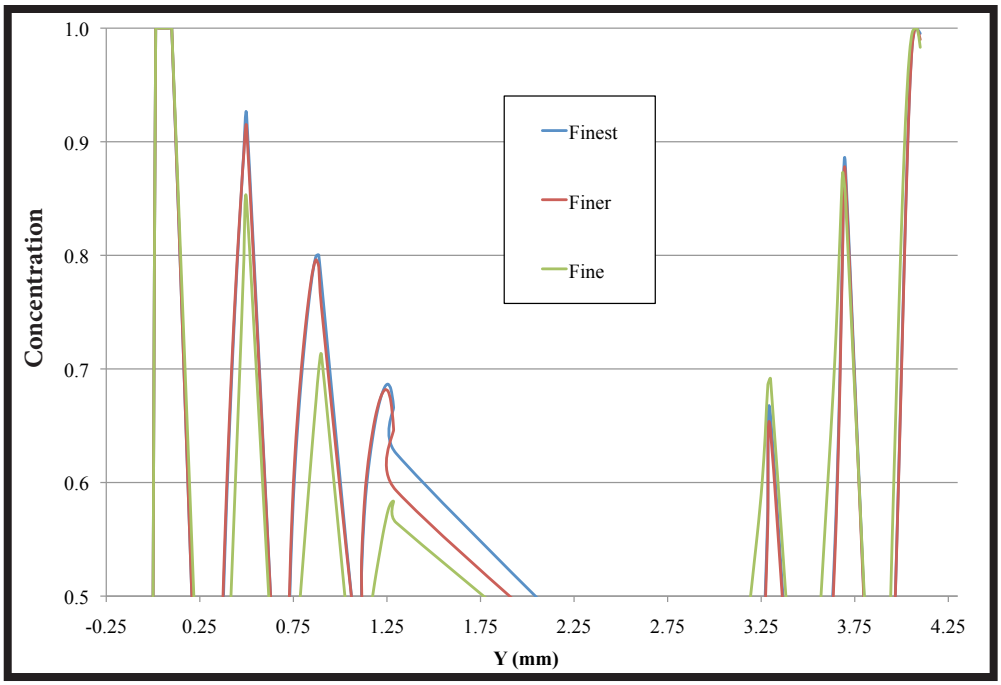

Figure 27: Concentration profiles for grid independence study.

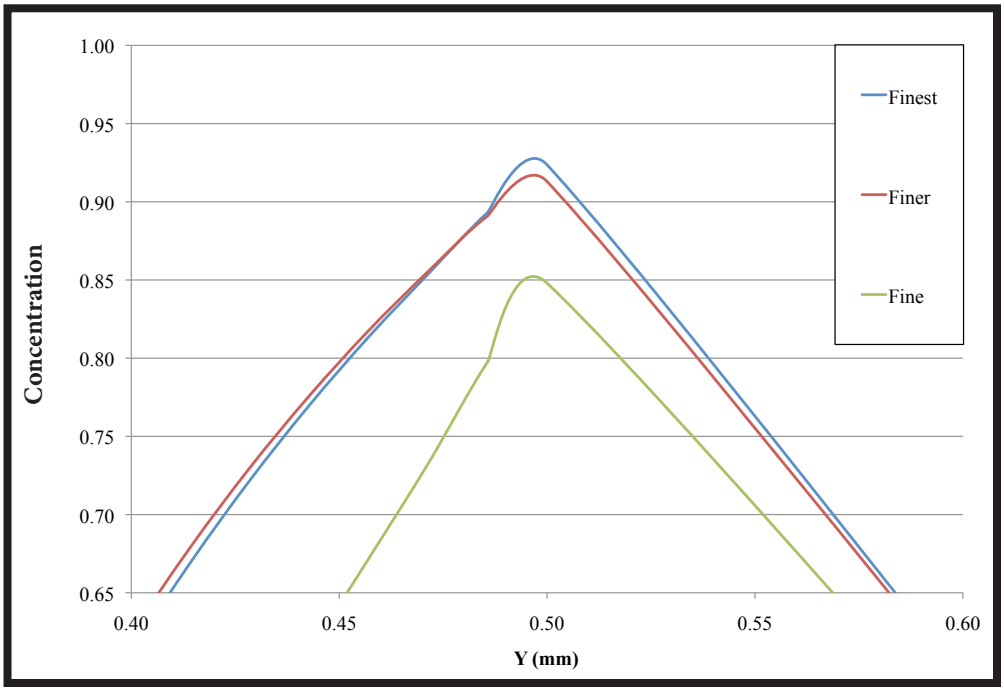

Figure 28: Zoom view of second peak from concentration grid independence study for concentration. There is minimal difference between the finer and finest grids.

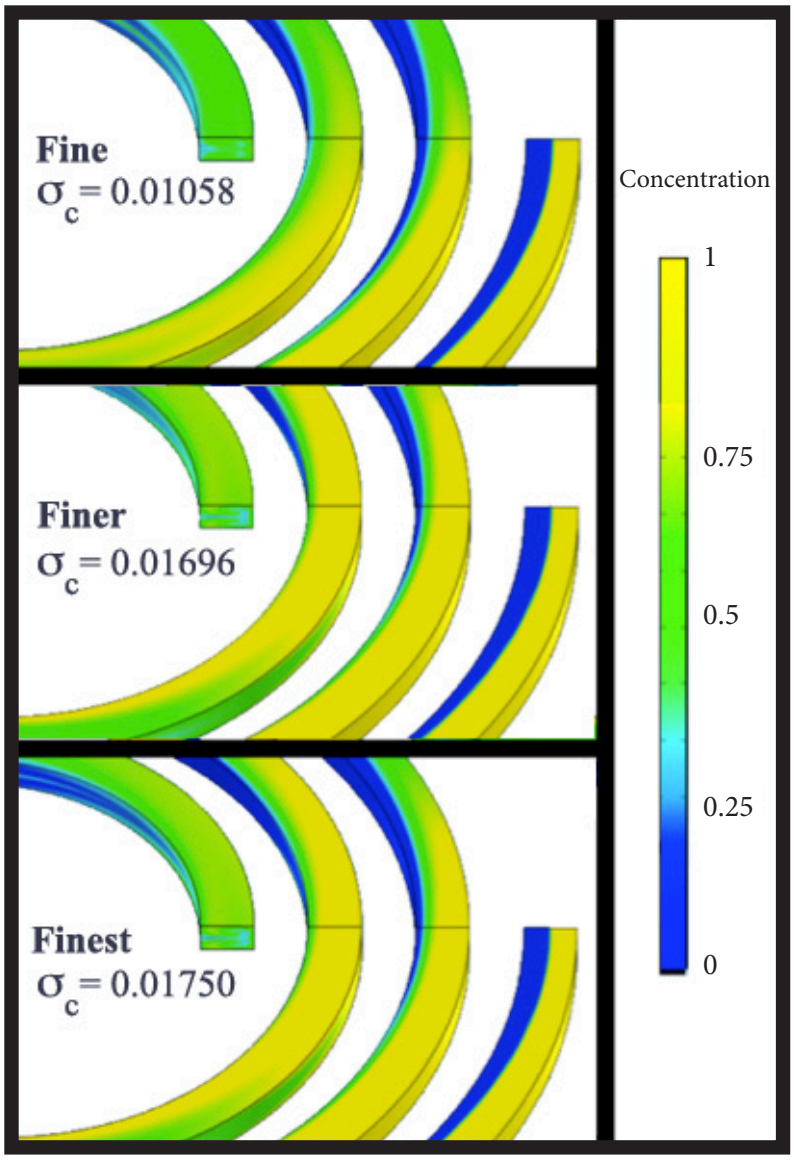

Figure 29: Grid independence study concentration values at outlet.

Although for both studies, the three finest grids were referred to as 'fine, finer, and finest', the 'fine, finer, and finest' grids for the concentration study are more refined than those for the velocity field study. Ultimately, the finer grid from the velocity field study was used as the primary grid for solving the Navier-Stoke equation. This grid had 96,240 elements. The finer grid from the concentration field study was used as the secondary grid for solving the transport equation. This grid had 282,520 elements. This is summarized in Figure 30.

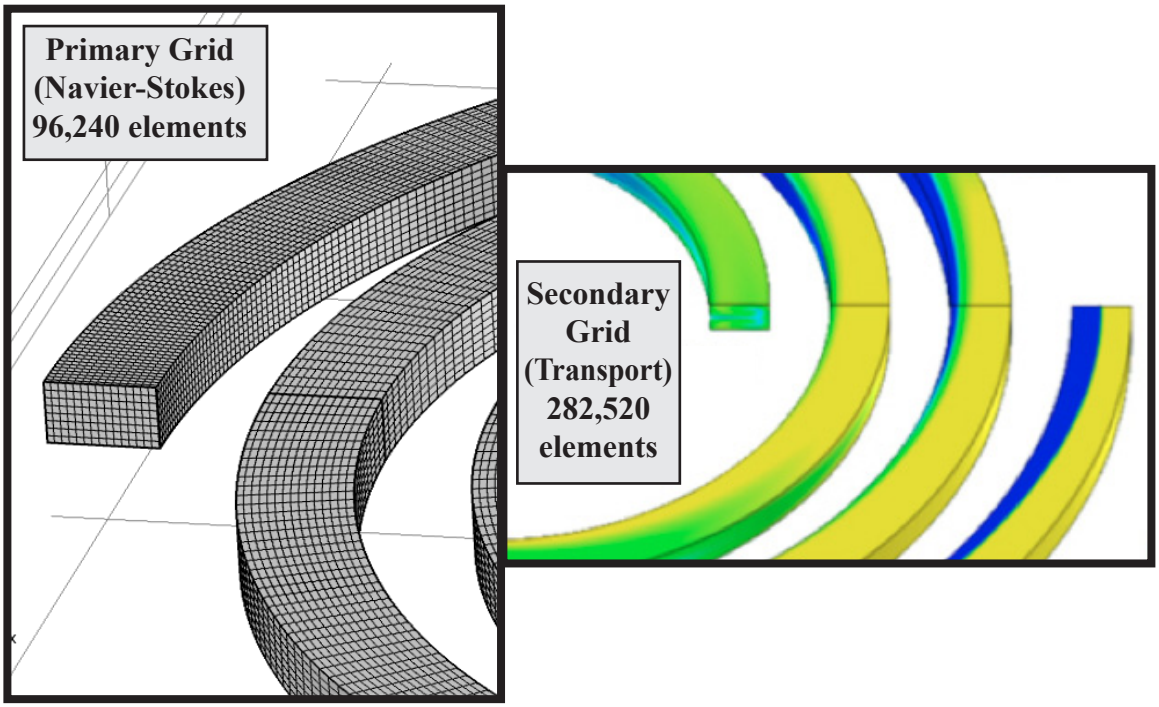

Figure 30: Primary (Velocity field) and secondary (concentration field) grid summary.

6.7 Analysis Summary

As noted in the parameters section, three different cases were run. For case 1, the straight channel, concentration measurements were made at the inlet and at locations at each quarter length along the pathway and the outlet (shown in Figure 31). For case 2, the glass spiral chip, pressure measurements were obtained at the inlet and outlet (Figure 32). For case 3, in order to yield data that is similar to the experimental DMI PDMS spiral mixing data, five locations were selected in a similar manner to the experimental location selections. These locations can be seen in Figure 33. The computational model was simplified over the physical geometry. As can be seen in Figure 33, the two inlet channels and plenum were not modeled, nor was the tube exiting the spiral and feeding into the exit/detection channel. This was part of the problem simplification process to reduce the size of the problem to lessen computing resource needs. The inlet and outlet locations are therefore different in the model than the experimental system. They are however similar and still provide useful information. In order to see the difference from an analysis of the cross sectional area and a view from the top of the channel in the model, a line segment at the top of the cross section was also analyzed. This is shown in Figure 34. COMSOL was then used to solve for five different inlet velocities (specified in Table 1) for all three cases. Data for the concentration fields were only calculated for case 1 and 3, as case 2 was analyzed for pressure drop only.

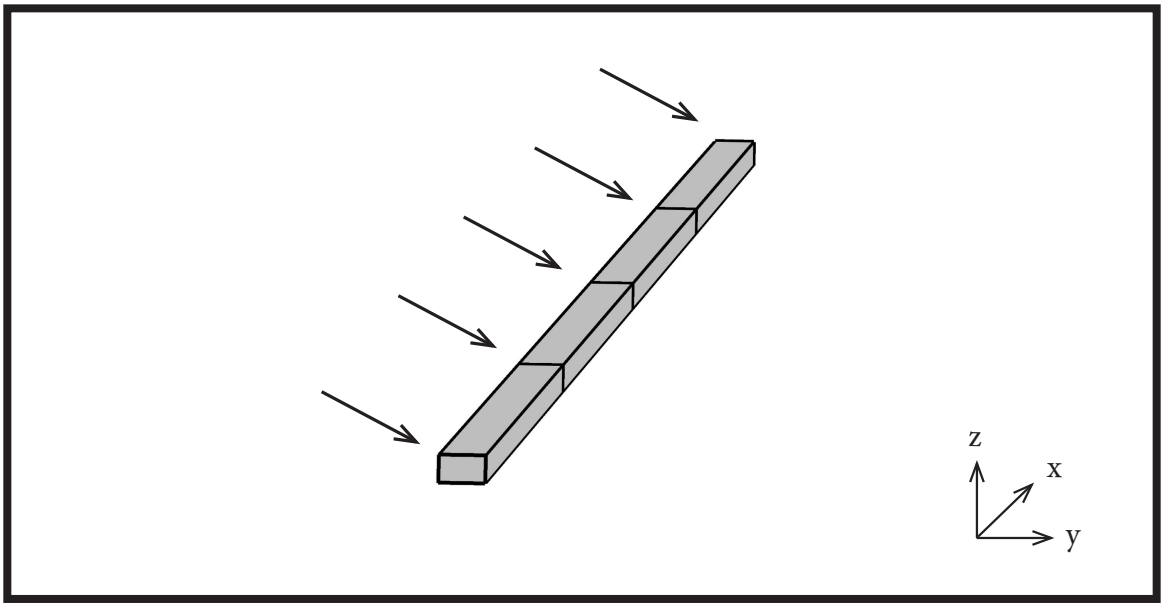

Figure 31: Straight channel (case 1) data analysis locations.

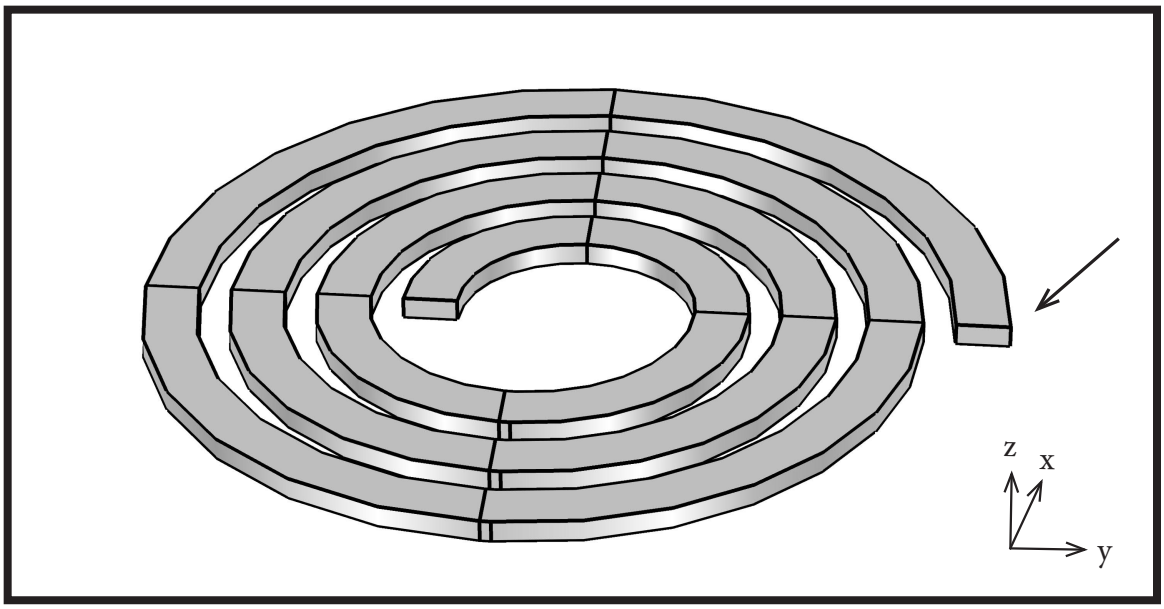

Figure 32: Glass spiral mixer chip (case 2) data analysis locations.

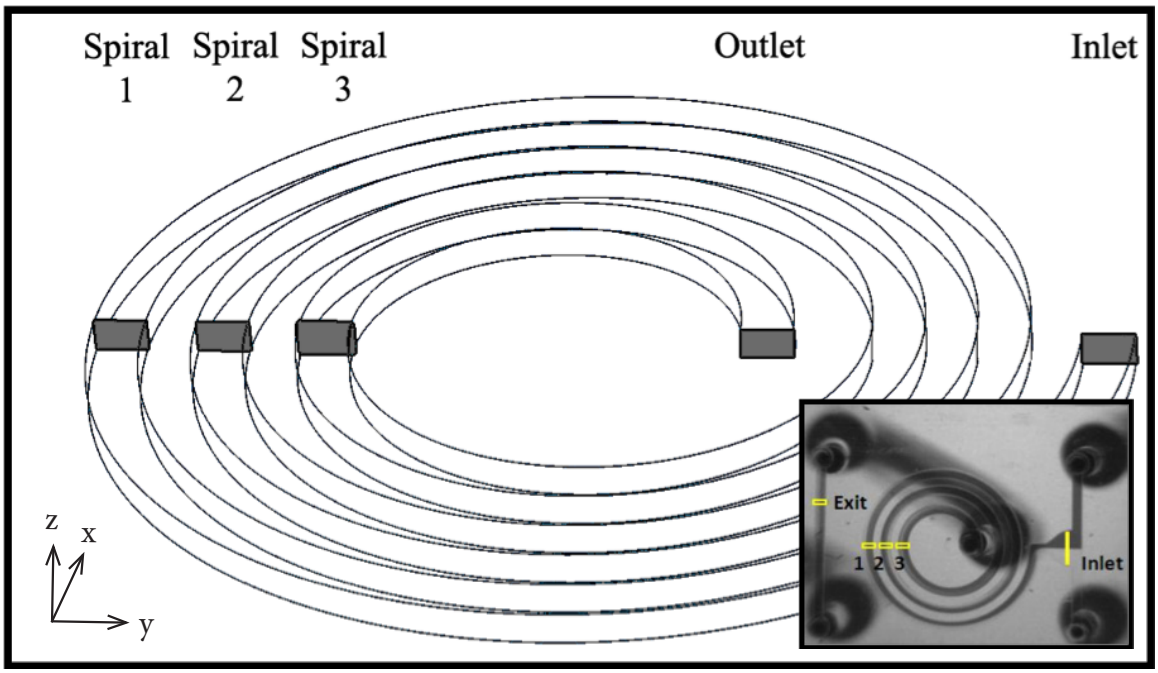

Figure 33: Locations were cross sectional data was taken for case 3 (DMI's PDMS spiral mixer).

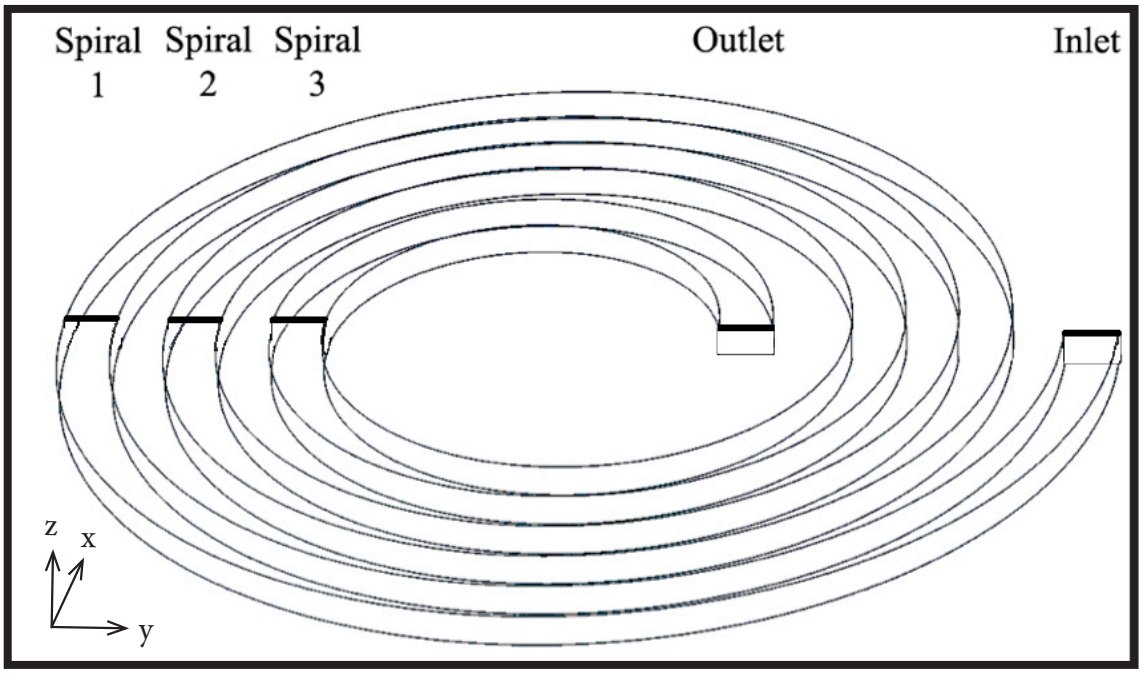

Figure 34: Lines show region where data was take for a top view analysis for case 3 (DMI's PDMS spiral mixer).

CHAPTER VII

RESULTS

7.1 Case 1 - Straight Channel Data

As described in the previous chapter, σ_c values were calculated for a straight channel. This was performed to gain confidence in the model behavior. The results from the T-mixer study are in shown in Figure 35-39. Each figure shows a 3D image of a concentration surface plot, as well as a plot of distance along the mixing path versus σ_c for five locations equidistance along the fluid path.

In Figure 35, the lowest Re case run, the concentration surface plots shows that there is diffusion between the two fluids. At the outlet, the diffusive interface is approximately half of the channel surface. The plot of Re versus σ_c shows that mixing increases along the channel length. This trend is not linear due to the developing flow at the entry region. At the outlet σ_c is below 0.1.

In Figure 36, where Re = 12, the concentration surface plots also show that there is diffusion between the two fluids. At the outlet, the diffusive interface is approximately have the size of surface area from the previous case, Re = 8. There is therefore less mixing at Re = 12 than Re = 8. This is also evident from the plot of Re versus σ_c. The value for σ_c is between 0.1 and 0.2, whereas for Re = 8 it was below 0.1. The trend appears to be linear after the second data point, indicating that the flow is fully developed.

In Figure 37, where Re = 30, the surface plot shows even less mixing than the previous case at the outlet. This is also apparent the plot of Re versus σ_c. The value for σ_c at the outlet is approximately 0.3 which is higher than the previous case. This again indicates less mixing than the previous case.

In Figure 38, where Re = 60, the surface plot shows minimal mixing. The value for σ_c at the outlet is between 0.3 and 0.4. The trend of less mixing as Re increases is evident as at the outlet for the previous case σ_c was approximately 0.3.

In Figure 39, Re = 90, the surface plot again shows minimal mixing. The value for σ_c at the outlet is approximately 0.4. There is slightly less mixing than the previous case.

In summary, For Re = 8, the σ_c value was below 0.1 at the channel outlet. For Re = 12, the σ_c value was between 0.1 and 0.2. For Re = 30 the σ_c value was approximately 0.3. For Re = 60, the σ_c value was between 0.3 and 0.4. For Re = 90, σ_c was approximately 0.4. The mixing increases along the length of the channel for each case, but from case to case mixing decreases with an increase in Re. The flow generally appears to be fully developed near a quarter of the length of the channel for all cases leading to a linear increase in mixing along the length of the channels after that point.

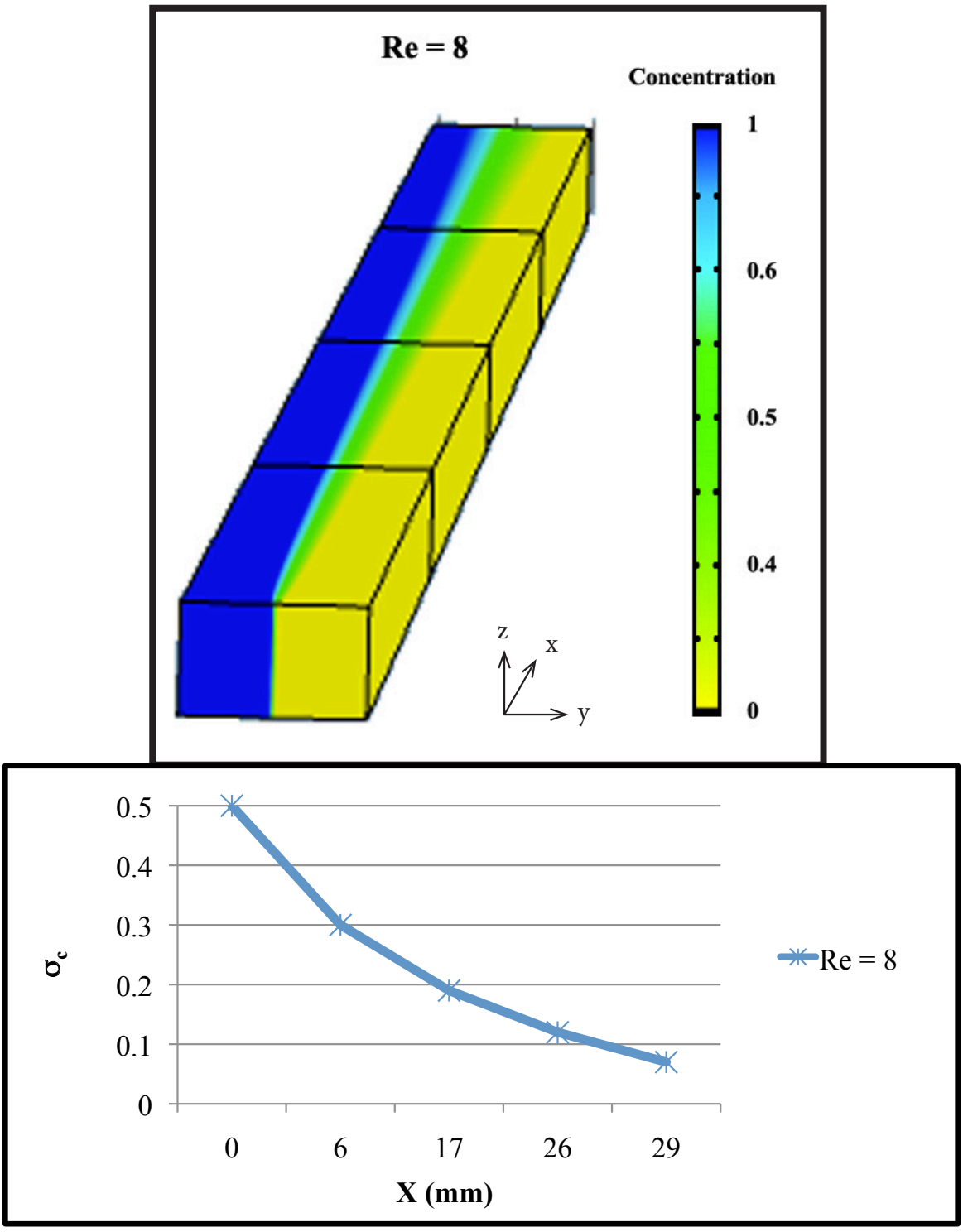

Figure 35: T-mixer concentration data for Re = 8.

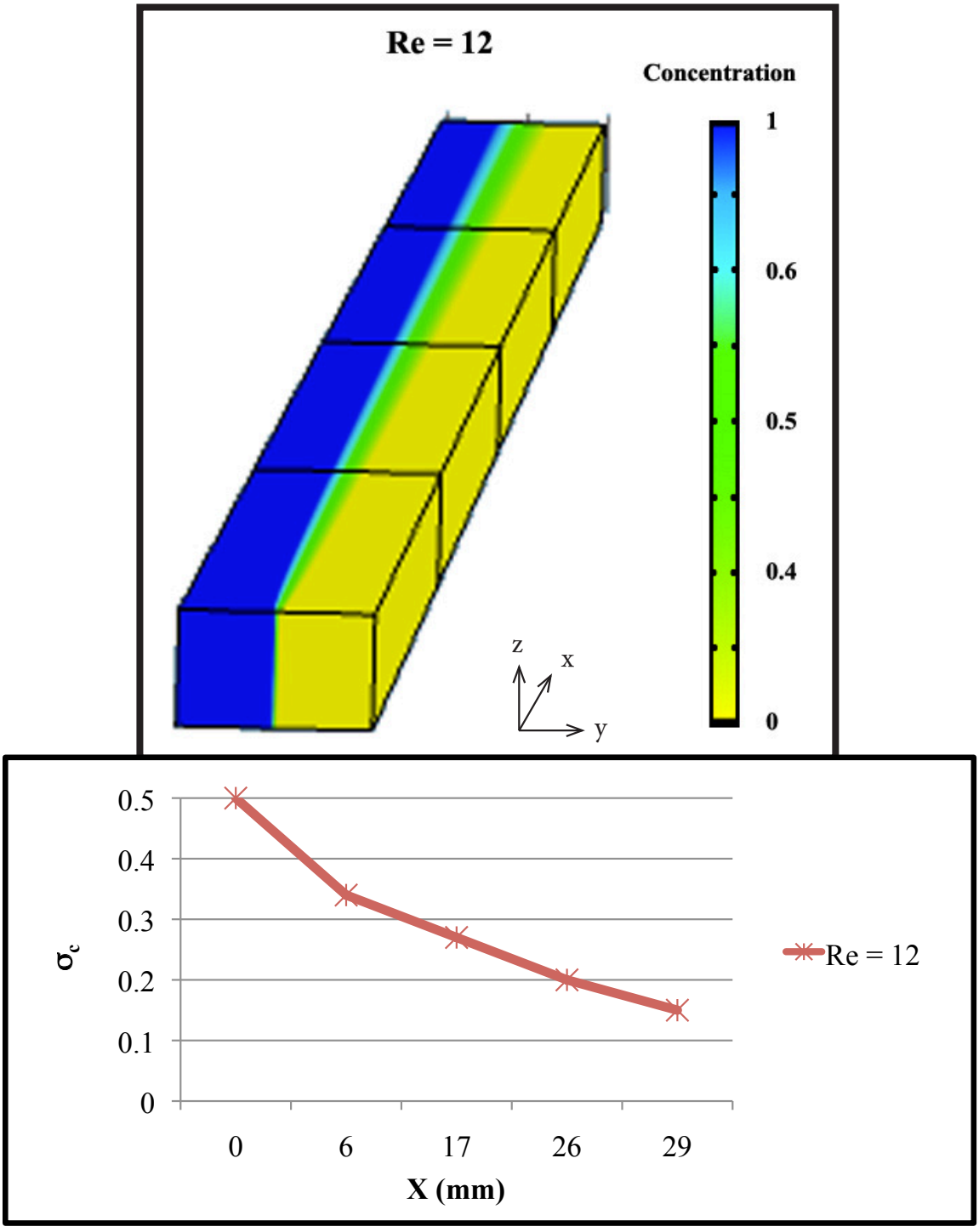

Figure 36: T-mixer concentration data for Re = 12.

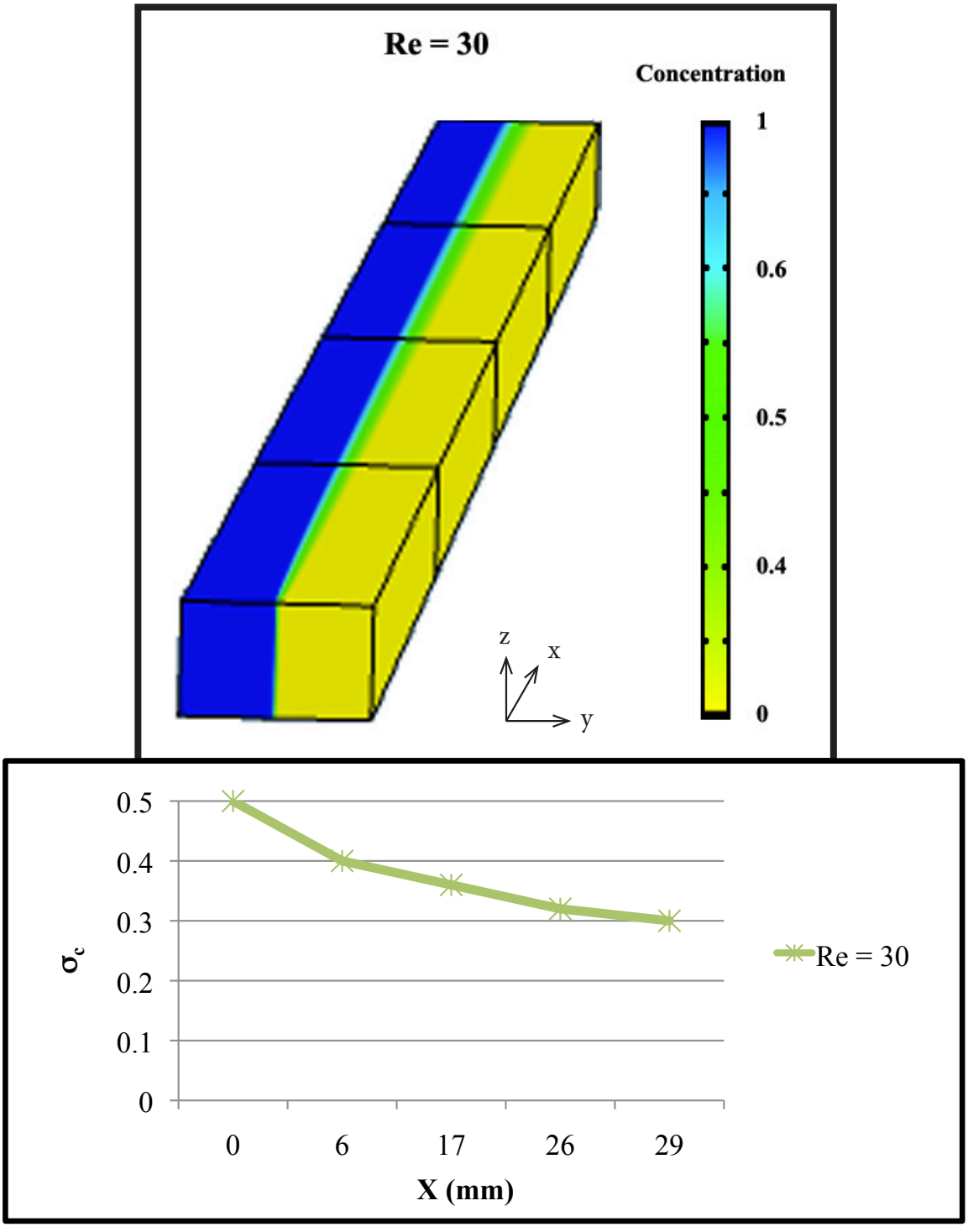

Figure 37: T-mixer concentration data for Re = 30.

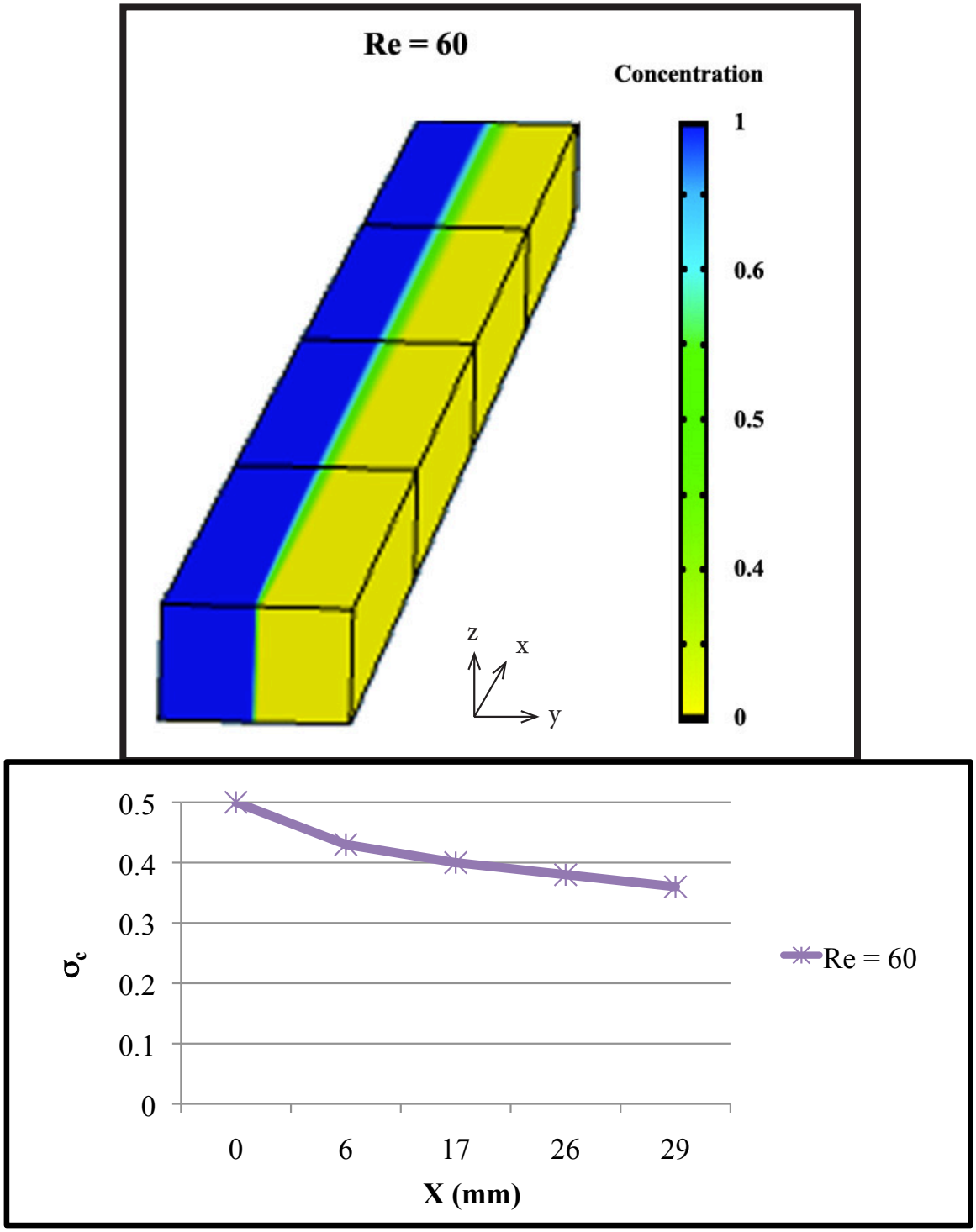

Figure 38: T-mixer concentration data for Re = 60.

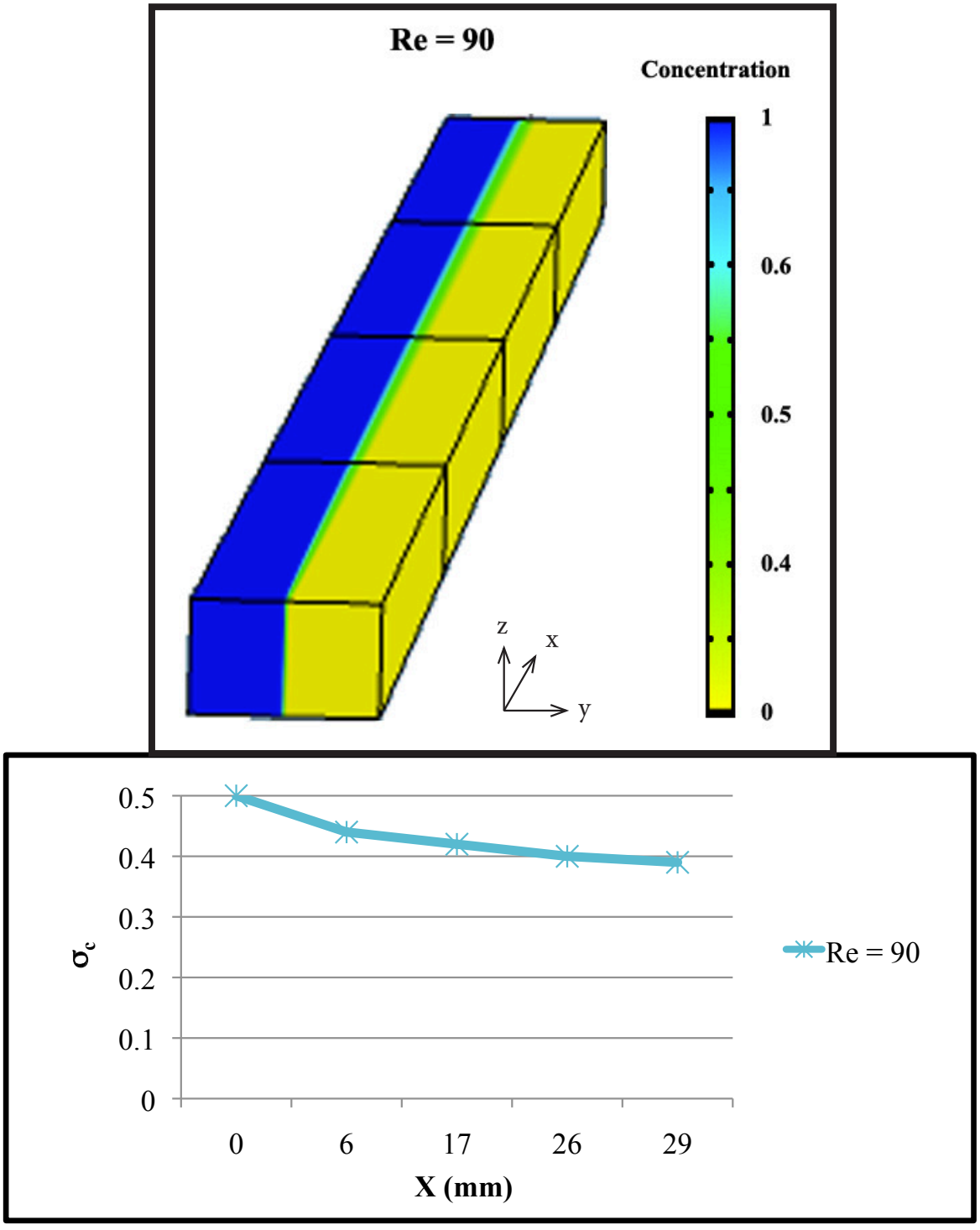

Figure 39: T-mixer concentration data for Re = 90.

7.2 Case 2 - GRC Glass Chip Model Data

From the glass chip experimental study at GRC, it was shown that there is extremely close correlations between the experimental pressure drop data and the theoretical pressure drop data. In order to assess how close the model data is to the theoretical and experimental data, pressure values were examined for a model of the glass chip as well. The correlation between the model data and the theoretical pressure drop is shown in Figure 40. It should be noted that the theoretical pressure drop in this plot differs from the experimental theoretical pressure drop shown previously (Figure 11). This is due to the fact that the previous theoretical calculation including the restrictions from the tubing as well as the inlet region which was not modeled. In the numerical model, the inlet concentrations were set as a boundary condition. The exit boundary condition was P = 0. The theoretical pressure drop plotted in Figure 40 only took into account the length of the spiral.

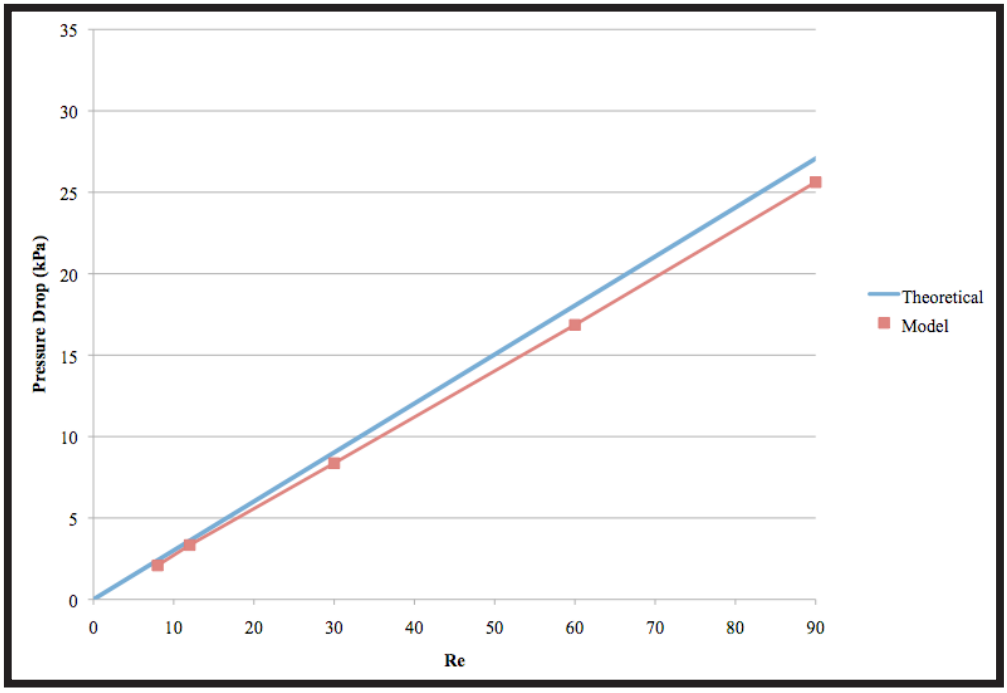

Figure 40: Theoretical and model Re versus pressure drop plot for glass chip.

7.3 Case 3 - DMI PDMS Spiral Mixer Model Data

For the DMI PDMS spiral mixer model, as described in the previous chapter, σ_c values for cross sectional areas were calculated in similar regions to the experimental data. Recall that the inlet concentration was specified as a boundary condition: over the inlet cross-section, the concentration was represented as two-equal area regions with c = 0 and 1, respectively. This translates into an inlet value of $\sigma_c = 0.5$, a fully unmixed condition. The analysis was then repeated at the same locations, but instead of using the whole cross sectional area for analysis, only a line, representing a top view perspective was analyzed. Figure 41 though Figure 55 show the result for all of the cases (Re = 8, 12, 30, 60, and 90). For each data set there is a figure showing a concentration surface plot of the cross sectional areas were data was obtained as well as a visualization of the region for the top view analysis where a line of data was analyzed. There is also a plot of mixing path length versus σ_c. Finally there is a plot of De versus the transverse flow magnitude for each data set.

Figure 41 shows concentration surfaces plots of cross sections for Re = 8 at each quarter turn from the inlet to the outlet. The regions (inlet, spiral1, spiral 2, and spiral 3) where σ_c values were calculated are outlined in a bold black box. In order to visualize what the data for a line from the top view would look like, a very small region from the top of the cross section was taken and expanded. This represents the data taken at a line across the top of the channel. Even at the lowest flow rate, Re = 8, the surface plots appear different than the cross sectional plots. There is a slight distortion in the fluid interface below the surface of the channel that is not visible from a strictly top view. In Figure 42, arc length versus σ_c, the values for the two analyses appear to be in good agreement even though the surface plots are not identical. In Figure 43, the magnitude of transverse flow is 0 for Re = 8 and the De value is less than 2 at all locations along the spiral.

Figure 44 shows the concentration surface plots for Re = 12. From the cross sectional

plots, it is apparent that the interface between the two flows becomes increasingly distorted. At the end of the spiral, it appears that the outer flow has completely folded in half over the inner flow. This effect increases mixing over the previous case, as there is more surface area for diffusion to occur. Figure 45 shows that the σ_c value appears to still correlate fairly well between the cross section and surface line data. Figure 46 shows a plot of De versus the magnitude of transverse flow. The De number ranges from 2-3 along the length of the spiral and for this case a small transverse flow is observed.

The cases for Re = 30 through Re = 90 are similarly presented in Figure 47-55. The trend of distortion between the interface of the two fluids increases with Re. At these higher Re values, the correlation between the surface line to cross-section values becomes worse as Re increases and the interface between the two fluids becomes more distorted and extended. De increases along the channel in each spiral as the radius of curvature increases. The average magnitude of transverse flow also increases with increasing Dean flow.

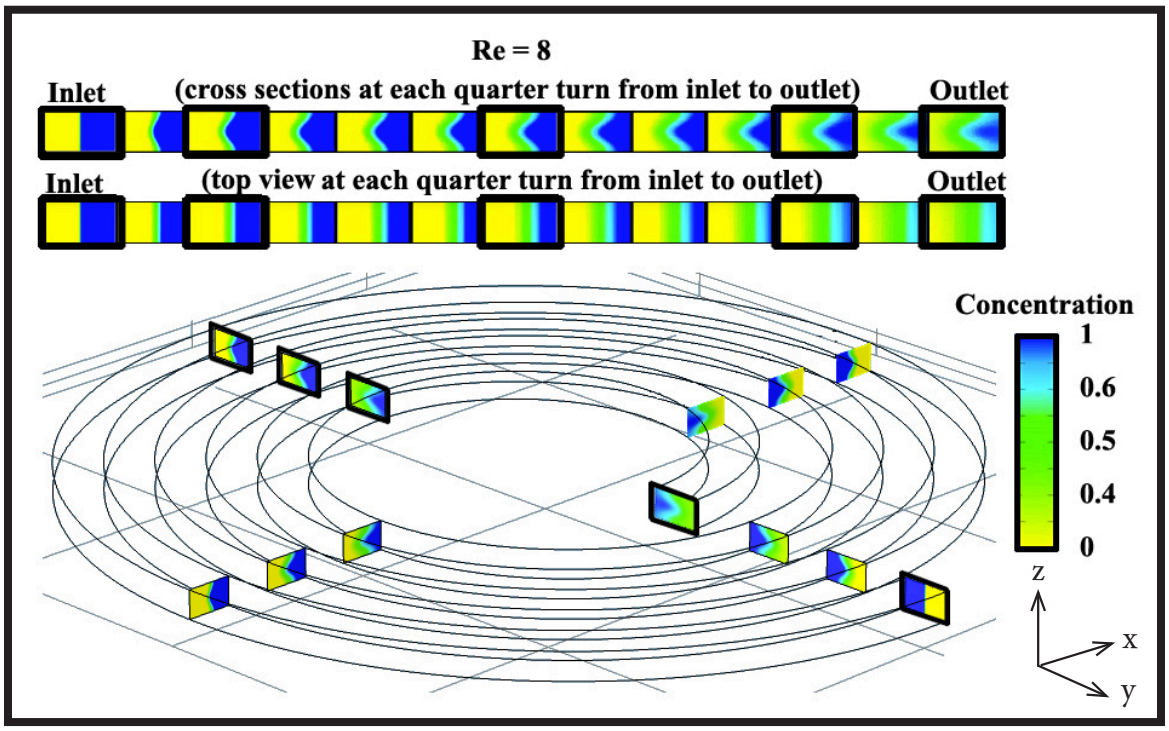

Figure 41: PDMS spiral mixer model concentration surface plots and visualization of line data for Re = 8.

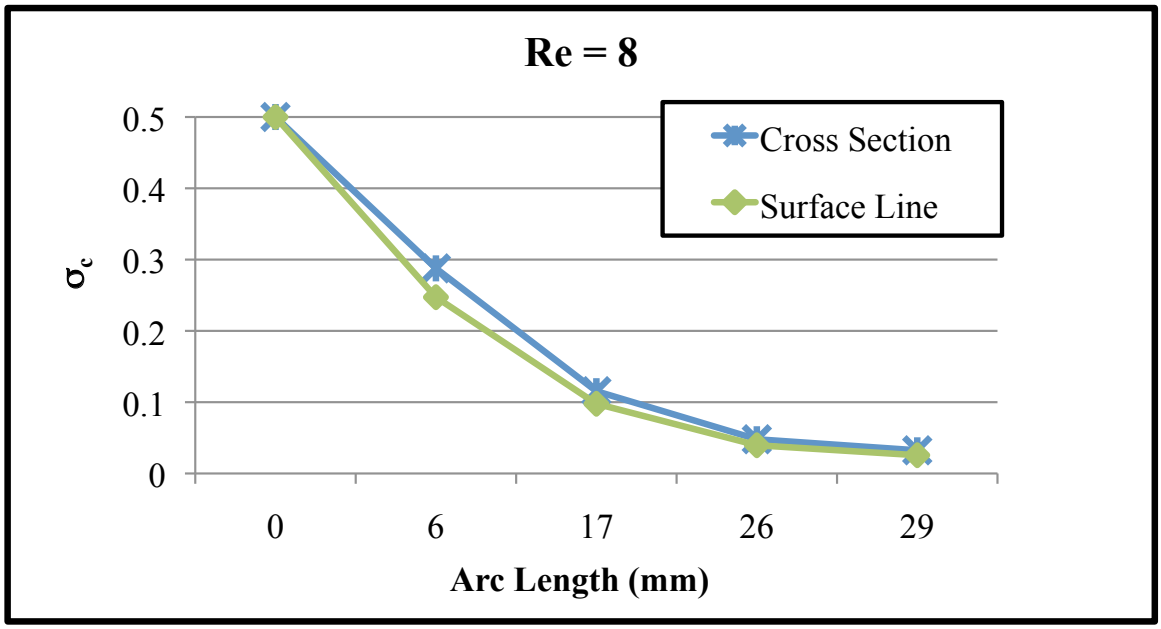

Figure 42: DMI PDMS spiral mixer model plots of concentration along the mixing path length for Re = 8.

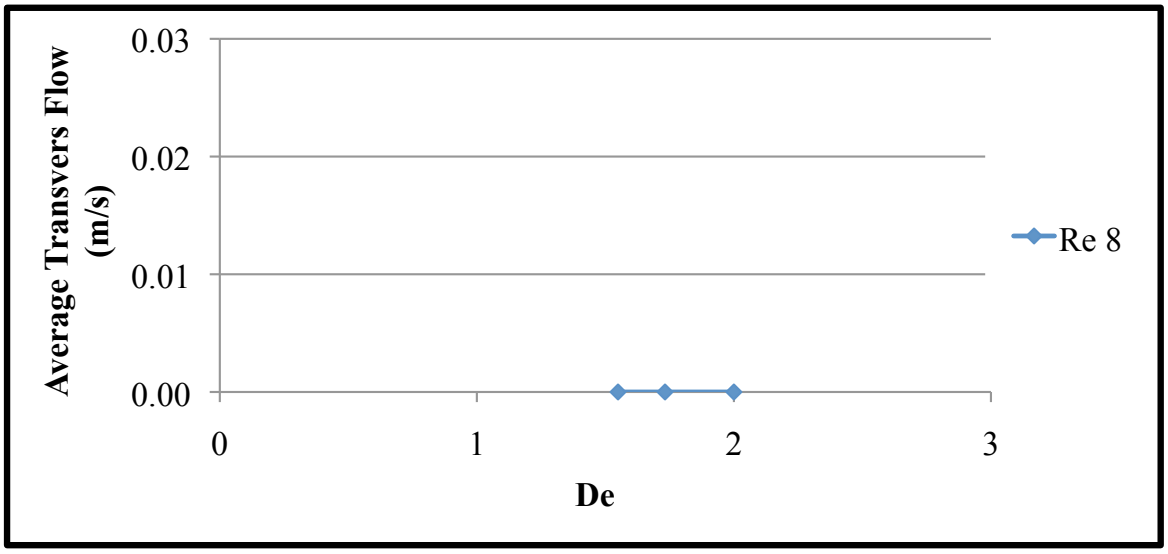

Figure 43: Plot of De versus transverse flow for Re = 8.

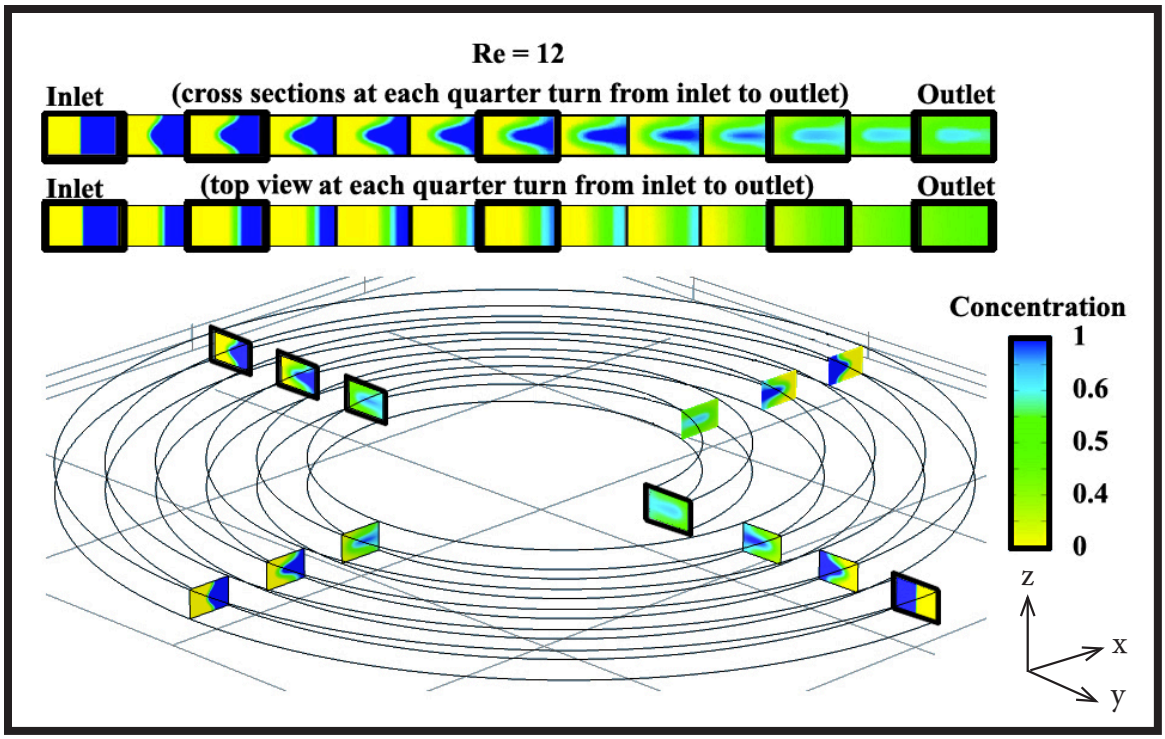

Figure 44: PDMS spiral mixer model concentration surface plots and visualization of line data for Re = 12

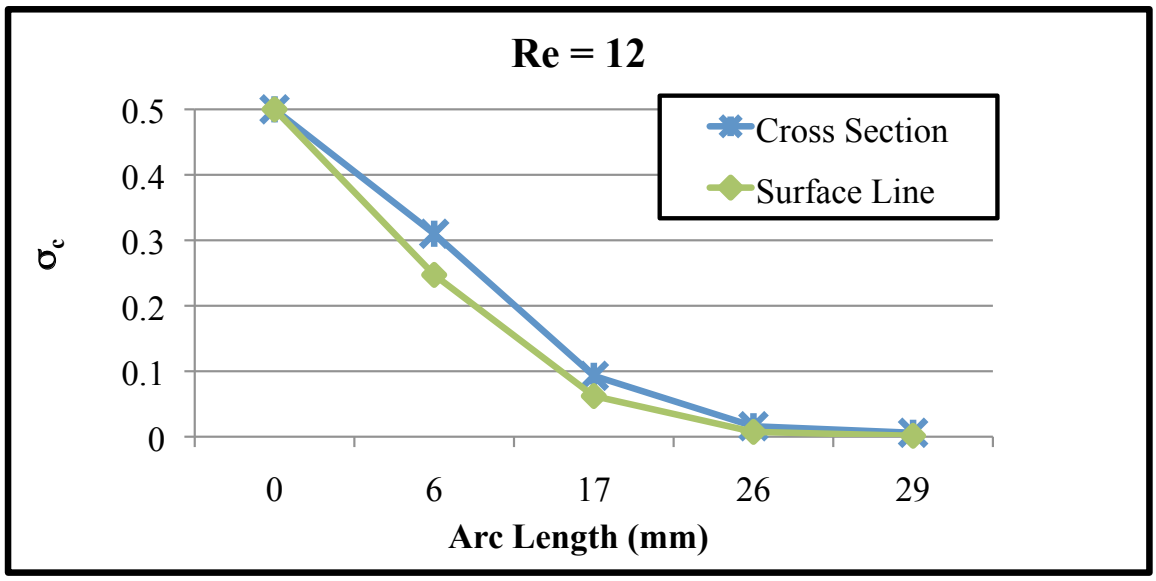

Figure 45: DMI PDMS spiral mixer model plots of concentration along the mixing path length for Re = 12.

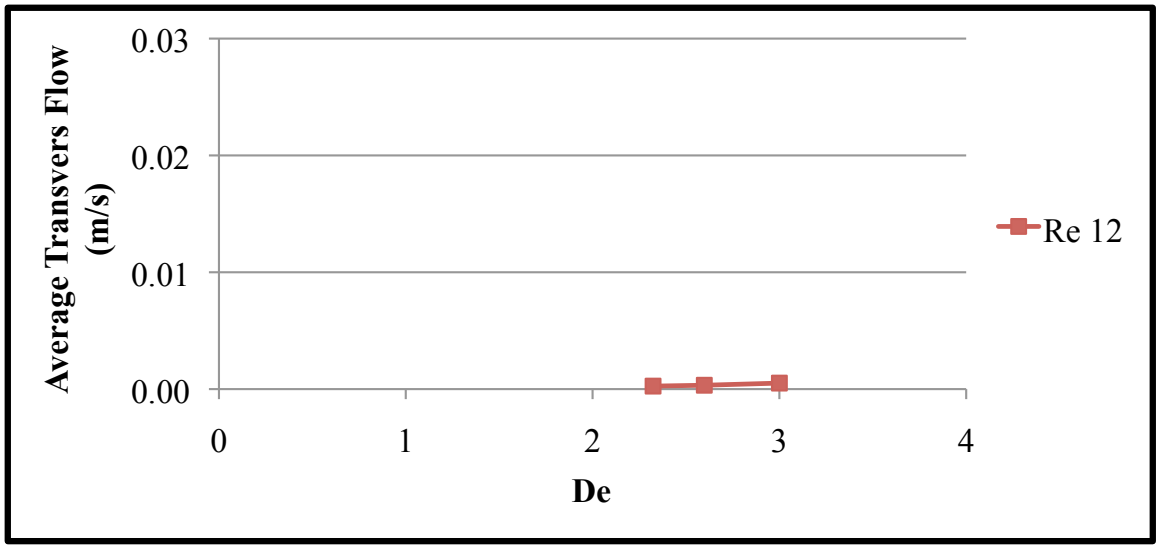

Figure 46: Plot of De versus transverse flow for Re = 12.

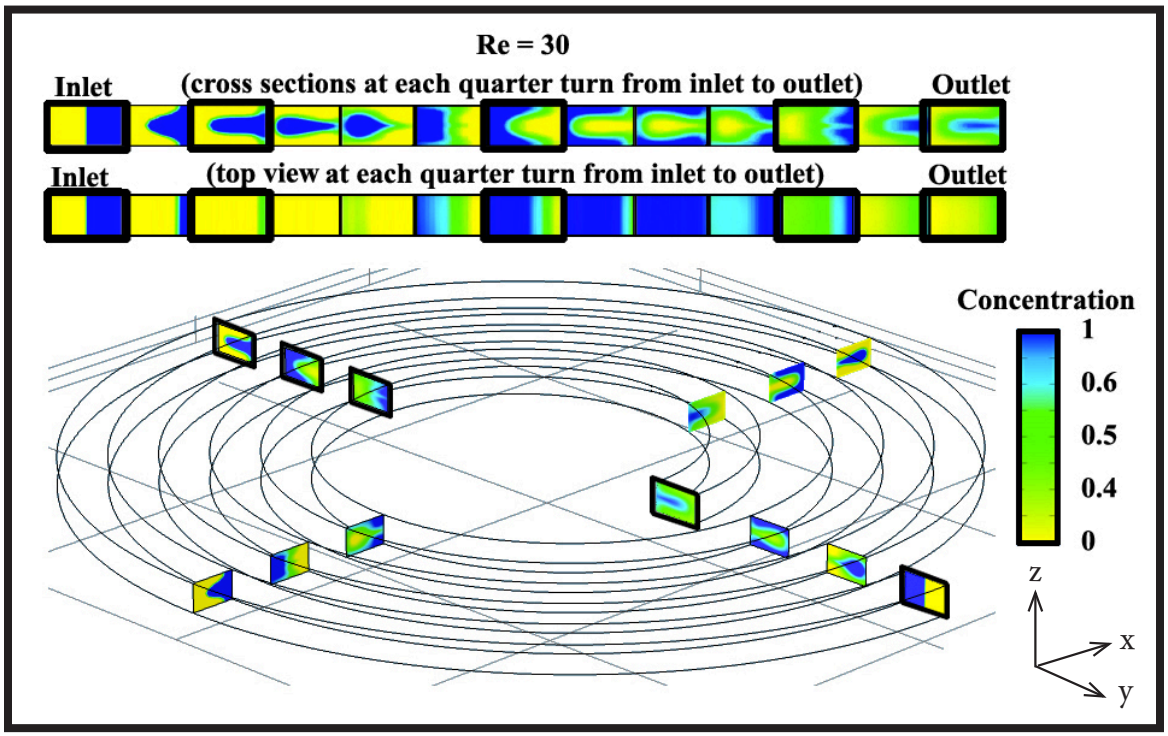

Figure 47: PDMS spiral mixer model concentration surface plots and visualization of line data for Re = 30.

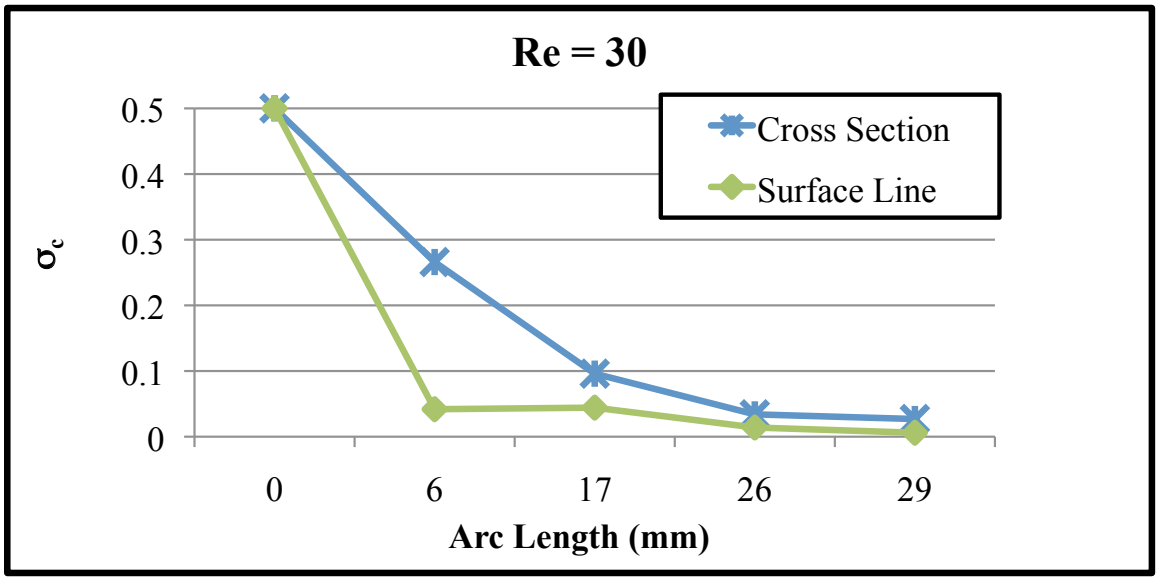

Figure 48: DMI PDMS spiral mixer model plots of concentration along the mixing path length for Re = 30.

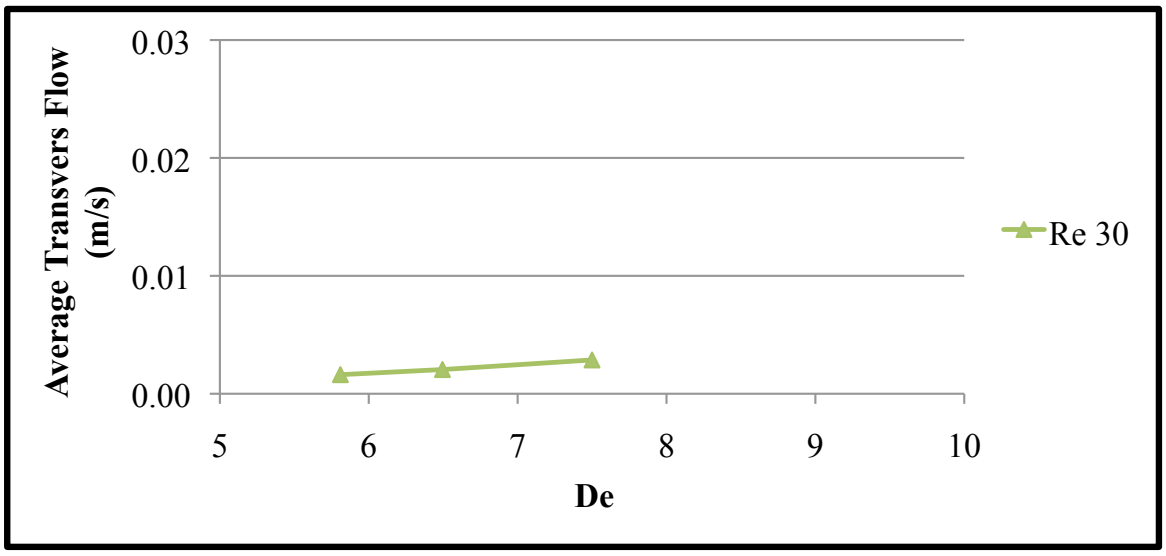

Figure 49: Plot of De versus transverse flor for Re = 30

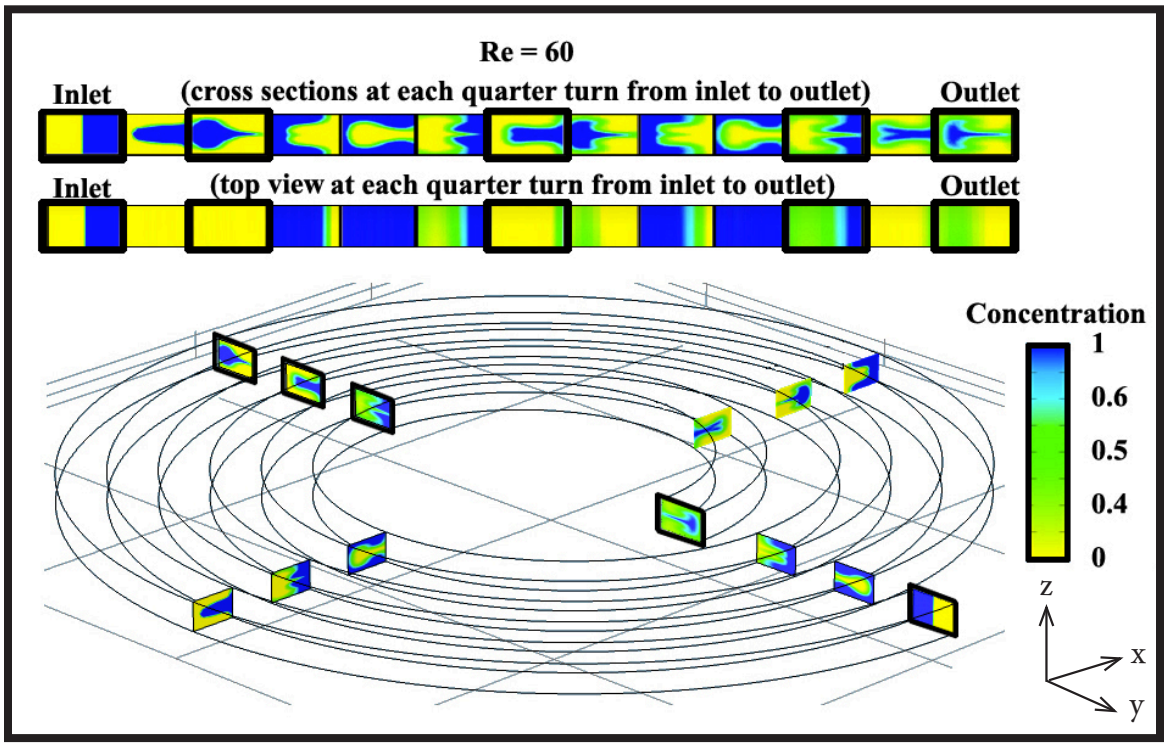

Figure 50: PDMS spiral mixer model concentration surface plots and visualization of line data for Re = 60.

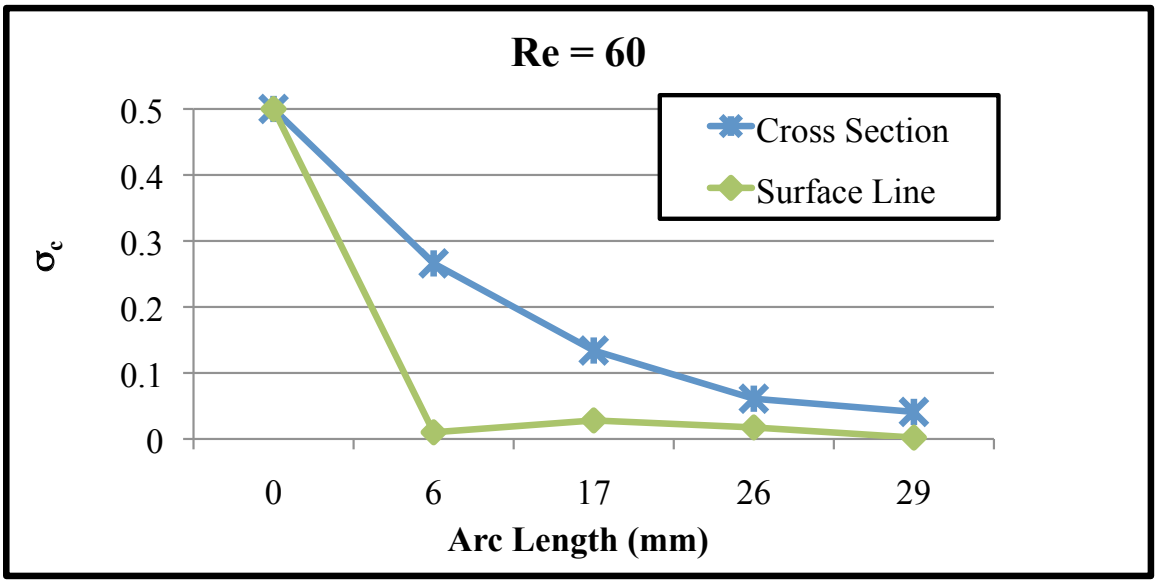

Figure 51: DMI PDMS spiral mixer model plots of concentration along the mixing path length for Re = 60.

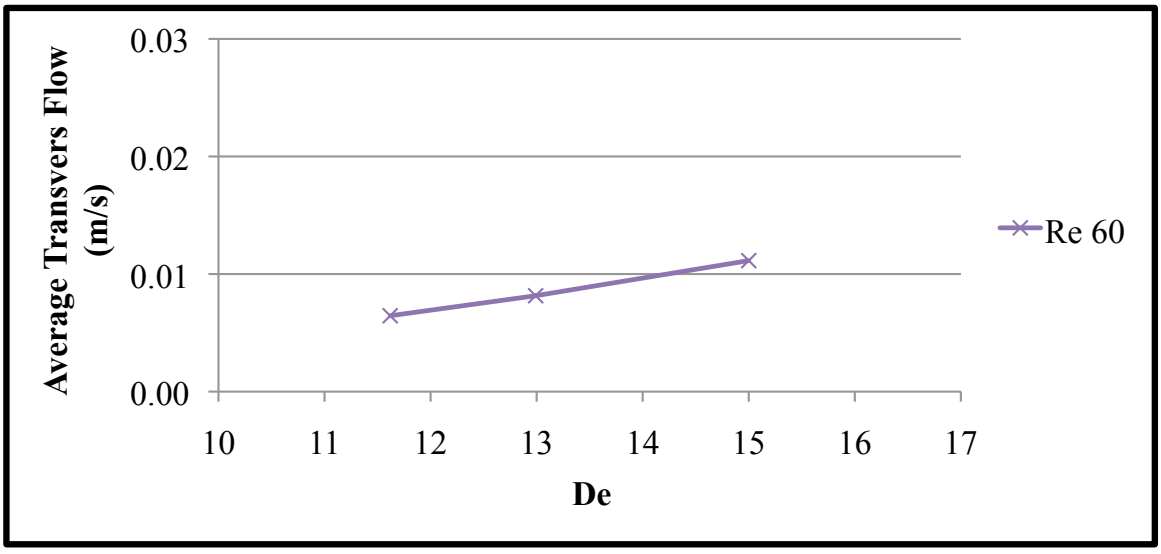

Figure 52: Plot of De versus transverse flow for Re = 60.

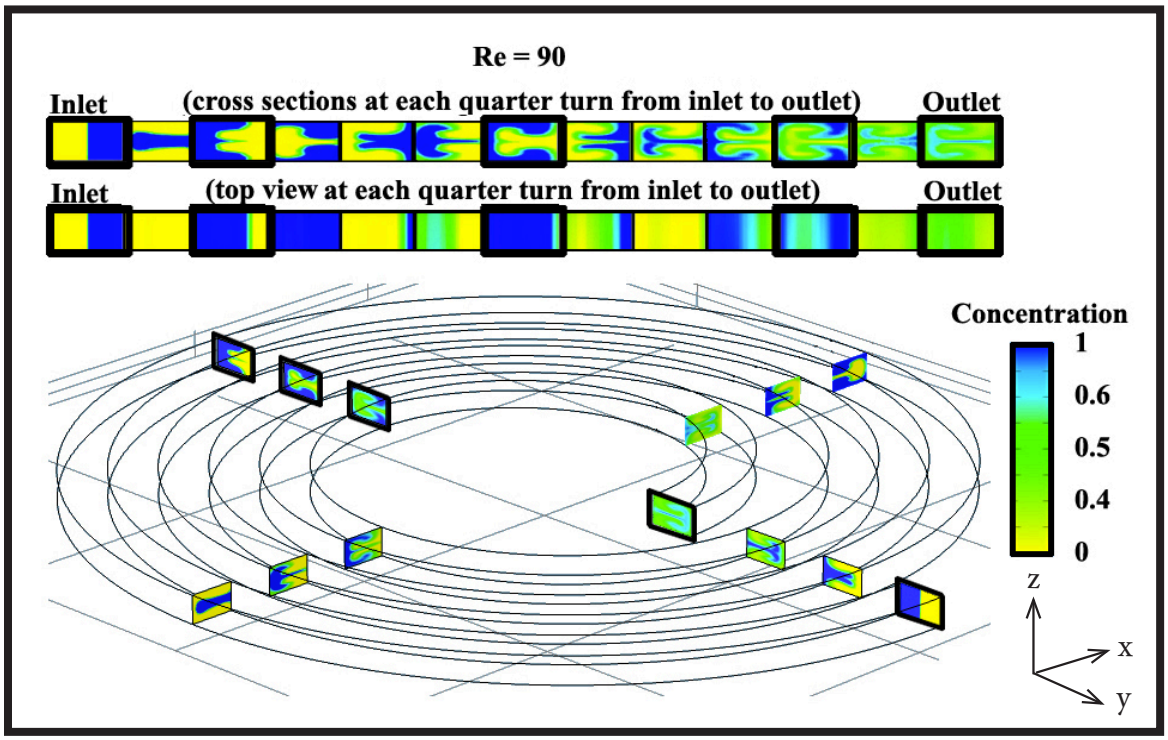

Figure 53: PDMS spiral mixer model concentration surface plots and visualization of line data for Re = 90.

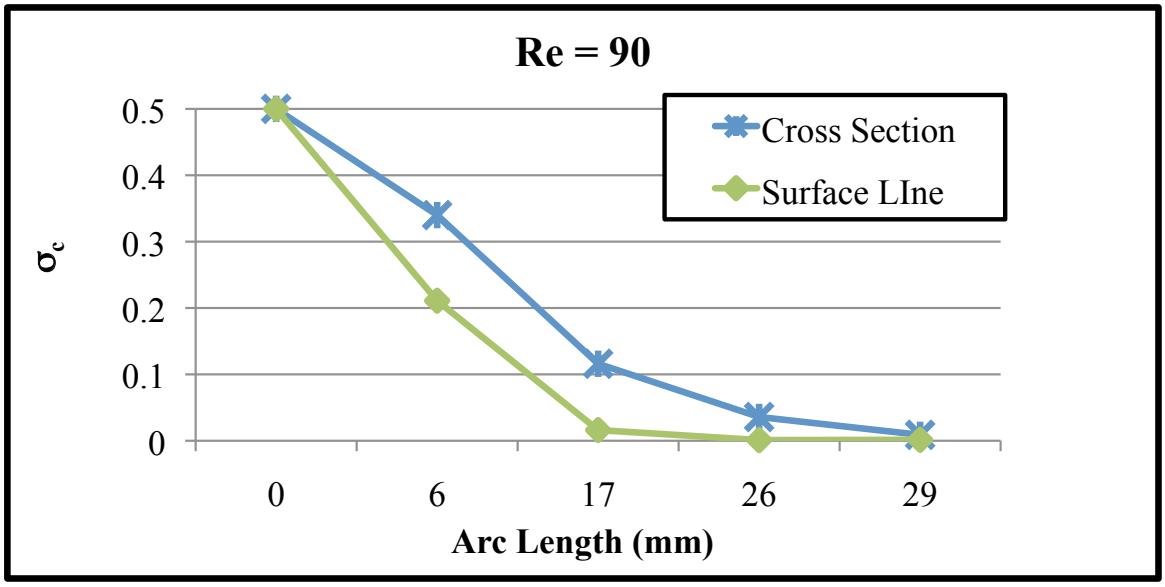

Figure 54: DMI PDMS spiral mixer models plots of concentration along the mixing path length for Re = 90.

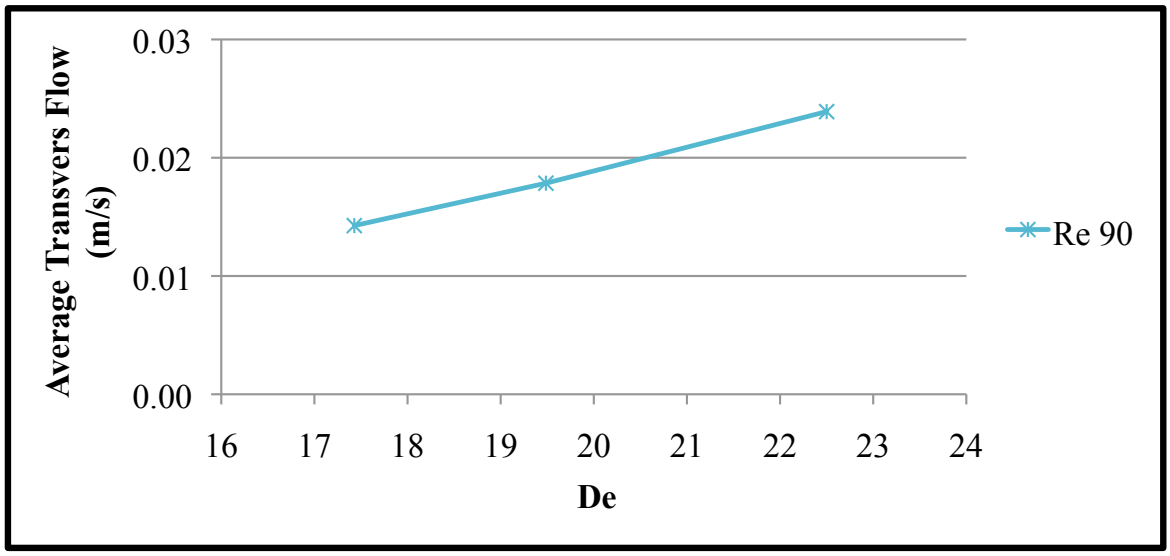

Figure 55: Plot of De versus transverse flow for Re = 90.

CHAPTER VIII

DISCUSSION

For the straight channel model, the results appeared as expected and corresponded to a similar model reviewed in the literature. In Figure 56, which shows a summary of the straight channel concentration and velocity field at Re = 8, 12, 30, 60, and 90, it can be seen that the flow velocity in the center of the channel increases with Reynolds number. The inlet velocity condition was increased from 0.05 to 0.6 m/s. Consequently, the residence time for diffusion at the interface of the fluids is decreased which reduces the time available for mixing. Figure 57 and Figure 58 also illustrate this trend. Figure 57 shows how the mixing increase along the path length for each channel, but decreases with increasing Re. Figure 58 presents the data as Re versus concentration variance for comparison to the spiral mixer data.

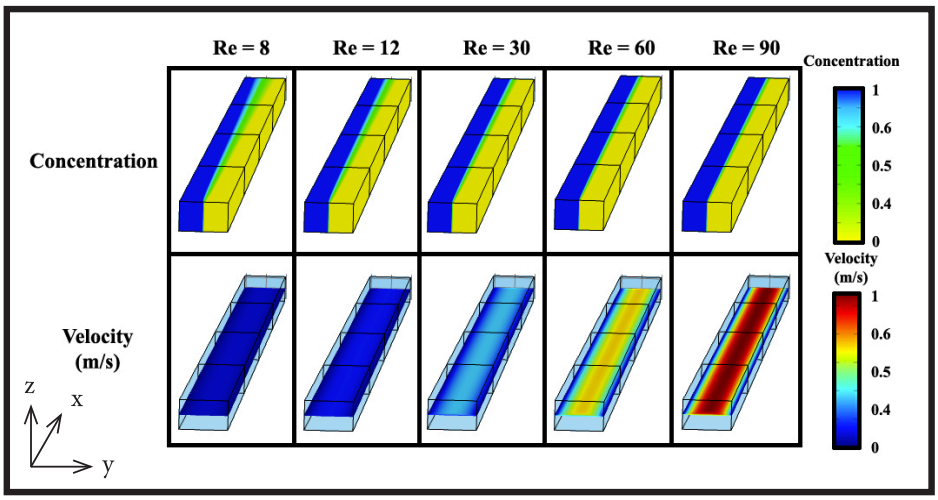

Figure 56: Straight channel model data comparison for Re = 8, 12, 30, 60, and 90.

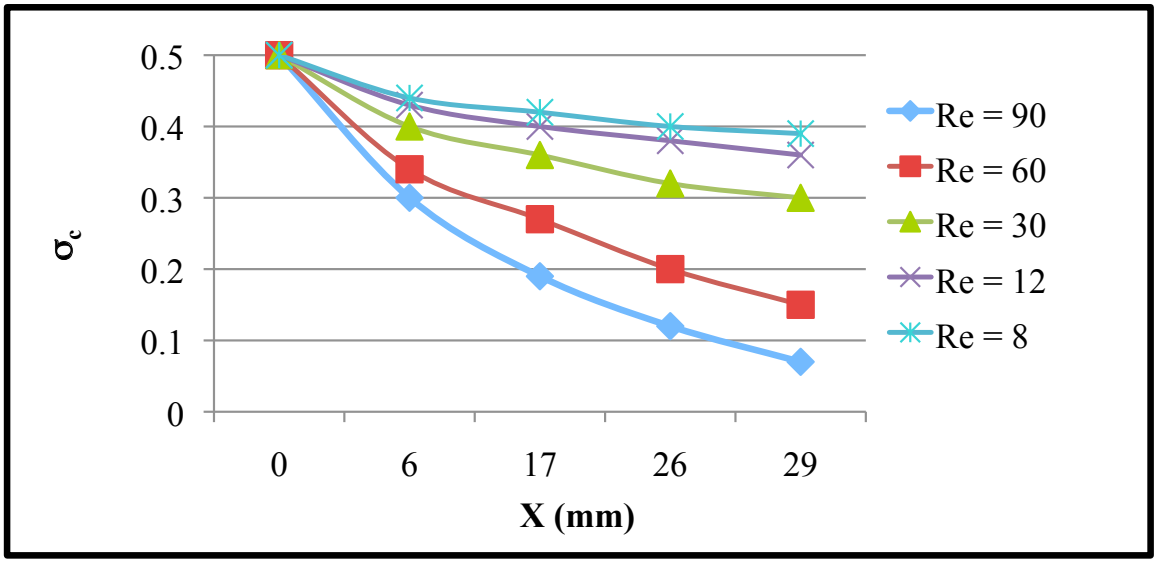

Figure 57: Plots of Re versus concentration variance at 1/4 length intervals along the length of the straigh channel (case 1).

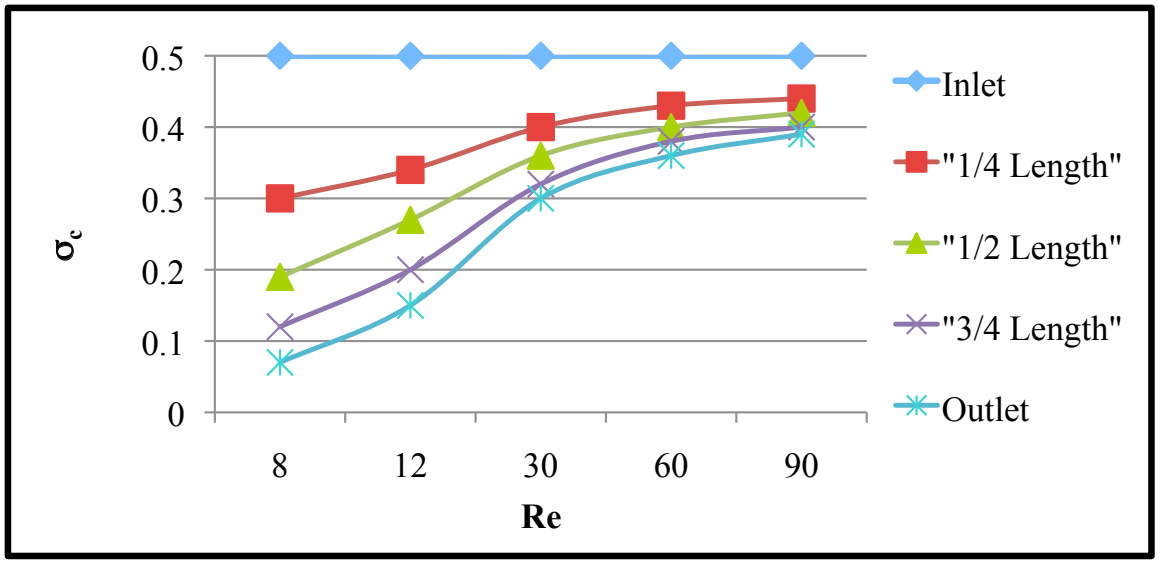

Figure 58: Plots of distance along straight channel length for concentration variance for straight channel (Re 8-90).

Cross sectional surface plots for the DMI PDMS spiral mixer are presented in Figure 59. It is evident that, even at a low Re of 8, the interface between the two flows becomes elongated along the length of the channel. For Re = 12, when the flow reaches the end of the channel, it can be seen that the inlet streams have essentially folded in half. The interface between the two flows is thus greatly increased compared to the straight channel model. For Re 30 to 90, the flow begins to show complete rotations within the length of the channel. As the Re increases, the length over which complete rotations occur decreases. In Figure 60, there is a plot of Re versus σ_c. The lowest values for σ_c can be seen at the outlets for Re = 12 and 90. For Re = 12, the mixing is dominated by diffusion, while for Re = 90, the mixing is dominated by convection. As was shown previously in the straight channel, at these significantly higher flow rates in a straight channel, the mixing would be minimized due to the lack of time for diffusion to occur at the interface. Interestingly, at Re = 12, the mixing appears to be significantly greater than for any other case. This would appear to be due to the fact that the flow is still slow enough for diffusion across the interface to have a substantial effect. Also, the interfacial arc between the two fluids is increased which allows for more surface area across which diffusion occurs between the two flows.

In order to better analyze the flow from the surface perspective versus the cross section, σ_c across a line of data at the top of the chip was calculated in a similar manner to the cross-sectional data. Figure 61 shows a visualization of that the concentration at a line on the surface where the cross sectional data was analyzed. The contour plots are representative of each quarter turn along the spiral path. It appears quite different from Figure 59. It is difficult to draw any conclusions from a visual inspection of the data. In some regions there are clearly two distinct fluid flows, while in other regions only one of the fluids is apparent. The trends along the flow path correlate well in the low Re range (8-12), but diverge at higher values (Re > 30). Overall they do both correctly show that the flow is more mixed at the outlets than the inlets. The data for the line analysis is plotted in

data, contrary to the cross section data, it appears that mixing is nearly complete by the first spiral for Re = 60 and Re = 90. Figure 63 shows a zoomed view the same plot for σ_c of 0 to 0.1. It is apparent that from this type of analysis, that the fluids can appear to "un-mix". This effect is most pronounced for Re = 60 where the fluid appears more mixed at the first spiral than at the second and third. At the outlet, the fluid appears well-mixed again. Although this analysis represents mixing at the surface, it does not incorporate the transmission of data from the interior that was present in the experimental photos. Nevertheless, this plot exhibits the same trends that were seen in the experimental data.

In order to visualize the flow effect that is causing the mixing, surface plots of the transverse flow magnitudes are shown in Figure 64 for Re = 30, 60, and 90. The secondary flow is much smaller than the axial flow by over an order of magnitude. As was predicted, it is evident that as the Dean forces increase, the flow from the inner side of the channel is pushed radially outward and then back along the channel wall creating a counter-rotating vortex pair. A plot of Re versus De is presented in Figure 65. As anticipated, De increases with Re.

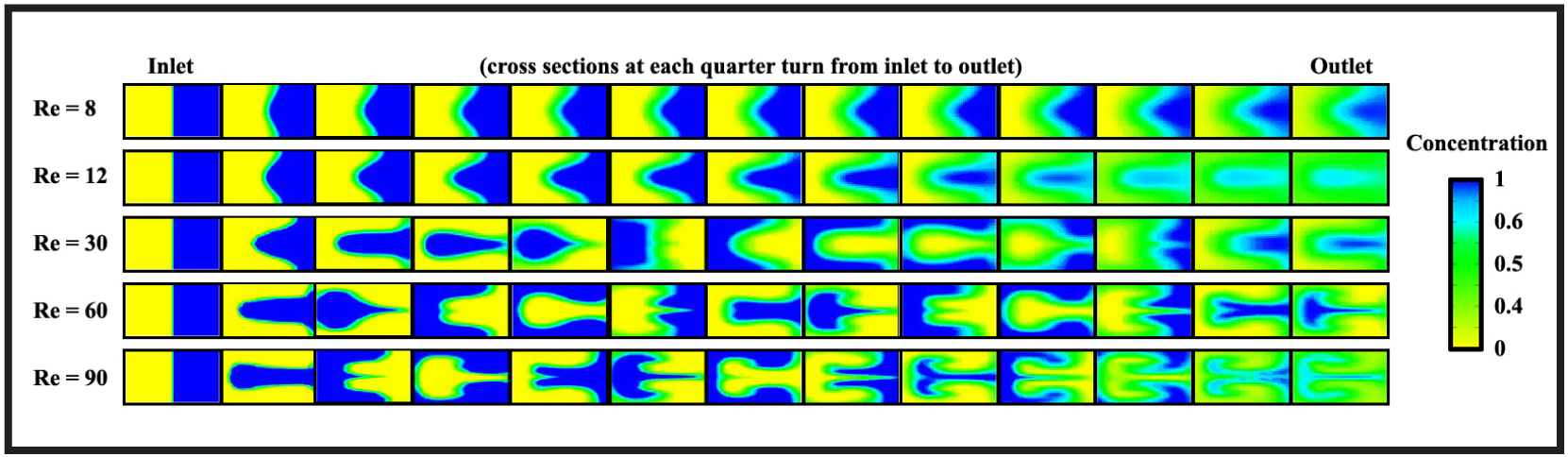

Figure 59: Surface plots of cross sections from the DMI PDMS mixer model at each quarter turn from inlet to outlet.

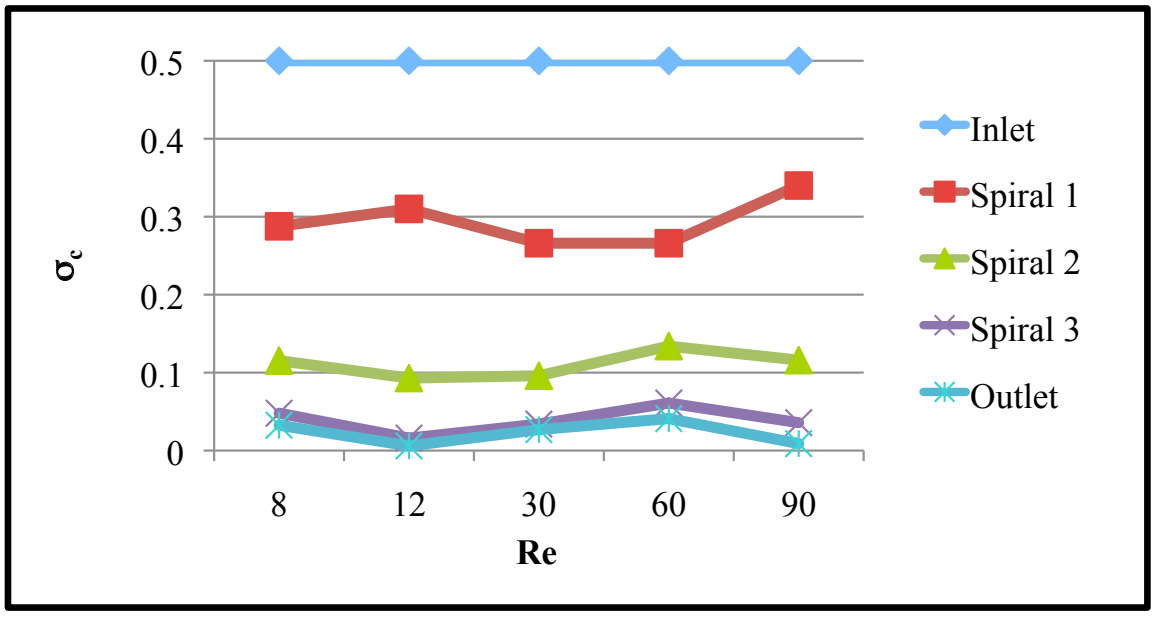

Figure 60: Plot of Re versus σ_c for DMI PDMS spiral mixer model.

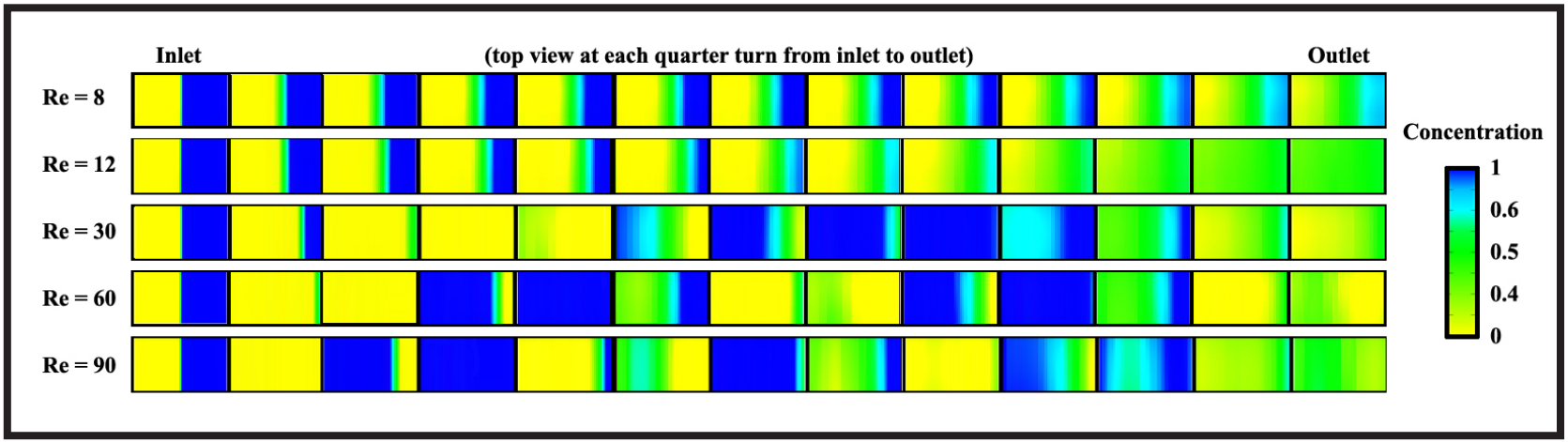

Figure 61: Visualization of line data taken at the same regions were cross sectional surface mixing was assessed for the DMI PDMS spiral mixer.

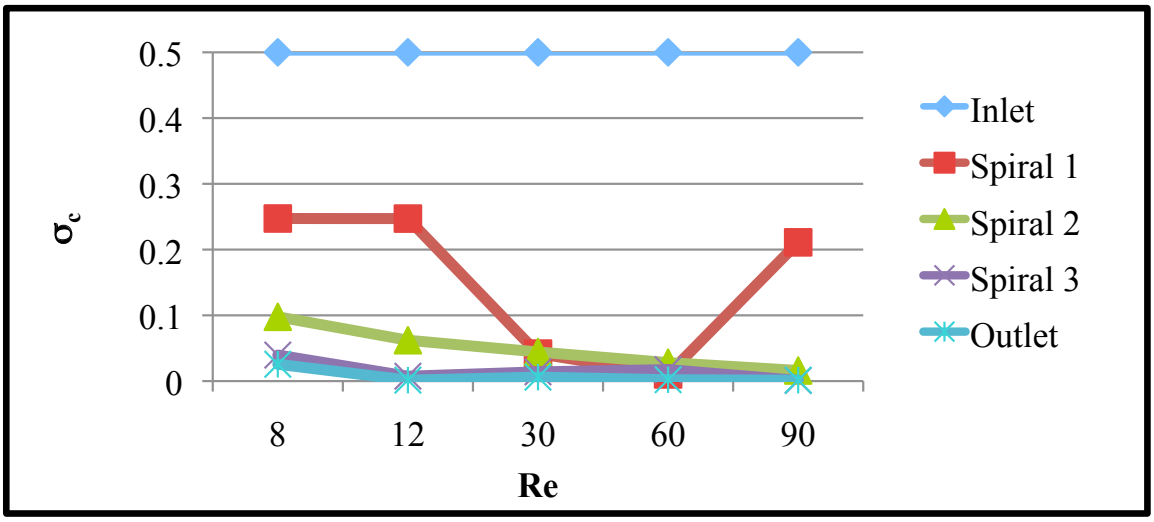

Figure 62: Re vs σ_c for DMI PDMS spiral mixer surface line data.

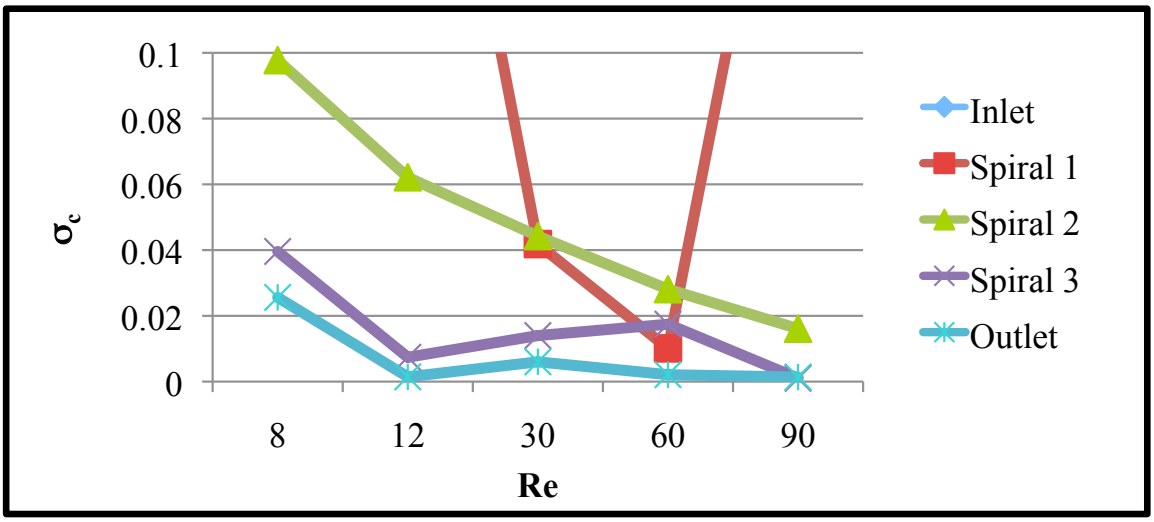

Figure 63: Zoom view of Re vs σ_c for DMI PDMS spiral mixer surface line-data.

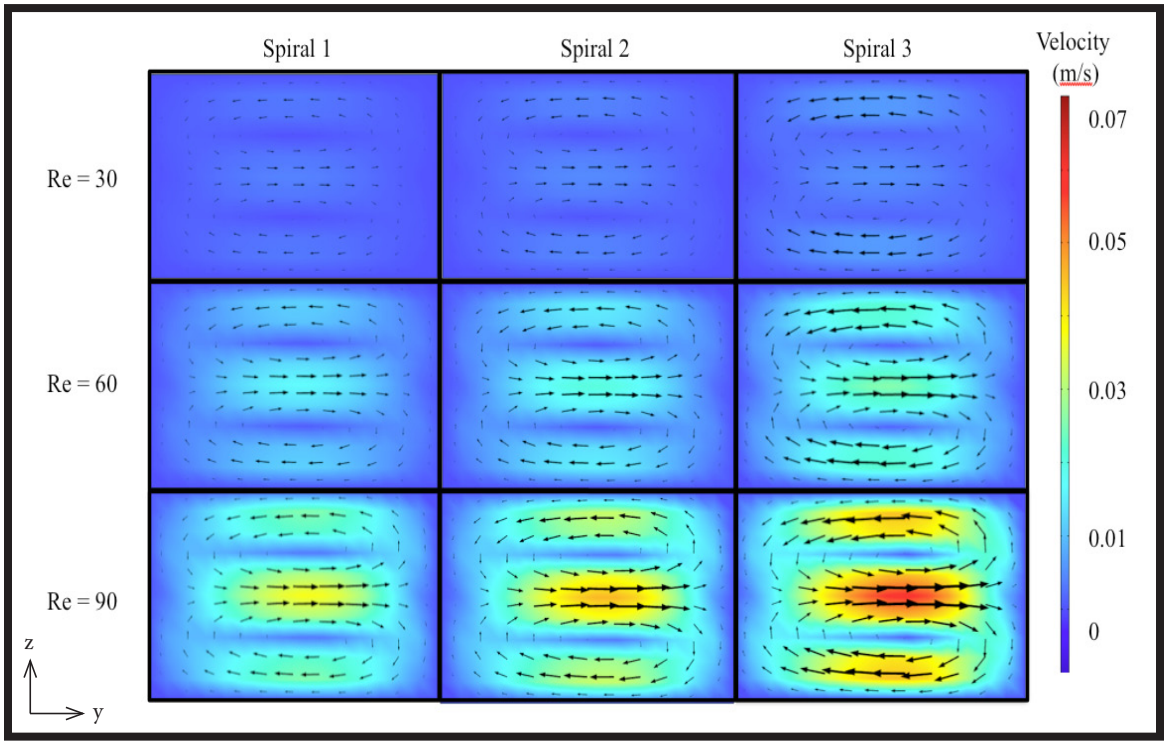

Figure 64: Surface plots of transverse velocity magnitude for Re = 30, 60, and 90. Black arrows show the transverse flow field and furthermore the Dean flow vortices.

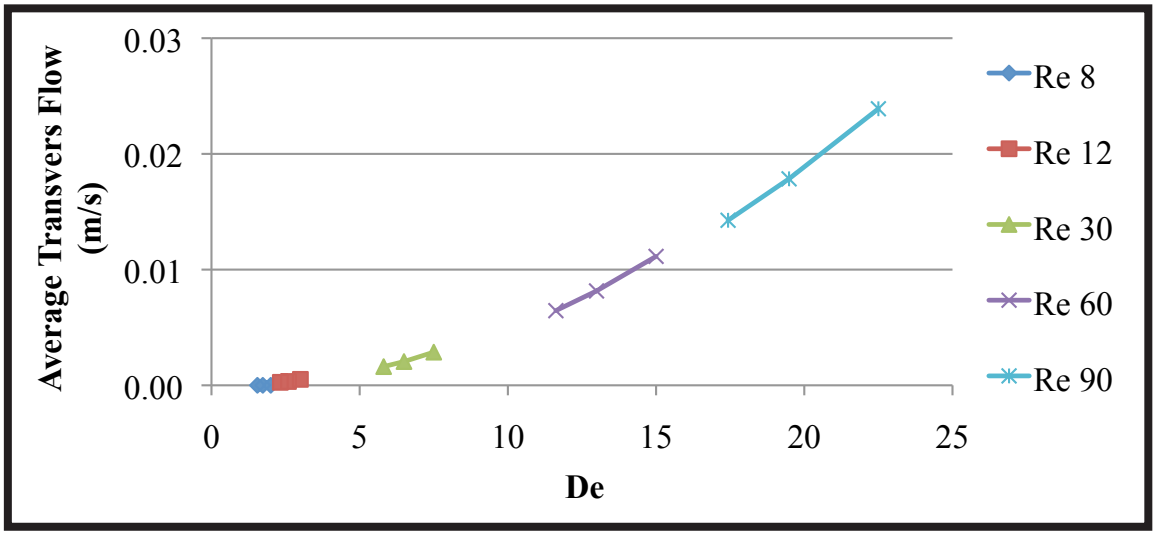

Figure 65: Plot of Dean number versus transverse flow magnitude.

CHAPTER IX

CONCLUSIONS

This study was performed in order to assist in the development of a spiral mixer, which will be a key component of a medical diagnostic technology tool that the DNA Medicine Institute is developing for the National Aeronautics and Space Administration. The ultimate goal of the diagnostic technology will be to provide general-purpose biological sample analysis. In order to satisfy the unique constraints of space travel, the device must: utilize minimal power, occupy a small volume, utilize minimal reagents, and satisfy extended (~ 3 year) shelf life requirements. Reuse of the microfluidic pathways was one of the unique design choices that were made to enable satisfaction of the unique requirements of a diagnostic tool for use during space exploration. Reuse of the fluid pathways will greatly reduce the need for consumables, especially as compared to current biological diagnostic devices that rely on disposable microchips for each analysis. Optimization of the mixing process will also reduce the volume of reagents required while ensuring sufficient mixing and dilution for each assay. To enable reusability of the fluidic pathways and ensure a long operational lifetime of the device, a simple and robust passive spiral mixer was chosen for ensuring mixing and dilution. The spiral mixer was preferable over other passive mixing options as fouling and clogging risks are minimized.

In order to gain confidence in the mixer computational model, a simple straight channel

diffusion based mixer was initially modeled. This model had the same cross sectional area and fluid path length as the spiral mixer and was analyzed in the same Re range as the spiral mixer (8 – 90). It was seen in the model that diffusive mixing decreased with increasing Re. As the flow velocity increased, the opportunity for molecular diffusion at the interface of the fluids decreased.

A computational model of a spiral mixer was then modeled. This model showed that from Re 8 to 12 the mixing increased, while from Re 12 to 60 mixing decreased and from Re 60 to 90 mixing again increased. This differs from the previous model due to the added centrifugal flow effects that arise from flow in a curved channel. From Re 8 to 12, the interface between the separate flows is greatly extended which enables the opportunity for diffusive mixing even though the flow is slightly faster. In the straight channel, faster flow would decrease mixing. The decrease in mixing from Re 12 – 60 is similar to what was seen in the straight channel. Although the interface continues to distort at these ranges the increasing flow rate again leads to a decrease in mixing. From Re 60 to 90, the Dean flow effects increase to a point where the mixing begins to increase.

The model correlated well with the experimental data. As the experimental data was obtained from a top view approach, the experimental results could not resolve regions where Dean flow caused the flow to rotate in the channel. There is an uncertainty in the experimental data due to the transmission data that was present in the experimental photos and therefore data. This leads to uncertainty in the experimental data and that uncertainty is difficult to quantify. The model was able to provide more insight into these regions. Mixing occurred primarily by diffusion across the fluid interface between Re of 8 and 12 (De < 2). A combination of diffusion and convection from transverse flow was responsible for mixing in the range of Re between 12 and 30 (De 2 – 8). At the higher Re, above 30 (De > 11), mixing occurred primarily due to Dean flow effects. As the secondary flow strength increases with increasing Dean number, the fluid interface becomes progressively more

convoluted allowing for increased interfacial area between the fluids. At the same time, high flow rate reduces the time available for diffusion to mix the fluids. Thus, the mixing process involves a balance in providing increased interfacial area and overall residence time for diffusion. The model appears to be a good tool for use to optimize design choices for mixing as calculations can be performed across cross sectional areas to provide a better insight into mixing performance.

CHAPTER X

FUTURE WORK

The mixing studies in the effort were carried out for fluids with properties similar to water. Ultimately it would be desirable for the device to be capable of processing multiple types of samples, such as: blood, urine, saliva, or potable water. The next stage is to model fluid with properties similar to blood. Therefore the model will next be validated with a fluid that is more representative of blood. The next stage in the DNA Medicine Institute's work is to perform another mixing experiment with their current chip design using a confocoal microscope for imaging. This type of image will provide mixing information throughout the cross-section of the chip and will be a validation for the numerical model since the experimental data will provide 3D results. As the confocal microscopy set-up is laborious and expensive, DMI will only run simulations with a 50:50 ratio of blood to diluent. After the model is validated with data from these experiments, further dilution studies will be performed numerically to determine the most efficient dilution ratio. Once this is identified, DMI can run one additional confocal experiment and provide a quantitative evaluation. The design process thus becomes iterative between experiments and CFD for more efficient, timely decision on the best design for space. As further design needs and constraints are defined this model will be used a tool for design optimization studies.

REFERENCES

Adeosun, J. and A. Lawal (2009). "Numerical and experimental studies of mixing characteristics in a T-junction microchannel using residence-time distribution." Chemical Engineering Science **64**(10): 2422-2432.

Adeosun, J. T. and A. Lawal (2009). "Numerical and experimental mixing studies in a MEMS-based multilaminated/elongational flow micromixer." Sensors and Actuators B: Chemical **139**(2): 637-647.

Ansari, M. and K. Kim (2009). "Parametric study on mixing of two fluids in a three-dimensional serpentine microchannel." Chemical Engineering Journal **146**(3): 439-448.

Auroux, P. A., D. Iossifidis, et al. (2002). "Micro total analysis systems. 2. Analytical standard operations and applications." Analytical chemistry(74): 2637-2652.

Bringer, M. R., C. J. Gerdts, et al. (2004). "Microfluidic systems for chemical kinetics that rely on chaotic mixing in droplets." Philosophical transactions. Series A, Mathematical, physical, and engineering sciences **362**(1818): 1087-1104.

Brown, D. (2011). Experimental Flow Characterization Activities for Reusable Lab on a Chip Technology. **RLOC-DOC-003**.

Chan, E. (2009). Reusable Handheld Electrolytes & Lab Technology For Humans: rHEALTH Sensor. NASA SBIR NNX09CA44C

Chan, E. (2010). "FAST Final Report."

Chen, C. S., D. N. Breslauer, et al. (2008). "Shrinky-Dink microfluidics: 3D polystyrene chips." Lab on a chip **8**(4): 622-624.

Chin, C. D., V. Linder, et al. (2007). "Lab-on-a-chip devices for global health: past studies and future opportunities." Lab on a chip **7**(1): 41-57.

COMSOL. (2011). "Laminar Static Mixer." from http://www.comsol.com/showroom/documentation/model/245.

Datta, A. K. and V. Rakesh (2010). An introduction to modeling of transport processes : applications to biomedical systems. Cambridge, UK ; New York, Cambridge University Press.

FDA (1997). Design control guidance for medical device manufacturers., Center for Devices and Radiological Health.

Finlayson, B. A., A. Aditya, et al. (2008). Mixing of Liquids in Microfluidic Devices. COMSOL Conference, Boston.

Grimes, A., D. N. Breslauer, et al. (2008). "Shrinky-Dink microfluidics: rapid generation of deep and rounded patterns." Lab on a chip **8**(1): 170-172.

Hessel, V., H. Lowe, et al. (2005). "Micromixers?a review on passive and active mixing principles." Chemical Engineering Science **60**(8-9): 2479-2501.

Howell, P. B., Jr., D. R. Mott, et al. (2004). "Design and evaluation of a Dean vortex-based micromixer." Lab on a chip **4**(6): 663-669.

Kumar, V., M. Paraschivoiu, et al. (2011). "Single-phase fluid flow and mixing in microchannels." Chemical Engineering Science **66**(7): 1329-1373.

Lin, K. and J. Yang (2007). "Chaotic mixing of fluids in a planar serpentine channel." International Journal of Heat and Mass Transfer **50**(7-8): 1269-1277.

Logan, D. L. (2011). A First Course in the Finite Element Method, Global Engineering.

NASA (2009). NASA Systems Engineering Processes and Requirements. NPR 7123.1A, Office of the Chief Engineer

Nelson, E. S. (2011). "Design principles for microfluidic biomedical diagnostics for space." In "Biomedical Engineering, Vol 4", R. Fazel, ed. Intech. To be published June, 2011.

Nguyen, N.-T. (2008). Micromixers: fundamentals, design and fabrication. Norwich, NY, William Andrew.

Nguyen, N.-T. and Z. Wu (2005). "Micromixers—a review." Journal of Micromechanics and Microengineering **15**(2): R1-R16.

Reyes, D. R., D. Iossifidis, et al. (2002). "Micro total analysis systems. 1. Introduction, theory, and technology." Analytical chemistry(74): 2623-2636.

Saliterman, S. (2006). Fundamentals of bioMEMS and medical microdevices. Hoboken, NJ Bellingham, Wash., Wiley-Interscience; SPIE Press.

Schulte, T. H., R. L. Bardell, et al. (2002). "Microfluidic technologies in clinical diagnostics." Clinica Chimica Acta **321**(1-2): 1-10.

Stroock, A. D., S. K. W. Dertinger, et al. (2002). "Chaotic Mixer for Microchannels." Science **295**: 647-651.

Sudarsan, A. P. and V. M. Ugaz (2006). "Multivortex micromixing." Proceedings of the National Academy of Sciences of the United States of America **103**(19): 7228-7233.

Virk, M. S., Holdo A E, Kaennakham S (2007). Numerical analysis of fluid mixing in T-shape micro mixer. COMSOL Users Conference, Grenoble.

Weigl, B. H., R. L. Bardell, et al. (2004). "Modeling diagnostic microdevice processes to speed product development." IVD Technology Retrieved 04/07/2010, from http://www.ivdtechnology.com/print/516.

Yamaguchi, Y., F. Takagi, et al. (2004). "Interface configuration of the two layered laminar flow in a curved microchannel." Chemical Engineering Journal **101**(1-3): 367-372.